AN ENERGY – FRAGMENTATION APPROACH FOR BLASTING PERFORMANCE

by

Martha Maria Barreto Maya

A thesis submitted in partial fulfillment of the requirements for the degree of

Master of Science

in
Mining Engineering

Department of Civil and Environmental Engineering
University of Alberta

ABSTRACT

Blasting is widely used in mining operations as the primary comminution process to reduce the in-situ rock into fragmented material suitable for the subsequent transport and processing. The energy used is released from an explosive by detonation and transferred to the rock mass via a shock front resulting from the initial high pressure of detonation and continuing gas expansion pressure from the products of the explosion. Both play an essential role in fracture development.

This research was focused on creating a practical methodology to measure not only the explosive energy in terms of "specific energy or pressure" and estimate how much of it is used for actual fragmentation, but also to create an easy to use tool to identify and develop optimization strategies for a bench blast in mines and quarries.

To accomplish this, four stages were developed: a) Explosive characterization in terms of initial detonation pressure and subsequent gas expansion pressure generated, b) Fragment size distribution determination using an Image Analysis System, specifically WipFrag software, c) Rock tensile strength estimation using not only the widely recognized Brazilian Test, but also Digital Image Correlation (DIC) system, and d) a semi-empirical approach for pressure expenditure estimation at three radii from the center of the hole, representing the maximum zone affected by the blast, the outer limit of the crushing zone, and the area midway between borehole wall and maximum zone.

It was observed that both the initial high detonation pressure and the subsequent gas pressure are essential for the tensile crack initiation and propagation, even though the methodology is not capable of estimating how much of each type of energy is used to create the resulting rock size

distribution. For a daily blasting assessment, the technique is easy to follow and only a few variables are needed for it's implementation.

ACKNOWLEDGMENT

I wish to express my deepest gratitude to my supervisor, Dr. Tim Joseph, who gave me the opportunity to accomplish one of my biggest professional goals. His wide knowledge, kindness, trust, motivation, patience and continue support were essential during this journey. Also, I would like to thank Professor John Sammut, who provided substantial support. His academic and practical guidance and recommendations were invaluable in the completion of this project.

I wish to acknowledge SunHills LP mining operation, otherwise known as the Highvale Mine for granting me access to its engineers and field operations. Special thanks to Dylan Wedgewood who helped me coordinate mine site visits and the exchange of technical data and information. I would also like to extend my thanks to Lucas Duerksen for his guidance during laboratory work.

I would like to thank my husband, Fabian, for his love, unfailing support and encouragement during these years, thank you for being part of this team. My most sincere thank you to my Father, Donaldo Barreto and my two sisters, Carolina and Angela for trusting me and making me feel close to them. Finally, thank you mom for being next to God taking care of me.

TABLE OF CONTENTS

LIST OF TABLES

LIST OF FIGURES

LIST OF ABBREVIATIONS

2D	Two-dimensional
3D	Three-dimensional
AN	Ammonium Nitrate
ANOVA	Analysis of Variance
ARF	Actual number of radial fractures
ASTM	American Society for Testing and Materials
AWS	Absolute weight strength
B	Burden
BT	Brazilian Test
C	Stemming
CZ	Crushing Zone
C-J	Chapman-Jouguet
$\mathbf{C_{CZ}}$	Circumference at outer limit of the CZ
$\mathbf{C_{Max}}$	Circumference at maximum zone affected by the blast
$\mathbf{C_V}$	Specific heat capacity at constant volume
$\mathbf{C_{50}}$	Circumference at the area midway between borehole wall and C_{Max}
$\mathbf{D_B}$	Borehole diameter
DDZ	Detonation Driving Zone
DIC	Digital Image Correlation
DOF	Depth of Field
DPT	Direct Pull Test
DTS	Direct Tensile Test
E	Young´s Modulus
$\mathbf{E_{wk}}$	Expansion Work
FO	Fuel oil
G	Shear Modulus
$\mathbf{H_0}$	Null hypothesis
$\mathbf{H_A}$	Alternative hypothesis
IAS	Image Analysis System

ISEE	International Society of Explosive Engineers
ISRM	International Society for Rock Mechanics
L	Charge or explosive column
MP	Megapixel
MRF	Maximum number of Radial Fractures
MSDS	Material Safety Data Sheet
$\mathbf{M_m}$	Molar mas
Pa	Pascal
PF	Powder Factor
PLT	Point Load Index Test
PSD	Particle Size Distribution
$\mathbf{P_{Det}}$	Detonation Pressure
$\mathbf{P_{Gas}}$	Gas pressure
Q	Heat content released by a chemical reaction
R	Molar gas constant
RWS	Relative weight strength
S	Spacing
SA	Surface Area
SD	Standard Deviation
SPH	Sphericity
$\mathbf{T_e}$	Temperature of the explosion
TDS	Technical Data Sheet
TFZ	Tensile Fracture Zone
KPI	Key Performance Indicator
U	Internal Energy
UAVs	Unmanned Aerial Vehicle
UCS	Unconfined compressive strength
v	Poisson ratio
VOD	Velocity of Detonation
$\boldsymbol{\varepsilon_x}$	Horizontal strain
$\boldsymbol{\varepsilon_y}$	Vertical strain

$\boldsymbol{\varepsilon_{xy}}$	Shear Strain
$\boldsymbol{\tau_{xy}}$	Shear stress
$\boldsymbol{\sigma_{x}}$	Horizontal stress
$\boldsymbol{\sigma_{y}}$	Vertical stress
$\boldsymbol{\sigma_{T}}$	Tensile strength
$\boldsymbol{\sigma_{t(BT)}}$	Tensile strength calculated from BT equation
$\boldsymbol{\sigma_{t(S)}}$	Tensile strength calculated from strain values
$\boldsymbol{\sigma_{t(PT)}}$	Tensile strength calculated from Direct Pull test

1. INTRODUCTION

1.1 Background and Problem Statement

In common with many other industries, mining is increasingly competitive to achieve a low cost bottom line. As such, mining companies strive to increase efficiency through cost reduction whenever possible. All corporate foci, whether productive or non-productive in nature, are scrutinized, analyzed and modified frequently to changing operational and market conditions. It is thus essential that not only individual processes are clearly understood but also their impact on the entire operational system in a corporation.

Surface mining operations are often viewed to commence with bench rock blast hole drilling and blasting to achieve fragmentation. These two processes determine the characteristics of the feed for subsequent loading, hauling, plant-processing or raw product delivery. When analyzing blasting, documented studies define performance in terms of outcomes such as vibration, noise, movement (heave), toxic fumes released, or how the broken material influences the efficiency of other processes. Only a few contemplate energy release during blasting as an efficiency of fracturing and fragmenting in-situ rock; and how such energy release knowledge can be used as a key performance indicator (KPI) in blast efficiency assessment and design for a mining operation.

Explosive energy partitioning is a topic frequently debated, with few researchers taking on the challenge. Ouchterlony et al., (2003) performed five full-scale tests in a limestone quarry using a mixed emulsion and estimated that 3 to 2 % of the explosive energy was lost as Seismic energy with only 0.1 to 0.2 % employed in fragmentation. Using a similar methodology, Sanchidrián, Segarra, and López, (2007) quantified that 1.9 to 6 % of the explosive energy, referred to it as heat content at constant volume (Q_V), was used as fragmentation energy. They stated that the kinetic and seismic energy efficiencies ranged from 3.3 to 10.3 % and 0.9% respectively. Hamdi, Bouden Romdhane, du Mouza, and Le Cleac'h, (2008) showed efficiencies of 11% and 6 % for micro and macro fragmentation respectively. Calnan (2015) estimated efficiencies of 0.2 to 0.5% for fragmentation following the work of Hamdi and Sanchindrian.

Clearly, greater understanding of energy partitioning is relevant to analyzing the ability of an explosive to fragment rock, but it is even more important to show the use of such knowledge in a clear KPI that may be applicable as an operational performance evaluation. In addition, any field applicable measuring tools or methodologies need to be practical, easy to perform, and quick, so as not to impede mining operations.

1.2 Objectives

The main objective of this thesis was to critically examine explosive sourced fragmentation energy utilized in blasting as detonation and gas pressures. In parallel, a study of the fragmentation outcome due to the explosive energy (pressure energy) transmitted to the intact rock, via analyzing particle size distributions obtained at a full field scale versus rock tensile strength at fracture observed through experimental laboratory testing was undertaken. The two approaches were then linked through a common parameter study.

The research work seeks to propose a practical and easy-to-use measuring tool, based on performing simple lab tests, oriented not only to assess required fracture energy, but also to implement improvement opportunities in the performance of operational blast design as a function of field explosive efficiency as a KPI.

1.3 Research Limitations

Breaking in-situ rock by blasting involves many complex mechanisms which occur over a very short period of time. There are many variables which make analysis difficult. Some of these are geo-mechanical in nature and therefore inherently variable, and some involve complex chemical reactions. None are fully understood. These issues make the topic controversial, and there is no agreement on the relative and proportional impact of detonation and gas pressures on final fragmentation. Researchers have adopted a variety of approaches, through both small and large-scale studies, which have increased knowledge to further understand the complexity, but none provide a complete picture.

This research was conducted at the Faculty of Engineering Surface Mining Research Laboratories at the University of Alberta, where it was not possible to perform any laboratory test using explosives. The author thus accepted some energy values reported by explosive manufacturers to characterize the ANFO explosive used, but in the context of understanding the manufacturer approach to measuring that energy. Also, to simplify some calculations, general equations and

basic assumptions were made, all of which are justified in this thesis. The approach adopted here was consistent with other researchers in the field.

1.4 Summary of methodology

The research was broken down in two areas. Initially, field-work was performed at a coal strip mining operation (Highvale Mine, Alberta; Sunhills Mining LP) to gather information on mining practice, blast design parameters and muckpile configurations. Also, rock samples were collected for laboratory analysis.

Laboratory work was carried out to determine the mechanical characteristics of the rock. The rock samples were cored and tested using a Universal Testing Machine following ASTM standards. In addition, different approaches were taken to determine the tensile (fracturing) strength of the rock and the results compared.

Finally, the collective data was analyzed to develop an easy to use measuring tool that can be used to determine the fragmentation efficiency and evaluate the blast performance in the field.

1.5 Thesis Outline

This thesis is organized in 6 chapters as described below:

- **Chapter 1**: Current chapter. The background information, research objectives and limitations found during the study are described. Also, a brief description of the methodology used to undertake this thesis is introduced.

- **Chapter 2:** A literature search that outlines the main concepts and theories currently used by academia and industry concerning the rock breakage process through blasting. Explosive energy, its propagation and its effect on the surrounding rock is discussed. Different particle size distribution measurement techniques are explained as a useful methodology for post blast assessment.

- **Chapter 3:** Provides detailed information about the mining operation, geological information and blasting parameters currently used at Highvale mine. Additionally, an explosive energy determination is conducted.

- **Chapter 4:** States the methodology and calculations followed to determine the particle size distribution (PSD) of the fragmented rock at Highvale mine.

- **Chapter 5:** Describes the methodology, calculations and analysis developed to identify the tensile mechanical properties of the rock sampled at the Highvale mine. Different approaches are taken for laboratory testing in assessing tensile strength. The results are compared, and their benefits and drawbacks are analyzed and presented.

- **Chapter 6:** Detonation and gas energy are estimated. Fragmentation energy efficiency is established, and a practical measuring tool is introduced.

- **Chapter 7:** Summarizes the major conclusions. Findings, limitations and possible future work are also discussed.

2. LITERATURE REVIEW

Rock fragmentation through blasting is a complex process that involves many variables, which need to be clearly understood to ensure that the resulting broken material is sufficient for downstream requirements, whether for processing, aggregate or other use. Small changes in variable magnitude have the potential to produce significant variations in the resulting fragmentation.

There are several approaches used in the mining industry today to evaluate fragmentation and blasting performance; but in most cases, each variable parameter, from blasting to grinding, is analyzed as part of a collective system and not as individual parameters. Regardless, few approaches consider energy input and efficiency of a system as a means of achieving a required fragmentation, where key parameters, related to blast design to achieve a desired fragmentation, can be modified to better control the fragmentation distribution outcome.

2.1 Blasting and Fragmentation

In most mining operations, drilling and blasting are the first stages of the mining operational production chain. The in-situ rock needs to be broken into size fractions suitable for subsequent processes. The aim is to satisfy all successive production requirements, whether loading, hauling, crushing, grinding or product delivery. Hence, some of the most critical objectives in a blasting program should be:

- An appropriate fragment size distribution for loading, hauling and subsequent crushing
- Material with enhanced surface area permitting ore mineral to be better exposed for mineral processing
- Stable final mine structures, such as like highwalls, pillars and roofs
- Minimum impact on security and the environment

Substantial documented evidence supports the premise that blasting can reduce the overall total cost of mining and processing. Kojovic, Michaux, and McKenzie, (1995) showed that incrementing powder factor by 16%, decreased mining cost for a net savings of $0.65/tonne. Brunton, Thornton, Hodson, and Sprott, (2003) determined a strong dependent relationship between crushed product particle size at 80% passing, P80, in a fragment size distribution and hydraulic excavator dig time to bucket pass ratio. Via Monte Carlo simulation, Brunton et al.

(2003) concluded that decreasing P80 from 600mm to 200mm reduced dig time to bucket pass ratio by 26%.

Cebrian and Flores, (2015) demonstrated cost savings of $0.05 per ton were achievable through choice of explosive. They showed that such an improvement represented $1M/year cost savings. Asraei (2016) showed that for an open pit copper mine, an increment of 20% in powder factor reduced blasting and milling costs by $0.04 and $0.096 per tonne respectively. Kabwe (2017) investigated the impact of utilizing air decking in blast-holes on overall blasting cost. He found not only a cost reduction of $19.84 per hole, but also a reduction in the amount of fly rock and mean fragment size.

To achieve improved fragmentation, the variables that affect the mode by which rock breaks must be considered; interpreting not only the impact of each, but also their influence one upon another in the overall fragmentation process. Variables fall into two groups – those that can be controlled and those that cannot. The characteristics explosives and blast design parameters are examples of variables over which we have some control; whereas variables such as rock type and structure are geologic and outside of our control, but with understanding of their influence, may be used to enhance a blast design.

As energy for fragmentation is sourced from the explosive, it represents a variable that may be manipulated through composition and quantity to achieve a desired fragmentation outcome. According to the International Society of Explosives Engineers (ISEE, 2011), an efficient blast is achieved only when the explosive energy is utilized effectively; dependent on five factors:

1) Energy distribution - which controls uniformity of fragmentation; where the borehole diameter is critical, as it defines the quantity of explosive per hole.

2) Energy confinement – which is necessary for post-detonation expanding gases to increase the pressure within the borehole region and cause fracture extension. Here the degree of competent stemming is an important design variable in controlling loss of gas pressure. However, knowledge of the rock mass geological and structural characteristics also figures largely here in defining the ability to contain pressure.

3) Energy level – defined as the amount of explosive energy exerted on the borehole surrounding rock; where an explosive contains a set degree of energy per unit weight, declared by manufacturer using proprietary methodologies of determination.

4) Relief - the unrestrictive presence of a free face permitting the blasted rock to move outwards into an available expansion space. Here, Burden is the controllable factor that contributes to creating a free face. The size of the burden is also a function of the quantity of explosive, through control of borehole diameter and therein as a function, the extendable cracking radius.

5) Explosive ratio - usually called powder factor (PF) or energy factor, representing the quantity of explosive required per unit volume of rock blasted.

2.2 Rock Fracturing Process

The rock fracturing process starts with the detonation of an explosive inside a borehole. Detonation is defined as a violent chemical reaction traveling through the explosive column at a velocity greater than the speed of sound in the explosive (ISEE, 2011). The resulting exothermic chemical reaction produces hot expanding gases at high pressure, which in turn bring about compression waves that are transmitted to the surrounding rock mass (Persson, Holmberg, and Lee, 1994).

Depending on the explosive type, a detonation can be described as “ideal” or “non-ideal”. According to Lopez Jimeno, Lopez Jimeno, and Carcedo, (1995); and Cunningham, (2006), commercial explosives generate chemical reactions behind the Chapman-Jouet (C-J) plane, following principles of non-ideal detonation. Figure 2.1 shows a schematic representation of the detonation process for both ideal and non-ideal theories. According to Cunningham (2006) and Zhang (2016), an ideal detonation follows the principles of (C-J) theory, where many assumptions are made, the most significant of which are:

- No lateral expansion is produced
- The detonation shock front is considered a flat (plane) wave front
- The chemical reaction is instantaneously completed at the Detonation-Driving Zone (DDZ) which is located between the shock front and the C-J plane

Conversely, non-ideal detonation theory assumes:

- The borehole walls are deformable
- The shock wave front may be curved depending on the diameter of the borehole
- There is a reaction zone behind the DDZ

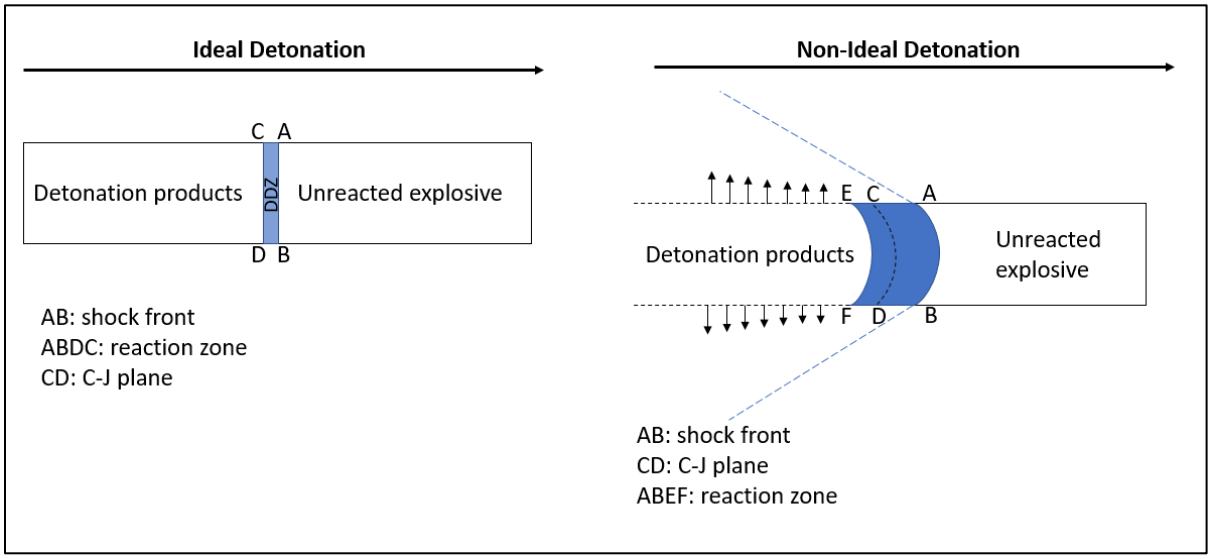

Figure 2.1 Ideal and Non-ideal detonation, after Cunningham (2006) and Zhang (2016)

Regardless of the model adopted to explain the detonation process, researchers do agree rock breakage through blasting is caused by the action of energy resulting from the detonation process, defined as the shock energy, and that due to gas expansion, defined as bubble energy, after McHugh (1983); Lopez Jimeno et al. (1995); and Singh (1999). However, there is no clear understanding or unified theory on which mechanism has greater influence on rock fracture, or the degree of fragmentation attributable to each energy source (Saharan et al., 2006; ISEE, 2011).

Figure 2.2 illustrates the degree of fragmentation produced around a borehole due to the action of the shock (crushed and intense fracture zones) and bubble (extended fracture zone) energy. It is noteworthy that Figure 2.2 does not show the effect of free faces or geologic discontinuities.

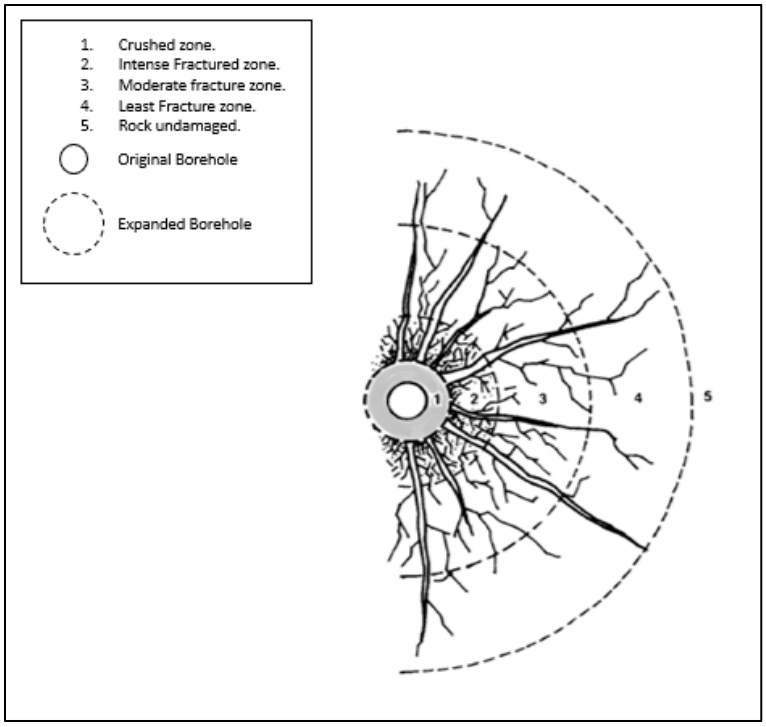

Figure 2.2 Fragmentation around a blast hole, after Atlas Powder Company (1987)

2.2.1 Shock and bubble energy contribution

The rapid chemical reaction on detonation produces a detonation shock wave, which propagates along the explosive column at 2000 to 7000 m/s (Saharan et al., 2006); where the detonation wave front propagates radially out through the rock medium, with the characteristics (Zhang, 2016) of:

- A highly energetic stress wave
- Ability to propagate through a solid, liquid and gas medium
- The wave applies stress to the rock medium exceeding elastic limit
- Pressure increases, with velocity
- The sudden shock transition between the reacted and unreacted explosive creates a nearly vertical front and the shocked material experiences an abrupt increment in pressure, temperature and density

The high pressure of the shock front expands the borehole size by pushing the walls out, exceeding the compressive strength of the rock. Near the borehole walls, this effect compresses and crushes the material, developing the “crushed zone”. According to Esen, Onederra, and Bilgin (2003) and

Zhang (2016), the extent of which depends on the rock properties, explosive type, borehole diameter, coupling ratio and confinement.

Researchers have attempted to estimate the shock front magnitude, despite difficulty in identifying exact limits after a blast and dependency on other variables. Atlas Powder Company (1987) indicated that the ratio between the radius of the crushing zone and the borehole might vary from 1 to 3 hole diameters, Bastante, Alonso, and González (2014) between 1.2 to 4.7 and Lu, Leng, Chen, Yan, and Hu (2016) from 1.2 to 5.

Esen et al. (2003) created a model verified through full-scale field tests carried out by other authors and 92 laboratory-scale blasting tests in a low, medium and high strength concrete blocks, resulting in equation 2.1:

$$r_c = 0.812\, r_B (CZI)^{0.219}, \quad CZI = \frac{P_b{}^3}{K * \sigma_c^2} \quad \text{and} \quad K = \frac{E_d}{1 + v_d} \tag{2.1}$$

Where r_c is the crushing zone radius in (mm), CZI is a dimensionless crushing zone index, r_B is the borehole radius (mm), p_b is the borehole pressure (Pa), K is the rock pressure stiffness (Pa), σ_c is the uniaxial compressive strength of the rock (Pa), E_d is the dynamic Young's modulus (MPa) and v_d the dynamic Poisson's ratio. For E_d calculation, Esen et al. (2003) suggested an equation as a function of the static Young's modulus.

Djordjevic (1999) proposed a two component model to obtain the blast fragmentation particle size distribution in which the crushing zone was estimated with the following relationship.

$$r_c = \frac{r_B}{\sqrt{\frac{24\sigma_t}{P_b}}} \tag{2.2}$$

Where σ_t is the tensile strength of the rock in Pa.

As the shock wave propagates through the rock medium, its radial extension induces tensile stresses in the tangential direction, which in turn generates radial fractures (ISEE, 2011). At greater distance from a borehole, the radial compressive shock wave decreases in amplitude and energy, thereafter propagating only as an elastic compressive stress p-wave (Persson et al., 1994) at velocities of 1000 to 5000m/s (Gokhale, 2011). When this p-wave encounters a free face boundary (air) or a defined change in rock material interface in the rock mass, a portion of the

energy is reflected back into the rock, generating spalling at the free or at inter- faces; while further portion of the energy may be transmitted as a compressive or tensile wave as a function of the incident face engagement angle and the relative change in material impedance (Atlas Powder Company, 1987; Persson et al., 1994; Lopez Jimeno et al., 1995; G. J. Zhang, 1996). According to Gokhale (2011) reflected waves generating spalling travel at velocities of 500 to 2500m/s; roughly half the speed of the initial stress wave, but do not exceed the compressive strength of the rock. However, as the tensile strength of rock is generally lower than the compressive strength, the tensile wave subjects the rock to stresses beyond the ultimate tensile strength, thus still causing the rock mass to further fragment in tension (Gkikizas, 2016). According to Atlas Powder Company (1987) and Persson et al. (1994), when the burden is insufficient for a given charge quantity, rock at the free face will likely experience spalling.

2.2.2 Crack initiation and propagation

The pressure at the detonation front creates shock energy ahead of the reaction product (gas) generation (Lopez Jimeno et al., 1995; Singh, 1999); and the high gas pressure generated by the reaction product, mostly as hot gases, creates a gas or 'bubble' energy and forces the gaseous products to flow through the newly initiated radial cracks (Lopez Jimeno et al., 1995; ISEE, 2011). The difference between the effect of this gas pressure energy and the crack initiating detonation shock pressure in generating a final fragmentation distribution is not clearly understood, due to the difficulty experienced by researchers in separating the two mechanisms given the short time frame within which the entire fragmentation process occurs. However, the challenge has encouraged researchers to progress a variety of analyses and theories.

Atlas Powder Company (1987) stated that gas propagation extends towards crack tips, which permits further crack elongation. According to ISEE (2011), gas pressure also plays an important role in rock fragmentation close to the borehole, contributing to both widening cracks initiated by the shock wave and in crack path deviation generating the opportunity for cracks to cross and intersect with other radial cracks. Djordjevic (2001) stated that the shock energy is used almost entirely in initiating rock breakage, while gas pressures or heave energy moves the rock to create a muck pile. This interpretation is very generalistic and provides little value as to explanation of the fragmentation mechanism.

Some researchers have attempted to investigate fragmentation mechanisms through field measurement, using physical tools such as borehole pressure reaction liners and analysis and interpretation of the resulting pressure history inside a borehole.

McHugh (1983) conducted experimental numerical simulation work, using two cylinders of Plexiglas; one being covered with a steel liner to retain the explosive gases to prevent gas penetration into fractures. An effective liner inducing confining pressure of 6.9 MPa was exerted on the charge, and the resulting crack extent post detonation were then physically measured. Even though the steel liner did not completely retain the explosion product gases, he concluded that the gas pressure not only penetrates the cracks but also, reaches the crack tip to further extend crack length. According to McHugh's work crack length extends by a factor of 5 to 10 solely due to the impact of gas pressure.

Singh (1999) used high strength concrete and Quartzite to conduct experimental work using steel liners inside fabricated and actual boreholes. The resulting fragmentation was compared with that obtained in boreholes without liners. He concluded that both shock and bubble energies contribute to the final fragmentation but, depending on the explosives characteristics, the gas energy may have a greater impact on the fragmentation process.

Nie and Olsson (2001) investigated the action of the shock and bubble energy respectively on the fracturing initiation and propagation process. It is worth mentioning that their prior study had showed the action of the expanding gases was insignificant. To corroborate these initial findings, they performed small-scale experiments using steel tubes inside boreholes drilled in granite blocks. Regarding the fracture mechanisms, they concluded that the shock wave fractures the rock, while the gases move the fragments. In addition, they found that even though the gases did not have a significant effect on the rock breakage, there was a possibility that the movement of the fragments might cause the elongation of the previous cracks.

Olsson and Nie wanted to further investigate the action of shock and bubble energy, and together with Bergqvist and Ouchterlony performed both full bench blasts in a granite quarry and laboratory scale blasts using granite blocks (Olsson, Nie, Bergqvist, and Ouchterlony, 2002). Two field tests were performed in the full bench blasts. In the first trial, steel tubes were used as liners inside twelve boreholes to avoid gas venting and escape through cracks. All the boreholes were charged with a nitroglycerine/nitroglycol explosive, with only 25% of the boreholes were stemmed. In the

second trial, twenty-five boreholes were drilled and 60% were charged with the same explosive used in the first trial and the rest with an emulsion. Also, 10 boreholes were not stemmed. Through measuring crack length, they concluded that the shock wave energy determined the length of the cracks and the gas pressure bubble energy had no substantial effect. However, they stated that no absolute conclusion could be drawn, because the results were not completely clear.

Considering laboratory scale blast tests in granite blocks (Olsson et al., 2002), gauges capable of resisting pressures up to 10GPa, were installed inside the boreholes to record the time-pressure history. In some boreholes, steel lining tubes were also installed. These tests did not yield any important results regarding crack length initiation or propagation.

Similar findings to those of Olsson et al., (2002) were identified by Ledoux (2015). He performed small, medium and large-scale blasts in which carbon resistors were used inside lined and unlined boreholes in grout cylinders. He analyzed the relationship between the pressure history and the physically observed presence of cracks and fragmentation. In the small-scale tests he performed, there was no significant difference to the work of Olsson et al., (2002). In the medium-scale tests, the results were inconclusive. However, in the large-scale trials he conducted, the importance of gas pressure was more significant, to which Ledoux concluded was more likely to have an impact producing large rock fragments.

Although it is evident that some researchers have followed research directions focused on shock energy and have dismissed the contribution of bubble energy in achieving rock fragmentation, their inconclusive results and analysis merely indicate a lack of complete understanding of the entire blast fragmentation mechanism. It is the premise of the work that follows here that both shock and bubble energy make significant contribution to the overall fragmentation of rock, without summarily dismissing the contribution of any one component.

2.3 Explosive Energy

Rock fragmentation occurs by the action of energy imparted to the rock from the point of detonation through to shock and bubble (heave) energies. It is clear that input energy is sourced from the explosive, as the principal component in the process. It is therefore imperative, as a starting point, to understand the determination of the amount of energy that the explosive is able to release under ideal conditions and then progress such considerations from that datum.

Explosives are energetic compounds, such that energy is stored in the explosive as chemical energy, which is subsequently released on detonation to the surrounding rock (Persson et al., 1994). There are two recognizable methodologies for calculating the amount of energy that the explosive releases on detonation. One uses the principles of thermodynamics, while the other is based on experimental testing (Persson et al., 1994; Lopez Jimeno et al., 1995; ISEE, 2011). Each approach has benefits and drawbacks, but there is an adopted standard by manufacturers and users on the methodology favored for explosive energy determination. It is necessary therefore to understand the theoretical concepts behind the analyses to enable further interpretation.

2.3.1 Thermochemistry of the explosives

Thermochemistry is the branch of the science concerned with the change in internal energy, heat transfer, kinetics and mechanisms of a system that take place when chemical reactions occur (Akhavan, 2004). The detonation process may be evaluated on the principle that all energy stored in an explosive is released following the principles of thermochemistry, enabling the determination of the amount of theoretical energy available (Lopez Jimeno et al., 1995; Djordjevic, 2001).

Each explosive is considered to contain a defined amount of energy known as intrinsic or internal energy(U). Following the first law of thermodynamics, an incremental change in internal energy (ΔU) of a system is equal to the heat supplied to the system (Q) less the amount of work (W) done by the system to the surrounding rock (Persson et al., 1994; Lopez Jimeno et al., 1995). In this work, the internal energy (ΔU) is considered as the potential thermal energy that could be released by the explosive.

$$\Delta U = Q - W \tag{2.3}$$

The energy released (heat energy) in a chemical reaction can be calculated both at constant pressure (Q_p) and constant volume (Q_v) (Persson et al., 1994; Akhavan, 2004). When the pressure is constant, the work down by the system is defined as:

$$W = \int_{v1}^{v2} pdv = p\Delta V \tag{2.4}$$

Where p is pressure and v volume, then combining equations 2.3 and 2.4 yields:

$$\Delta U = Q_p - p\Delta V \tag{2.5}$$

Knowing the equation of state:

$$\Delta H = \Delta U + p\Delta v \tag{2.6}$$

Where ΔH is the change in enthalpy, substituting into equation 2.5, it can be re-written as equation 2.7:

$$\Delta H = Q_p \tag{2.7}$$

This implies that the heat content when pressure is constant is equal to the change in enthalpy. Here the reaction products are doing work in addition to raising the temperature. According to Persson et al. (1994), Q_p is also called Detonation Energy and may be referenced to the heat of reaction at the Chapman - Jouguet (C-J) plane. During detonation, the reaction always releases energy, essentially an exothermic reaction, such that Q_p will always be negative.

$$Q_p = -(\Delta U + p\Delta V) = -\Delta H = -\left[\sum_{i=1}^{k} n_i \left(\Delta H_f^0\right)_i - \sum_{j=1}^{l} n_j \left(\Delta H_f^0\right)_j\right] \tag{2.8}$$

Where:

ΔH is the change in enthalpy, n_i is the number of moles of the ith species of detonation products, n_j is the number of moles of the jth explosive used and $\left(\Delta H_f^0\right)$ is the enthalpy of formation at 298.15 K.

If the analysis is considered at constant volume, since no work is done by the system ($W = 0$), all the internal energy is converted to heat and equation 2.5 is simplified as:

$$\Delta U = Q_v \tag{2.9}$$

According to Persson et al. (1994), Q_v is also called the Explosion Energy where no work is done, as the volume remains constant before and after the explosion occurs.

If we assume the generated product gases are ideal, where

$$p\Delta v = \Delta n\, RT \tag{2.10}$$

Then using the standard enthalpy of formation, yields equation 2.11.

$$\Delta U = -Q_v = -\left[\sum_{i=1}^{k} n_i\left(\Delta H_f^0\right)_i - \sum_{j=1}^{l} n_j\left(\Delta H_f^0\right)_j - \Delta n\ RT\right] \quad 2.11$$

Where:

Δn is the difference in moles between products and reactants and R is the ideal gas constant.

To solve equations 2.8 or 2.11, it is assumed not only that the chemical reactions have reached an equilibrium but also that the products of the reaction have the same (Persson et al., 1994).

In summary, if the internal energy of an explosive needs to be computed, the following equation can be used.

$$\Delta U = -Q_v = -\left[\,|Q_p| - \Delta n\ RT\right] \quad 2.12$$

Some researchers emphasize the importance of calculating the internal energy stored in the explosive as the heat content at constant volume as shown in equation 2.9 (Persson et al., 1994; Lopez Jimeno et al., 1995; José A. Sanchidrián et al., 2007), but others state that for practical reasons and because explosives are found in solid or liquid phases, the term $p\,\Delta V$ can be neglected such that equation 2.13 is acceptable (Fifer and Morris, 1993; ISEE, 2011; Klapötke, 2012)

$$Q_v = Q_p = Q \quad 2.13$$

Regardless of the approach adopted, for an explosive of known chemical formula and density, the theoretical internal energy of an explosive can be mathematically calculated. However, most commercial explosives have complex formulae which make calculations complicated and only solvable using computer aided analysis methods. Most computer models consider an "ideal" detonation following the principles of C-J theory, while others adopt a "non-ideal" detonation theory.

A widely adopted thermochemical code, CHEETAH (Fried, 1994), developed from TIGER code (Cowperthwaite and Zwisler, 1974), uses thermodynamic formulae to estimate the amount of detonation product, temperature, volume, pressure and energy as stated by Lu (2001). CHEETAH uses C-J and Zeldovich-Neumann-Döring (ZND) theoretical principles to establish chemical equilibrium for a reaction (Fried, 1994). The use of such codes is widely accepted by the explosive

manufacturing industry as a reliable and practical method to characterize the explosives and define the heat content of complex chemical reactions. However, it is noticeable that each model makes its own assumptions and with appreciable discrepancy between models. In comparing the theoretical energy of explosives reported by different manufacturers, it is essential to understand the principles underlying the manufacturer' energy calculation process and the assumptions made. Such knowledge is rarely declared by those manufacturers.

Industry also uses the term Expansion work (E_{wk}) to quantify the energy from an explosive, also calculated via computer due to its complexity using the laws of thermodynamics (ISEE, 2011). The expansion work energy refers to the mechanical work done by reaction products on 'pushing' the borehole walls (Persson et al., 1994; ISEE, 2011). If the internal energy of the explosive is entirely used to perform work, equation 2.14 may be used, where it is assumed that all the reaction products expand completely from the point of detonation relative to atmospheric pressure, under perfectly elastic efficient conditions.

$$Q = E_{wk} \qquad 2.14$$

Some manufacturers calculate the actual work of an explosive using a 'pressure cut-off'. Here, the theoretical output energy produced at a pressure below a selected defined cut-off is not considered. The latter is due to the fact that at the onset state, some reaction product escapes through cracks, often when gases have expanded to 10 to 20 times their initial volume (Persson et al., 1994). However, this depends on the quality of the rock mass (the geologic fracture density) and the explosive charge characteristics.

2.3.2 Test methods

Experimental tests have been developed to assess the volumetric potential, as the energy and breakage capacity of explosives, to acquire comparator indicators to rate the strength of different explosives. The underwater detonation test, cylinder test, crater test and ballistic mortar test are some of the most widely used tests.

In an underwater detonation test a charge of explosive is detonated underwater and two types of energy are measured: shock and bubble energy. The shock wave energy is a measurement of the brisance or " shattering" capacity of the explosive, while the bubble energy indicates the explosive heaving action, expressed as a function of the volume of gas generated (ISEE, 2011).

Once detonation is initiated, a shock wave is produced and measured from a known position; then, the expansion of the detonation products create expanding gas bubbles that collapse when the hydrostatic underwater pressure exceeds the pressure inside the bubbles, creating a pulse (Lopez Jimeno et al., 1995). This process continues until the bubbles reach the surface and are vented to the atmosphere. The time between the primary shock wave and the bubble induced implosions are then used for calculation. This technique is considered suitable for comparing relative explosive strengths as long as the test conditions remain constant. The major drawback is that the impedance of water is much lower than rock.

In the cylinder test, a set charge of explosive is detonated inside an annealed copper cylinder in an oxygen-free medium. Upon detonation, the cylinder wall expands, recorded as a function of time using a precise motion capture system (Persson et al., 1994; ISEE, 2011). This method is reported as giving a good indicator of expansion energy in turn linked to pressure (Lopez Jimeno et al., 1995). However, the confinement provided by the cylinder is much lower than the actual resistance of rock borehole walls in the field.

The main objective of the crater test is to identify the depth (defined as the scale depth of burial, SDOB) of the centroid of an explosive charge of set diameter, that will produce a defined target volume of fragmented rock (Lopez Jimeno et al., 1995). According to ISEE (2011) field crater tests yield a volume fragmented for a defined set of SDOB conditions from which a strain energy factor may be determined. The drawbacks of this test are that to obtain a reliable conclusion a large number of tests are required and, where for each trial the geological characteristics of the in-situ rock mass are assumed to remain constant.

Finally, in the ballistic mortar test, a steel mortar charged with explosives is attached to a pendulum. On detonation, the pendulum swing (angle or elevation) is measured proportional to energy release (ISEE, 2011). The calculated energy is reported relative to the swing obtained from a reference explosive; TNT or ANFO. The main disadvantage of this test is that the degree of explosive coupling is not similar to that found in rock blasting;, and the reaction products can expand 20 to 30 times the initial charge volume before any pendulum movement (work) is detected (Persson et al., 1994). Table 2.1 summarizes the main advantages and disadvantages of each test.

Table 2.1 Test methods for explosive energy determination

Test	Advantage	Disadvantage
Underwater test	Shock and bubble energy measured	Impedance of water << rock
Cylinder test	Good indicator of expansion energy	Cylinder confinement << Resistance of borehole rock
Crater test	Determine strain energy factor as input for crater blasting	Requires many trials and geological characteristics assumed constant
Ballistic mortar test	Calculates energy indirectly	Explosive coupling differs from field conditions

2.4 Particle Size Distribution (PSD)

There are a number of modes of blast performance evaluation, through pre, post or during blast activity.

In post-blast assessment, the blast outcome through fragmentation, muckpile configuration and fracture damage may be analyzed (ISEE, 2011). Characterization of broken material via particle size distribution are widely used in mining operations, leveraging visual recognition technology tools and algorithms. Analysis of a representative sample of the blasted rock mass is used to identify if downstream fragmentation requirements have been met. Results are usually plotted as the percentage of material passing a standard screen size of decreasing mesh, generating a characteristic "S" shaped curve when plotted in semi-log format. Analysis of such distributions can yield indicators of the efficiency of the blast, as a function of the energy balance at the face through process plant comminution energy requirements.

Several methodologies may be employed to determine the size distribution of blasted material, ranging from those that only require visual observation to more sophisticated computerized image analysis techniques.

2.4.1 Methodologies used to determine the PSD

Qualitative visual observation is one of the simplest and widely used field approaches, but is the most unreliable as a function of the visual interpreter (Lopez Jimeno et al., 1995). It does not

provide any quantitative outcome and depends on the expertise of the observer. It is commonly used for initial observation, which may be the only level of interpretation adopted by a mining operation. It is predominantly used to assess larger size fraction product, representing oversized material indicating a higher powder factor, closer hole spacing or stronger explosive may be required.

Screening of fragmented material by successive mesh size is one of the most accurate methodologies, but time consuming and costly. To get representative results, it is necessary to screen around one quarter of a blasted muck pile (ISEE, 2011) which due to operational constraint is effectively impractical.

Photographic methods to discern fragmented rock particle size distribution, through manually or digital image processing technology is more practical. Originally, delineation of fragments was performed manually using superimposed grids, which was time consuming and impractical (Lopez Jimeno et al., 1995). With improved visual recognition technology, image processing is today automated, making digital image analysis an acceptable, reliable and economical measuring tool to determine the size distribution of fragmented rock (Palangio and Maerz, 1999; Chow, Zeng, Baumann, and Tafazoli, 2012; Kumara, Hayano, and Ogiwara, 2012; Borana, Yadav, and Parihar, 2018).

Today, photogrammetry methods initially used in mining operations for surveying purposes have been adapted for blast fragmentation assessment to determine PSD. According to Lopez Jimeno et al., (1995) and ISEE (2011), such techniques are extremely accurate permitting analysis of broken rock in three-dimensional (3D) space. They also state that, to the point of publication in 2011, as sophisticated and often expensive tools are required, the technique has only been used in high profile cases, boulder analysis and geological studies. More recent (since 2011) technological advances have enabled access to cost effective systems, such as Unmanned Aerial Vehicles (UAVs) or "drones" which, together with photogrammetry techniques, offer new, economic systems for post-blast analysis. According to Bamford, Esmaeili, and Schoellig (2017) use of drone technology enhances results utilizing safe, affordable and efficient processes. (Bamford et al. (2017) concluded that such techniques only take 20% of the time of conventional photographic image processing, with greater numbers of photographs making overall samples of a larger broken

rock mass more representative and finally, human exposure to risk through walking blasted muck piles is removed, negating excessive stoppages for mine operational activity.

2.4.2 Digital Image Analysis

Digital Image Analysis is the photographic-driven approach where image processing is undertaken using computer algorithms. In application to rock blast fragmentation, one of the first proponents of the technique were Carlsson and Nyberg (1983), during the first Symposium on Rock fragmentation by Blasting (FragBlast). The procedure calculates the PSD of a fragmented rock mass as a3D distribution from 2D photographs using mathematical and statistical theory (Maerz, Palangio, and Franklin, 1996).

Independent of how the image capture process is performed, the digital image analysis process may be divided into three general steps: image capture, image processing and reporting.

2.4.3 Image Capture

Generally, image acquisition is performed not only on muck piles, stockpiles or in surge bins, but also as fragmented rock is loaded (shovel bucket) or transported (truck bodies or conveyor belts). Depending on sampling location, photographs must be carefully taken. Two methodologies are used: a) A manual process – whereby photographs of muck pile faces are taken manually using sampling strategies and a common image location reference system, then uploaded to a processing system for analysis; and b) Automatic image acquisition – whereby systems that are usually fully automatic from image acquisition to processing employ real time analysis.

2.4.3.1 Manual Processes

Manual photographic sampling a muck pile after a blast has been proven reliable and practical to discern a PSD (Hosseini, Amirrahmat, and Khoshroo, 2004; Kahriman, Tuncer, Karadogan, and Ozdemir, 2005; Tosun, 2018). However, to decrease error, it is essential that orderly images are acquired in sufficient quantity and of adequate quality for subsequent processing.

The quantity of pictures taken must be sufficient to represent the fragmentation of the entire muck pile. This will vary with the size and heterogeneity of the pile (Palangio and Franklin, 1996). Statistical theory dictates that a larger sample allows estimation to be more precise and more likely to detect differences. The greater the number of images, the better the estimation (Cunningham,

1996; Dahlhielm, 1996; WipWare, 2017). However, such an approach may involve sampling biases, which can be reduced or avoided by employing stringent statistical sampling techniques.

According to Maerz (1996a), there are two methods that can be employed for sampling a muck pile: random and systematic. In the systematic method, best practice divides a muck pile into image sampling areas, avoiding overlapping images within a set area. In the random method, one or more of sectors are picked and pictures are taken randomly while the material is excavated. For systematic techniques, the material covered by all the sectors are photographed and the number of pictures remains constant for each one.

WipWare technical service (WipWare, 2017) states seven possible methodologies to follow:

1. Simple Random Sampling: Any process in which a device predefines the number of samples and time at which they are taken. For example, rolling dice to determine when and how many photographs to take. This process is repeated every day.

2. Systematic Sampling: Intervals of time for sampling are predefined, and no matter the circumstances, the preset time is executed.

3. Stratified Sampling: Rock material is divided into multiple piles with similar volumes, to obtain the same number of random samples from each pile.

4. Probability Proportional to Size Sampling: Similar to 3 above, but the amount of material in each pile is not equal. Random photographs for each pile but proportional to their volume.

5. Quota Sampling: The volume in each pile are not equal and the number of photographs are not proportional to the volumes. According to WipWare (2017), this is not a recommended procedure.

6. Cluster Sampling: The time interval for sampling a number of piles is held constant. This approach is not recommended since variations in the size of material are not considered.

7. Accidental Sampling: Where samples are taken without any systematic or random process. Ironically, although this is the most used field technique it is the least reliable. In general, end users have a poor understanding of statistical sampling.

Image quality is an important consideration. Photographs need to be taken with suitable resolution, lighting, shot angle, lenses, filters and in some cases, scaling objects. According to Wagner (2015),

even though resolution is not considered an important property, higher resolution produces better results; where shooting and lighting features have equal or greater importance in image acquisition. Modern cameras generally have sufficiently high resolution for fragmentation analysis at 18 Megapixel (MP) or greater resolution. However, too high resolution generates oversized image files that slow processing time (WipWare, 2017). In fact, image resolution of 1280 x 960 pixels is sufficient to attain reliable analysis values; but dependant on particle and pile size, lens quality, shot distance and the area covered by a photograph (WipWare, 2019a).

Lighting is critical in rock fragment edge detection, where lighting quality is assessed in terms of intensity, uniformity and contrast. Maerz (1996a) suggests that images should be taken under natural light, avoiding direct sun to prevent shadows. Ideally, each fragment should have a relatively lighter uniform color than the thin dark shadow that surrounds it (created by its 3D nature). When contrast is excessive, a fragment can be interpreted as many parts also called disintegration. When contrast is deficient, particles may be interpreted as merging into a larger interpreted fragment (fusion).

The distance at which the images should be recorded is a function of the size of the pile, the number of fragments and the resolution of the camera; but there is no fixed relationship between such parameters. If images are recorded in too close a proximity, large particles may be omitted. If the shot is taken too far away, fines particles may not be identified. As a rule of thumb, if particles are visually discernable by human sight, an image recording system should similarly discern such particles. Some researchers recommend that each image should contain at least 400 particles (WipWare, 2019a) or 500 to 1500 particles (ISEE, 2011). In addition, large fragments should not occupy more that 20% of the width of the picture (Santamaria, Morley, Franklin, and Wang, 1996; WipWare, 2019a).

To scale images, as may be necessary, scaling objects should be located in the middle of images. One object is appropriate if all particles are located a similar horizontal distance from the camera or no slope is presented (Figure 2.3a). If an image represents a slope, good practice is to use two objects (Figure 2.3b), vertically separated across the rock pile (Maerz, 1996a; Tavakol Elahi and Hosseini, 2017; Split Engineering LLC, 2019a; WipWare, 2019a). The final image scale will be linearly interpreted from the top to the bottom of the slope image, based on the two known scale object positions (Split Engineering LLC, 2019a).

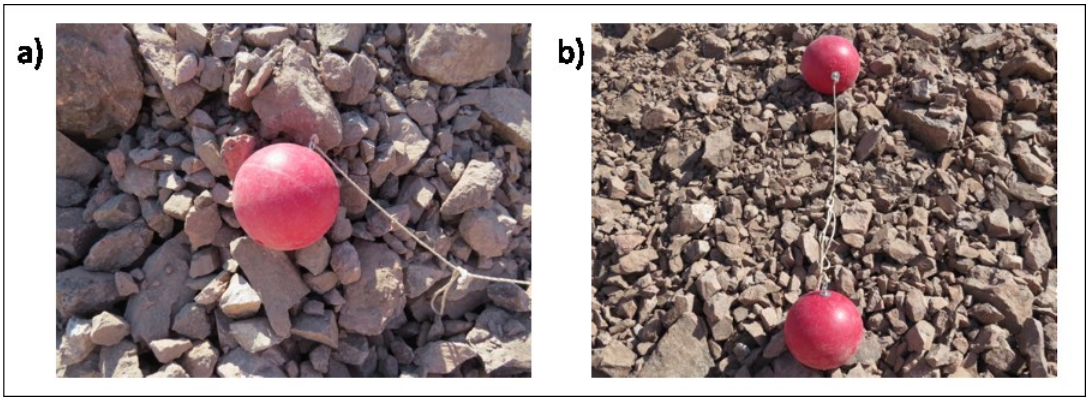

Figure 2.3 Objects used to define scale

Some researchers have used a mix of multiple images with one and two scaling objects in their studies to calculate one final PSD, also known as a Zoom-Merge technique (Maerz, 1996a). Such an approach has been proven as a reliable and practical alternative to increase the size of sampling windows, and it is highly recommended for fragmented rocks with a wide range of particle sizes (Santamaria et al., 1996).

In attempting to improve the fragmentation analysis process outcome and make image capture safer and faster, the latest versions of some software, like Split Desktop version 4 or WipFrag3 iOS, have developed auto-scaling features, where scaling objects are not required (Sameti et al., 2014; Split Engineering LLC, 2016; WipWare, 2019a).

The most recent technological development in this area is the joint use of digital image analysis and UAV systems, also termed UAV image analysis. According to (WipWare, personal communication, February, 2019), in such application a drone with known flight path software takes several aerial photographs to generate a GeoTIFF orthomosaic image, which is then manually uploaded to the system for analysis. For reliable results, the camera should have a resolution greater than 6 MP, the image overlap should be around 80%, no scaling object is needed since an orthomosaic image has an embedded reference and the user must be aware that the system limitation occurs for excessively steep muckpile faces.

2.4.3.2 Automatic Processes

Field use development has led to the creation of completely automated analysis systems where the image acquisition process is fully automatic and can be performed in dynamic situations. For example, while the material is being loaded or transported to downstream processes by truck or

conveyor, real-time analysis is simultaneously performed. WipWare (2019b) and Split Engineering LLC (2019b) developed packages capable of measuring fragmentation in a shovel bucket, truck bodies, on conveyor belts, and in stockpile or surge bins with reporting verification to mining operation control systems.

For automatic image acquisition, sensors are mounted on excavator booms, at fixed points along haul routes, in surge bin drawpoints, at dump areas or above conveyor belts, positioned to take sequential pictures that are then analyzed in real time (J. A. Sanchidrián, Segarra, and López, 2006; J. A. Sanchidrián, Segarra, Ouchterlony, and López, 2009; Chow et al., 2012). In such a system, cameras are set up in optimal positions to provide consistently reliable photographic results, at a known location and distance from the target material, so a scaling object is not necessary. In analysis, any gravity segregation that has occurred in a fragmented blast pile can be determined and then used as a baseline for further interpretation (Palangio and Maerz, 2005).

2.4.4 Image processing and reporting

On images being uploaded to a processing system, they are analyzed as 2D pixelated matrices via statistical and mathematical techniques (Maerz et al., 1996; Santamaria and Fratta, 1996). Generally, in processing images, it is necessary to (a) determine the image scaling, (b) delineate the individual fragments, (c) calculate the size of the fragments, (d) assign the fragments to a specific class size, (e) compute the size distribution and (f) report the results as a table or visually.

a) Image scaling is a function of the mode used to capture the image. If obtained manually, the user should establish the size of the scaling object used to permit an algorithm to calculate a scale factor as the number of pixels over the known dimension $\left[\frac{pixels}{length}\right]$, (WipWare Inc, 2017). When an auto-acquisition system is utilized, the orthomosaic images already have embedded scaling.
b) The next stage is to create an outline profile of the rock edges using a delineation algorithm (Girdner et al., 1996; Maerzet al., 1996; Sanchidrián et al., 2009). This process, also called "Edge Detection", can be performed manual or automatically, where the rate change in the light intensity across a particle is a critical consideration; hence, good contrast to define edges is of prime importance (Downs and Kettunen, 1996; Maerz, 1996a). According to Sanchidrián et al., (2009), the time required to achieve accurate results can be improved if the delineation process is performed automatically and then corrections performed

manually. Although software marketed today is proprietary with no access to code or mathematical methods, Girdner et al. (1996) and Maerzet al. (1996) state that edge detection is performed in two stages. An initial delimitation of blocks using conventional image processing techniques followed by reconstruction techniques, the block edges are enhanced and the profile is finally defined. For a program to recognize a particle, the particle must be completely surrounded by a defined closed edge.

c) Once the system has delineated the blocks or fragments to produce an overall profile or net, 2D size measurements of each individual particle are carried out to then, enable the generation of a 3D distribution using statistical theory. For size defining 2D measurements, a number of different approaches may be adopted. Franklin (1996); and Shanthi, Kingsley Porpatham, and Pappa, (2014), identified the diameter of the particle as the most important parameter to determine, dependant on the method used to carry out the measurement. As an example, Sudhakar, Adhikari, and Gupta, (2006) and Franklin (1996), define the diameters of equivalent spheres.

d) To obtain a 3D distribution, given an assumed particle shape, a third particle dimension is then assigned. Maerz (1996b) stated that particle shapes may be simplified as spheres in which the area of equivalent diameter can be estimated as:

$$d^2 = \frac{4}{\pi}a \qquad 2.15$$

Where d is the diameter of a circle with an area equivalent of a (the area of a non-circular particle).

e) Girdner et al. (1996) identified that Split Software computes PSD with an algorithm that, after delineating the edges of each particle, calculates a particle area and the major and minor axes of the best-fit ellipse to obtain its volume and the actual fragment screen size (de). After field verification, they suggested following equation to determine the actual fragment screen size.

$$de = 1.16 * \text{minor axis} * \sqrt{1.35 * \frac{\text{major axi}}{\text{minor axi}}} \qquad 2.16$$

f) The final step is reporting the result. Digital imaging analysis software generally represents a PSD as a histogram and cumulative curve.

Depending on the applied method as a delineation algorithm, particle shape assumptions, size measurement methods and statistical theory adopted, PSD computations may vary considerably by overall approach and available software. It is therefore important to understand software capability and features to understand the confidence in outcome, the level of reliable automation, flexibility in application and cost. Qian and Tran (1996) compared FragScan, WipFrag and Split software application options with conventional sieving analysis. They concluded that WipFrag and Split reported similar results close to the sieving data, although all three programs underestimated fines.

2.4.5 Benefits and Drawbacks of image analysis

Digital Image Analysis is a widely used technique for post-blast rock fragmentation assessment in the mining industry, where major benefits were summarized by Maerz et al. (1996) and Chow et al. (2012):

- Practical, economical and feasible for any size rock fragments sampled. A major processing time advantage over sieving
- Minimizing or eliminating field production or processing disruptions
- Sampling, processing and reporting is fast and may be fully auto-implemented

Conversely, potential sources of error that users need to be aware of to avoid inaccurate results include:

- The image capture process may be subject to operator bias, making the process unreliable. Employing sampling strategies or relying on automated processes significantly reduces this source of error.
- Delineation of the fragments depends on software algorithms, light quality and sharpness of the images. Essentially, a good image should have clear contrast between the body area of each particle and its edge, permitting an algorithm to delineate more accurately. The main errors occurring in such processes include fusion and disintegration of the fragments. However, those effects can be reduced almost entirely by means of appropriate selection of edge detection variables, minimizing the manual edits required to account for false edges (Edgen and Franklin, 1996; Maerz et al., 1996). Excessive manual corrections give rise to further errors, added through the inherent user subjectivity.

- Sanchidrián et al.,(2006) conducted a study in which manual and automatic modes were compared, concluding that only manual corrections performed during the first minutes of processing are relevant in reaching greater accuracy.
- Missing fines is an issue where most of the fines are either shadowed behind larger fragments or their relative size is very small relative to the overall image size, and hence systems are unable to delineate those small particles. Santamaria et al. (1996) proposed the analysis of multiple images taken at different scale (zoom-merge technique), arguing that any algorithm can delineate the smallest particle, as long as the system is able to detect the fragment edges at the smallest scale in more than a few pixels (e.g. 3 x 3). They concluded that such an approach yields reliable results and avoids not only the use of empirical calibrations for a solution, but also unnecessary and assumed extrapability of results. Maerz (1996a) confirmed this approach and suggested further the determination via an empirically calibration based on full scale sieving, was highly recommended for long term studies.
- The last major source of error is associated with the mathematical approaches used by algorithms to construct 3D fragment distributions from 2D measurements. Through such approaches the shape of fragments is assumed, where empirical equations and probabilistic theory are applied (Girdner et al., 1996; Maerz et al., 1996).

Summarizing in reference to specific mining applications:

- Blast fragment muck piles: Image analysis provides a unique technique that analyzes run of mine material directly resulting from a blast. However, scaling objects are needed, where placement may have safety implications. Here, any manual process intervention likely introduces sampling bias (Palangio and Maerz, 2005).
- Shovel excavation at mine faces: With no need for scaling objects, given the known set dimensions of shovel buckets, image analysis provides a useful study mechanism for bucket fill factor and excavation throughput and cost relative to downstream crushing cost. Providing ongoing feedback with excavation for blast design performance assessment, a non-disruptive and continuous sampling method is effected (Chow, Zeng, and Tafazoli, 2011). However, as material may be further fragmented during shovel loading cycles

(Chow et al., 2012) and since a shovel cannot load oversize fragments, such measurements are excluded.

- Truck haulage: Image processing is useful to study truck body fill factor where similar to the shovel case, there is no need for a scaling object given the known size of a truck body dimensions, which then permits a non-disruptive and continuous sampling method opportunity. However, again since the shovel does not pass oversize material to the truck body, such truck body measurements do not include oversize. Also the transported material may be further broken when dumped at load destination (Chow et al., 2012). The fines in this instance may be more segregated due to the truck vibration during travel movement.
- Conveyor belt haulage: Both from mine pit to processing plant and within processing plant performance, given the ability to position sensors above conveyors at set known distance, and there is no need for scaling objects. According to Palangio and Maerz (2005), sampling segregation may be assumed constant, given the conveyor movement generating a continuous sampling strategy which inherently reduces sampling bias. However, since the rock fragments are usually modified through excavation, primary truck haulage and crushing activities prior to image analysis in a processing plant, the outcome is not indicative of blasting design performance (Palangio and Maerz, 2005).
- Feed or surge bins prior to primary crushers: According to Palangio and Maerz (2005), image analysis of surge bin contained rock fragments is an operational non-disruptive option in a mine, but it is not commonly used due to the need for special sensors identifying material flowing versus 'stuck' in a bin, to counter multiple images of the same broken rock skewing the outcome. Further to relate such PSD back to a blast design would require knowledge on any particle deterioration stages from active excavation face through haulage to the bin location.

2.5 Rock strength

For engineering applications, it is important to understand the basic characteristics of the rock involved and in particular, to be able to characterize it in terms of strength. A huge amount of work has been done over decades to try to determine reliable ways to measure the compressive and tensile strength of rocks.

The unconfined compressive test is one of the most common techniques for rock strength classification and can be performed following the ISRM (2007) or ASTM (2002) standards, in which not only the unconfined compressive strength (UCS) of the rock is determined, but also Young´s Modulus (E) and Poisson's ratio (v). Tensile strength (σ_T) is another critical parameter that influences the failure process in rocks or brittles materials, and can be measured through direct or indirect methods. The Direct Tensile Test (DTS) or Direct Pull Test (DPT) is a standardized procedure (ISRM, 1978; ASTM, 2008) in which a cylindrical specimen is subjected to a uniaxial tensile load until the sample breaks (Figure 2.4, a). The technique has been criticized mostly because the stress distribution along the cylinder is not uniform due to the heterogeneous structure of the material (Van Mier and Van Vliet, 2002; Sarfarazi, Faridi, Haeri, and Schubert, 2015) and both the linkage and gripping system configuration (Van Mier and Van Vliet, 2002; Freiman, 2012). These issues increase the likelihood of producing eccentricity, which in turns can create flexing and torsion causing the rock to break before the ultimate tensile strength is achieved (Van Mier and Van Vliet, 2002; Toutanji, Matthewson, Effinger, and Noumowe, 2003). To overcome some of these difficulties, a "dog-bone" shape specimen has been proposed; however, if the shape is not extremely precise, most of the difficulties found in the regular cylinder shape are still found. Freiman (Freiman, 2012) states that DTS seems to be a simple test, but it is one of the most complex procedures to perform.

Because of these difficulties the development of a simpler test was necessary. The need was for a test which could determine the tensile strength of a specimen without subjecting it to direct tension. One such test is the "Splitting" or "Brazilian" test (BT); an indirect tensile test which is one of the most widely used because the specimen shape and test requirements are easy to achieve. The test follows ASTM D3967–16 (2016b) or ISRM (2007) standards. A compressive diametrical load is applied on a disc sample as shown in Figure 2.4, part b., and tensile failure is induced.

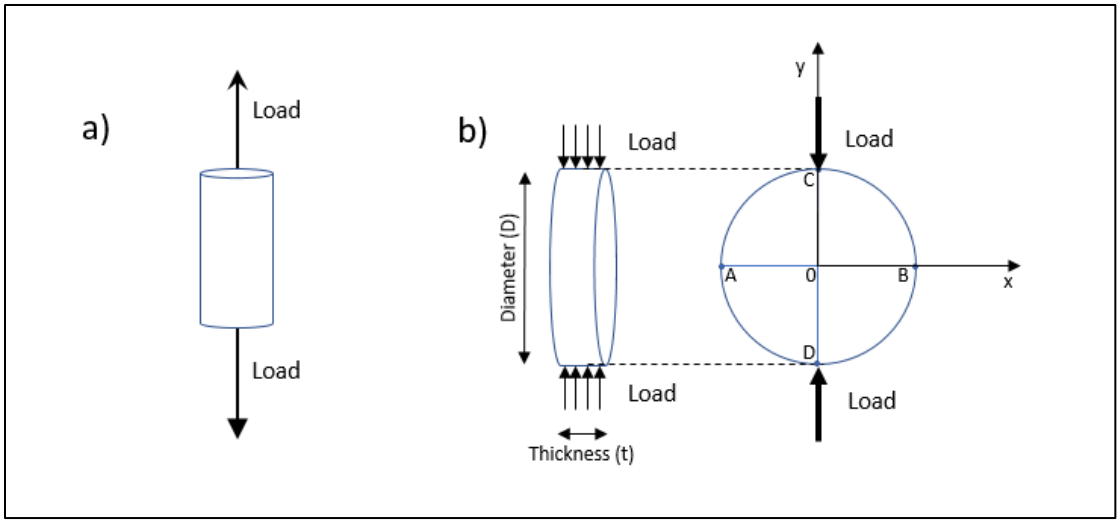

Figure 2.4 Test configuration for: a) Direct tensile test, and b) Brazilian test

The compressive load generates tensile and compressive stresses through the specimen. Hondros (1959) determined the stress concentration along the segment AB with equation 2.17 and segment CD with equation 2.18, when the load is applied over a finite arc and assuming an isotropic and linearly elastic rock (Mellor and Hawkes, 1971). He concluded that in the middle of the sample, point O, the rock experiences both tensile and compressive stresses, the latter being three times greater in magnitude, following Griffith criterion.

$$\sigma_x = \frac{2P}{\pi Dt}\left[1 - \frac{16D^2x^2}{(D^2 + 4x^2)^2}\right] \text{ and } \sigma_y = \frac{2P}{\pi Dt}\left[1 - \frac{4D^4}{(D^2 + 4x^2)^2}\right] \qquad 2.17$$

$$\sigma_x = \frac{2P}{\pi Dt} \text{ and } \sigma_y = \frac{2P}{\pi Dt}\left[1 - \frac{4D^2}{D^2 - 4y^2}\right] \qquad 2.18$$

Where, σ_x is a tensile stress, σ_y is compressive stress, P is the load at failure (N), D is the disc diameter (mm) and t (mm) the disc thickness.

At the center of the disc, when x = 0, equations 2.17 and 2.18 can be reduced to equations 2.19 and 2.20. Equation 2.19 is the standarized formula proposed not only by ASTM (2016b) when flat plattens are used, but aso, by ISRM (2007).

$$\sigma_x = \frac{2P}{\pi Dt} \qquad 2.19$$

$$\sigma_y = -\frac{6P}{\pi Dt} \qquad 2.20$$

For a BT to be valid, the crack must initiate at the center of the specimen and propagate outward along the diametral loading line; however, some researchers have questioned its validity stating that the crack initiation is more likely to begin near the loading point contacts due to the load concentration in this area (Fairhurst, 1964).

To overcome this, some authors have proposed the modification of the shape of the loading platens as suggested in ASTM (2016b), or added an additional thin plastic cushion between the rock and the loading device (Yuan and Shen, 2017). Others like Wang et al. in 2004, suggested a modification in a sample geometry in which a flattened disc sample is loaded along its parallel flat surfaces. This well-known test is recognized as Flattened Brazilian test (FBT) and authors like Elghazel, Taktak, and Bouaziz (2015); Liu, Dai, Xu, Zhao, and Feng,(2018); and Wu, Ma, Cheng, Xu, and Huang,(2018) have used it in their research.

2.6 Summary

The above literature review has summarized the major contributions of previous researchers seeking to better understand the mechanisms of rock breakage through blasting. Those researchers have shown that the energy generated at detonation of an explosive creates shock and gas energy, which are specifically responsible for rock fragmentation. Some researchers have attempted to estimate the efficiency of the fragmentation process, indicating that only a small portion of the explosive energy, referenced as total heat content (Q), is used to fragment the rock, but none has fully quantified the influence of shock and gas energies on a resulting particle size distribution, and so did not consider such a KPI measurement useful in the blasting process performance evaluation.

Further, the principal methodologies adopted by those researchers for compressive and tensile rock strength determination have been outlined, highlighting flaws and benefits. This review has permitted a focus on establishing a new approach to analyzing tensile strength and through this a new approach to evaluating the efficiency of tensile fracture propagation in rock blasting.

3. BLASTING CHARACTERIZATION AT HIGHVALE MINE

This chapter provides some pertinent detailed information on the SunHills Highvale mining operation, specifically related to geology and blasting parameters in current typical use. The data related to the blast design parameters and blast bench geology were provided by the blasting engineer at the Highvale Mine. Explosive strength was initially taken from the technical data sheets provided by the explosive manufacturer, Maxam, where values were checked against reasonable assumptions used with blasting theory to develop similar values. Field trips to the mine were undertaken to gather specific blast design data, rock samples from the blast area to verify rock strength, and pre and post blast photographs for subsequent fragmentation analysis.

3.1 Highvale mine

The TransAltra Utilities wholly owned SunHills LP mining operation, otherwise known as the Highvale Mine, is a surface coal strip mine owned located at Duffield Alberta, on the south of the Wabamun Lake, West of Edmonton. The mine produces about 13.6 M tonnes of low-sulphur-content thermal coal and 100 Mm^3 of overburden and inter-burden annually (Elliott and Wedgewood, 2019). Currently, only 2 of the 7 developed pits are active (pits 5 and 9). Figure 3.1 shows the mine location and permit boundary.

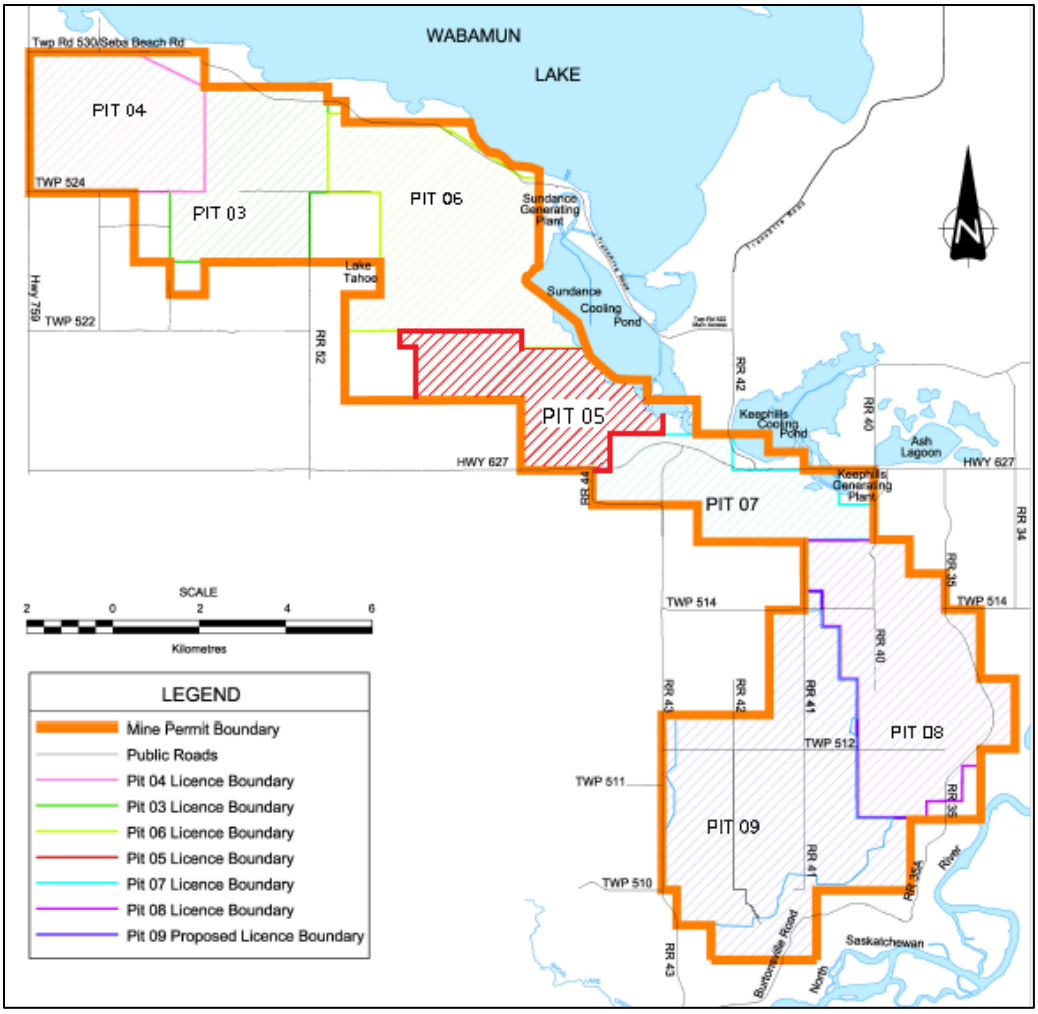

Figure 3.1 Pit boundaries for the Highvale mine, after SunHills Mining L.P. (2018)

As noted by Fenton et al. (1985), the geology at the Highvale Mine originated from glacially thrust bedrock during the Pleistocene era. Bedrock is 15 to 40 m thickness of Upper Cretaceous and Paleocene non-marine coal–bearing rocks (coal measures), with sub-horizontal inter-bedded layers of sandstone, siltstone, and mudstone (Fenton et al., 1985; Elliott and Wedgewood, 2019). According to Fenton et al. (1985), the coal deposit is identified within the Ardley Coal Zone formation which forms part of the Scollard formation (Langenberg, Berhane, Sweet, Marchionu, and Heaman, 2007).

Mine development and production were initiated with blasthole drilling on a 9m x 10.3m equilateral triangle pattern using Ingersoll-Rand DMM3 and Drilltech DK75 rotary drills. The 311 mm diameter blastholes are drilled from surface to coal contact for a 23m average hole depth. Prior

to ANFO (Ammonium Nitrate – Fuel Oil) explosive loading, wet holes were dewatered and lined to reduce adverse detonating conditions, increase explosive performance and reduce noxious as (NOx) emissions. The holes were primed with double 0.45 kg PETN (Penta-Erytritol-Tetra-Nitrate) booster-detonator combinations, placed together at about 1m off the bottom of the drilled hole; avoiding both coal contact that would generate dilution and reducing bottom hole water contact. The holes are then loaded with RIOFRAG (Maxam ANFO product name) mini-prill ANFO to within 7m of the hole collar and stemmed with crushed angular rock. The firing pattern, delays and configuration vary according to operational requirements (muck pile configuration and rock displacement direction), but usually an echelon firing pattern is used. The holes are initiated using DaveyTronic programmable electronic detonators used to prime the boosters.

Once the overburden is blasted, a dragline moves along the strip and excavates the freshly blasted overburden sandstone/siltstone rock, casting it into the previous worked strip. The mine has 3 operating draglines (Caterpillar (formerly Bucyrus) two 8750's, and one 8050) varying in struck bucket capacity from 41 (8050) to 84 (8750) m^3. The uncovered coal seams are then loaded into CAT 776 belly dump trucks in-pit, using a mixed fleet of backhoes, front-end loaders and electric and hydraulic shovels, and hauled to the mine-mouth thermal power plant.

3.2 Blast design parameters analyzed from pit 5

The field information analyzed in this study was gathered from Pit 5, located as shown in Figure 3.2. Currently, Pit 5 is one of the two active pits, from which about 2M tonnes of the 13.6M tonnes per year coal are extracted per year.

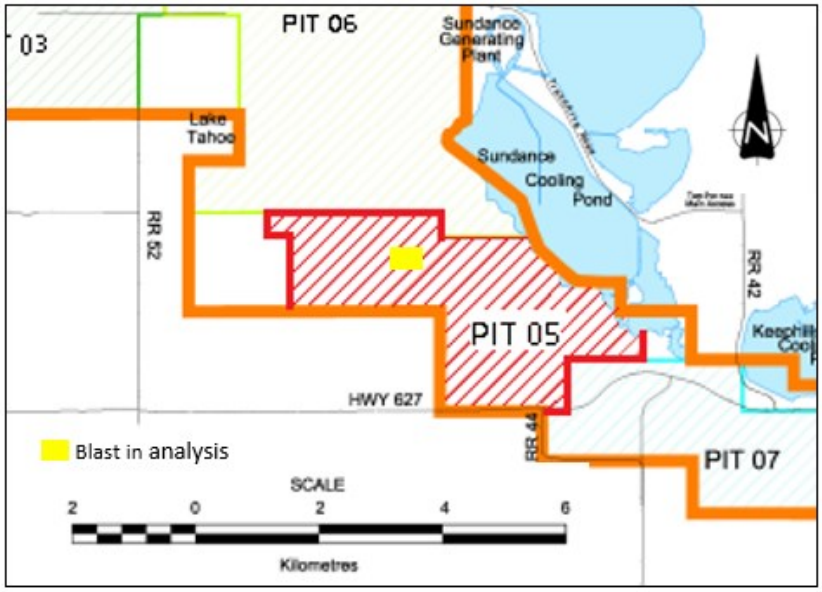

Figure 3.2 Location of blast in analysis-pit 5, after SunHills Mining LP (2018)

The average stratigraphy of pit 5 is illustrated in Figure 3.3. From the top of the upper coal seam to surface, consisting of a lower shale layer approximately 3m thick overlain by a medium grained sandstone that can reach up to 20m thick. Finally, this sandstone is overlain by a shale layer about 16m thick (Wedgewood, personal communication, September 2019).

The total thickness of the coal, which includes 5 coal seams and thin layers of clay inter burden, is about 8m. The average thickness of the two upper seams ranges from 2.5 to 3m and 1m for the lower seams (Wedgewood, personal communication, September 2019).

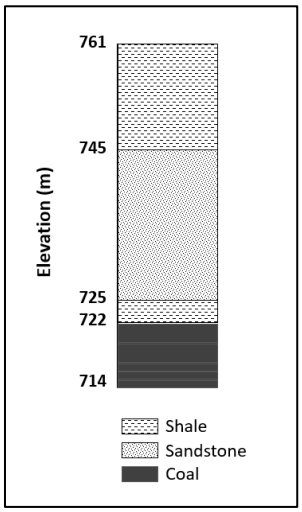

Figure 3.3 Stratigraphic diagram of pit 5

For the test area in pit 5 under consideration, from 745 to 714 m elevation above sea level (asl), the target bench is considered as generally a medium sandstone with a density ranging from 2.07 to 2.32 t/m^3. Note that the 16m shale layer was not presented in this area and a single geological unit was found.

The blast design parameters employed by the mine in pit 5 are described in Table 3.1. Note that the bench height was measured from the top of the bench (745m asl) to the bottom of the coal seam (714 asl).

Table 3.1 Drilling and Blasting design parameters at Highvale mine-Pit 5

Blast design parameter	**Value**
Bench height (H)	31m
Borehole depth (D)	23m
Subdrilling (DS)	0
Backfill (BF)	1m
Borehole diameter (D_B)	0.311m
Borehole angle (α)	90^o, Vertical
Burden (B)	9m
Spacing (S)	10.3m
Drilled Pattern	Staggered blast pattern geometry
Stemming (C)	7m
Explosive Column	15m
Explosive density (kg/m^3)	1050
Numbers of rows	5
Numbers of holes	37
Explosive type	Mini-Prill ANFO
Firing pattern	Staggered blast pattern with progressive delays
Delay time	42ms between rows and 100ms between holes

The blast was designed with 5 rows. The first 4 numbered from the existing ‘old’ highwall free face, termed the production rows, were drilled to the coal contact. The last row, closest to the ‘new’

post-blast highwall, was drilled only to the intersection of the design highwall to minimize damage to the new highwall.

Since most of the holes in pit 5 are 'production' rows, the analysis performed in this thesis is based on their loading configuration. A typical hole loading design for Pit 5 is shown in Figure 3.4.

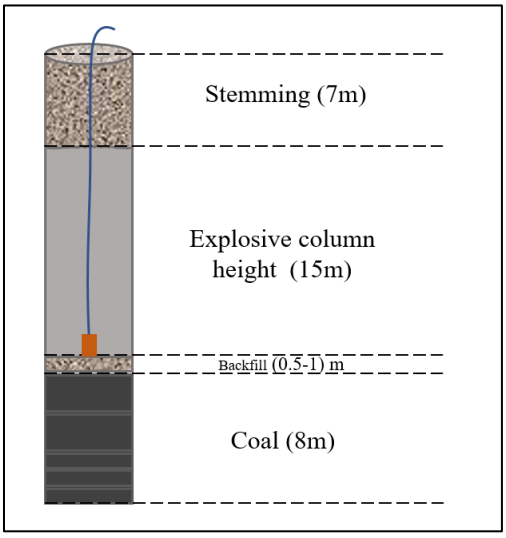

Figure 3.4 Typical design loading configuration for production holes

It should be noted that the blast design is not always followed during blast operations' implementation. According to mine records, an average of 1247 kg of explosive per production hole is used per blast, which translates to boreholes being charged with about 50 kg more explosive than stipulated by design. This implies that either (a) voids are present in the rock mass, resulting in more explosive being loaded than designed, or (b) additional explosive is loaded as normal practice, effectively modifying the blast design parameters. For simplicity it was assumed that the stemming column was less than 7m, so using the density of the explosive shown in Table 3.2 and a borehole diameter indicated in Table 3.1, the actual value of explosive column (L) was calculated as follows:

$$L = \left[\frac{\left(\frac{\text{kilogram of explosive}}{\text{Density of explosive}}\right)}{\left(\frac{\pi D_B{}^2}{4}\right)}\right] = 15.63 \text{ m} \qquad 3.1$$

Knowing that L is equal to 15.63m, the new stemming value (C_{new}) for production hole is 6.37m. It should be borne in mind that this is a theoretical equivalency only.

3.3 Explosive energy determination from the manufacturer information

The explosive used in the field test was ANFO, Maxam trade named RIOFRAG^{TM}, which is a mixture of high density industrial mini-prill (ammonium nitrate) and fuel oil (to 6% of the final product by weight). The mini-prills require specific fuel oils to be blended. At Highvale mine, CFE-150 is used which as recorded on the Material Safety Data Sheet (MSDS), it is a mixture of distillate fuel oil and obsolete base oils. See Appendix A

Due to the complexity of the fuel oil composition, the total heat content in the chemical reaction was not possible to compute using equation 2.8 or 2.12 referenced in chapter 2. Instead, theoretical values reported by the manufacturer (table 3.2) in the Technical Data Sheet (TDS) were utilized, which inherently introduces an unquantifiable error. The manufacturer adopts the AN strength reporting practice for evaluating relative energies with ANFO as a standard.

Table 3.2 Explosive theoretical energy rating, after Maxam (2015)

Average in-hole density (kg/m^3)	1050
Velocity of detonation (VOD) (m/s)	(4300-6100)
[1]Energy (kJ/kg)	3782.3
Relative weight strength RWS_e (%)	102
Relative bulk strength (%)	127

According to Maxam, the explosive manufacturer, in calculating absolute weight strength (AWS) no cut-off pressure was used (Fortelka, personal communication, July 2019). Hence, it is assumed that AWS is equal to the total theoretical heat energy that the explosive is able to release through detonation (Q) having units of [energy/mass].

Since RWS (heat content per unit of mass of explosives as related to the ANFO) is the value reported, AWS was computed using equation 3.2, and using $\mathrm{AWS_{ANFO}}$ equal to $3723.8\mathrm{kJ/kg}$

$$\mathrm{AWS_e} = \mathrm{RWS_e} * \mathrm{AWS_{ANFO}} = 102\% \text{ x } 3723.8\mathrm{kJ/kg} = 3798.3\mathrm{kJ/kg} \qquad 3.2$$

[1] ANFO as the reference explosive with a standard density and absolute energy of 840kg/m^3 and $3723.8\mathrm{kJ/kg}$ respectively and calculations are done with W-DETCOM code.

When comparing AWS_e with the energy value reported in the TDS of 3782.3kJ/kg, shown in Table 3.2, there is a discrepancy of 16kJ per kilogram of explosive. This could be caused by rounding error, or because the energy value reported by the manufacturer is related to other type of energy. However, since the manufacturer only specified their methodology for AWS calculation, 3798.3kJ/kg will be the Q thermal energy value used for future analysis.

$$Q = 3798.3\text{kJ/kg} \tag{3.3}$$

An appropriate ratio between AN and fuel oil by weight depends on the chemical composition of the fuel oil, which according to Lopez Jimeno et al. (1995); Gokhale (2011); and ISEE (2011), it should be about 94.3 : 5.7 and 94 : 6, at which not only Q, sensitivity and VOD reach their maximum values but also, the production of noxious gases are minimized. At the Highvale mine, the amount of fuel oil in the mixture is 6.1% of the final product by weight, which agrees with the theory, see Figure 3.5.

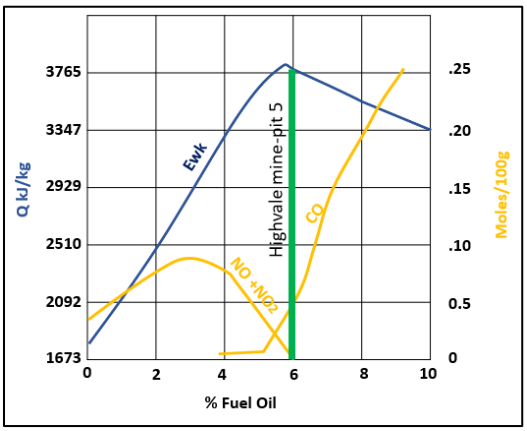

Figure 3.5 Variation of Q and fumes released with percentage of fuel oil, adapted from ISEE (2011)

The velocity of detonation (VOD) indicates the speed at which the detonation wave travels through the column of explosive and hence, it can be used to evaluate an explosive performance. The theoretical VOD suggested by the manufacturer for RIOFRAG^{TM}is from 4300 to 6100 m/s and Elliott and Wedgewood (2019), from field measurements, found that it reaches 5169.2 m/s under the Highvale mine geologic conditions. This is indicative of an explosive with a specific mixture of AN and fuel oil, generating a specific explosive density, performing within the geometric and geologic confinement within the boreholes used. Additionally, the VOD measured at the mine

indicates that the explosive is effectively unaffected by water and has not been deteriorated with age (ANFO cycling).

3.4 Rock strength measurements

Through field observation, it was noted that the target field blast bench consisted mostly of a medium grained sandstone, but there were no records of its specific strength. Hence, a first step for rock characterization was collecting rock samples from the bench area for laboratory analysis. Four blocks of rock were gathered (see Figure 3.6 part a) at the mine, and taken to the Surface Mining Research Laboratories at the University of Alberta where they were initially cored as shown in Figure 3.6 part b.

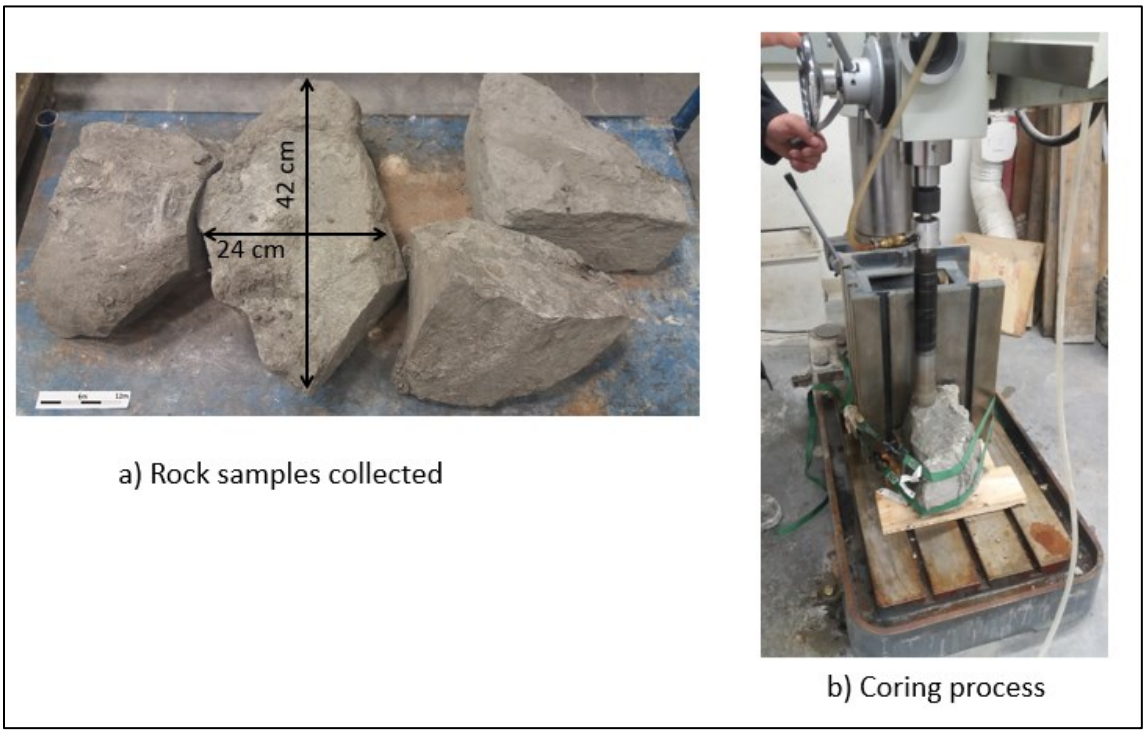

Figure 3.6 Part a) Block samples collected. Part b) Coring process

The first laboratory test performed was a Point Load Index Test (PLT) following the ASTM D5731–95 standard test method (ASTM, 2016a). This is a recognized indirect test for uniaxial compressive strength (UCS) determination of rock, in which a compressive concentrated point load is applied between two conical platens to a rock specimen until failure. The procedure and rock preparation are simple, making it a practical and cost effectively technique. It is worth mentioning that the ASTM recommends three procedures for Point Load Strength Index

determination (axial, diametral and block or irregular) and depending on the methodology used, not only the specimen shape and dimensions change, but also the formulation associated. Authors like Bieniawski (1974), Li and Wong,(2013) have proved the consistency of the results, no matter the approach followed. Also, according to Rusnak and Mark, (2000) the axial test is more analogous to UCS test.

In this analysis, 16 discs of rock were prepared using a cut-off diamond blade saw; then tested following the axial test suggested by ASTM PLT test procedure (ASTM, 2016a), with the results summarized in Table 3.3 and Figure 3.7. The length to diameter ratio was about 0.5 with an average length of 23.13mm. The Point Load tester (RockTest model PLI) was used with an effective piston bearing area of 9.48 cm^2. The load to failure (P) in kN, was obtained using equation 3.4.

$$P = M_p \, x \, A_e \tag{3.4}$$

Where M_p is the maximum pressure reading from the machine in kPa and A_e is the effective area of the piston bearing area in m^2.

Once the load at failure was obtained, the uncorrected point load strength index (I_s) was calculated by the equation below, where D_e is the equivalent core diameter in mm.

$$I_s = \frac{P}{D_e^2} \qquad D_e = \frac{4(\text{length x diameter})}{\pi} \tag{3.5}$$

Since not all the specimens have a same diameter of 50mm, a size correction factor (F) was applied by equations 3.6 and 3.7 as suggested by ASTM (2016a).

$$I_{s(50)} = F \, x \, I_s \tag{3.6}$$

$$F = \left(\frac{D_e}{50}\right)^{0.45} \tag{3.7}$$

Where $I_{s(50)}$ is the size corrected point load test index, and F is the correction factor.

Table 3.3 Values obtained through Point Load Test (PLT)

Sample	Length (mm)	Length/Diameter	P (kN)	A_e (mm^2)	I_s (MPa)	$I_{s(50)}$ (MPa)
1	25.2	0.51	9.14	1,251.5	5.74	5.18
2	25.2	0.52	8.32	1,231.0	5.31	4.78
3	26.0	0.53	7.68	1,283.5	4.70	4.27
4	25.3	0.52	7.43	1,234.5	4.73	4.26
5	26.0	0.52	9.54	1,296.7	5.78	5.26
6	25.0	0.58	5.59	1,073.0	4.09	3.57
7	25.0	0.59	7.87	1,065.7	5.80	5.05
8	24.8	0.58	7.62	1,055.0	5.67	4.93
9	25.1	0.58	6.50	1,077.1	4.74	4.14
10	25.1	0.51	10.39	1,230.3	6.63	5.97
11	25.0	0.58	7.32	1,069.0	5.38	4.69
12	26.4	0.52	10.12	1,335.8	5.95	5.46
13	26.4	0.52	8.44	1,330.2	4.98	4.56
14	26.0	0.52	9.71	1,311.4	5.81	5.31
15	26.0	0.52	11.07	1,308.9	6.64	6.06
16	26.5	0.52	10.03	1,338.0	5.89	5.40

Figure 3.7 Part broken samples under Point Load Test (PLT)

Authors like Bieniawski, (1974); Hassani, Scoble, and Whittaker, (1980); Smith, (H. J. Smith, 1997); Alitalesh, Mollaali, and Yazdani, (2015); Elhakim, (2015); ASTM (2016a) have published

several equations to correlate UCS and PLT for sandstone or other sedimentary rocks. However, the Bieniawski approach is one of the most used and the suggested value by the D5731-16 ASTM (2016) standard. The approach suggests that for a UCS determination, a correction factor (K) must be applied by equation 3.8. However, as the diameter of the samples was not identical, the value of $I_{s(50)}$ was used instead of I_s. For this analysis, K will be equal to 23 as stated by D5731-16 ASTM (2016).

$$UCS = K \times I_s \tag{3.8}$$

The average UCS calculated for the 16 samples was 113.4 MPa, with a standard deviation of 15.44. However, it should be noted that since a correction factor was used, the UCS value estimated is just an indicator of the resistance of the rock. According to Bieniawski (1974), the rock is located in the lower limit of a high strength material.

To further investigate the mechanical parameters of the rock, and to corroborate the results obtained from PLT, two UCS tests were performed following the procedure suggested by D7012–14 ASTM (2014) standard. Initially the end surfaces of the samples were cut and ground to ensure their flatness and parallelism. The average length of the samples was 102 mm and the length to diameter ratio of 2:1. The specimens were tested in a Material Testing System Series 793 (MTS testing machine) at a constant strain rate of $2.46x10^{-5}/s$. The axial strain was obtained from the MTS machine, and an Epsilon Extensometer- E86505 was used to record the lateral (circumferential) deformation of the samples. The resulting graphs are shown in Figure 3.8.

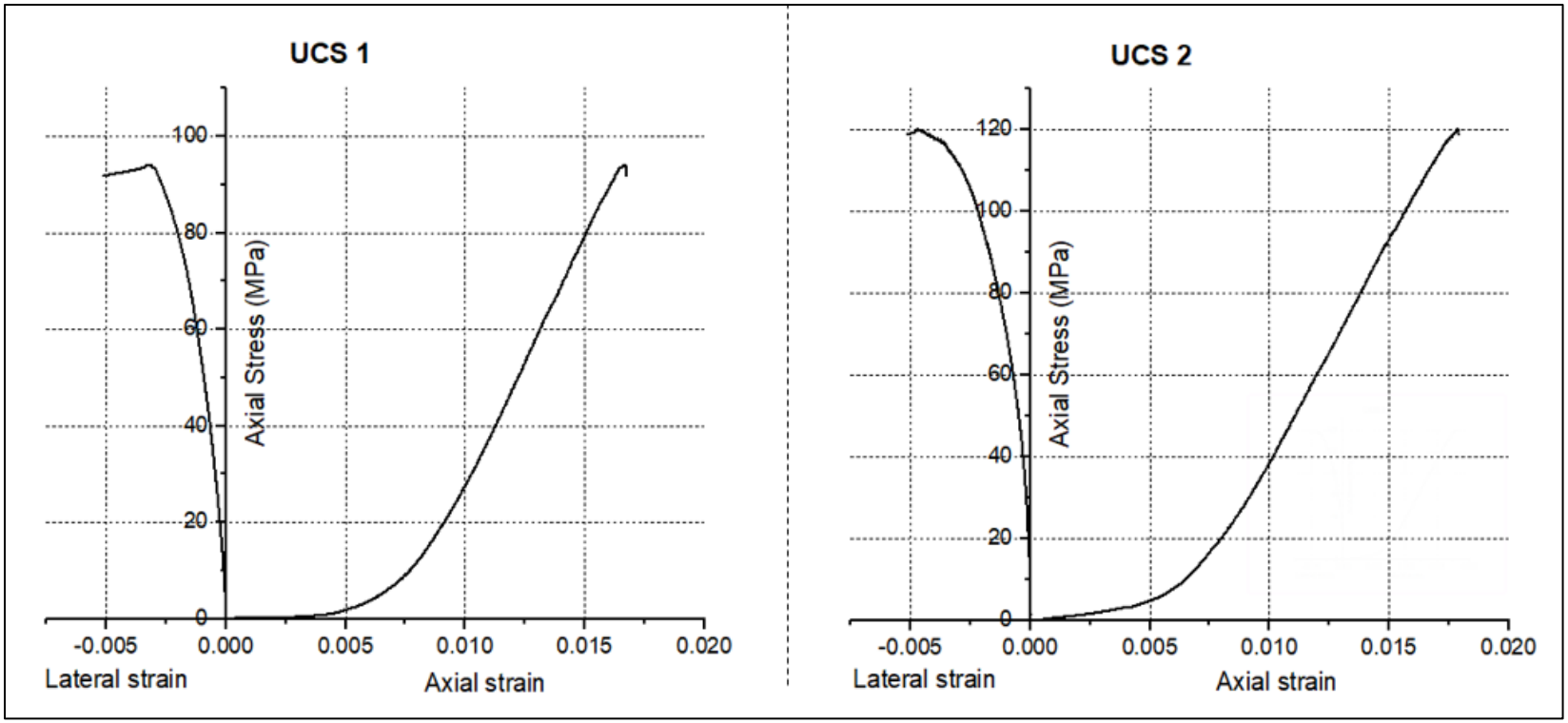

Figure 3.8 UCS test results

The average Young's modulus (E) was calculated using a linear least squares fit of the straight line of the Axial stress-strain curve. The Posisson's ratio (v) was estimated by dividing the E value previously calculated and the slope of lateral strain ratio which was calculated using the same approached used for E (linear least squares fit).

Table 3.4 UCS, Young's Modulus (E), Poisson's ratio (v) and Shear Modulus (G) of the Sandstone at Highvale mine

	Test 1	**Test 2**	**Average**
UCS (MPa)	94.05	120.2	107.1
Young's Modulus - E (MPa)	10654	10796	10725
Poisson's ratio	0.28	0.28	0.28
Shear Modulus – G (MPa)	8100.3	8043.4	8071.4

Comparing the Uniaxial Compressive Strength values obtained from PLT and UCS tests, it can be seen that the results are close, indicating that the PLT is a practical and reliable estimation tool for UCS determination. The values obtained by the UCS test confirms that the sandstone at Highvale mine is a strong sedimentary rock. It is worth mentioning that for future calculation, the average values indicated in Table 3.4 will be used in Chapter 5.

4. PARTICLE SIZE DISTRIBUTION (PSD)

Broken material is commonly characterized using a particle size distribution (PSD), permitting a fragmentation performance evaluation. In the extractive industries and civil engineering fields, image analysis systems (IAS) have been widely accepted as field tools to determine and analyze the shape and size distribution of fragmented or crushed rock. Documentation published since 1980 show progressive technological and reliability improvement, that have made IAS trusted tools for post-blast assessment (Carlsson and Nyberg, (1983); Maerz et al., (1996); Maerz (1996a); Qian and Tran, (1996); Dahlhielm (1996); Palangio and Maerz, (1999); Moser, Grasedieck, Olsson, and Ouchterlony, (2003); Ouchterlony (2003); Chow et al., (2011); Debnath and Jha, (2013); Shanthi et al., (2014); Choudhary and Mishra, (2016).

In this chapter the PSD of blasted rock generated at pit 5 in the Highvale mine has been determined using Wipfrag 3 software (WipWare, 2019b) as the post-processing tool selected for image analysis. The tool was carefully chosen based on widest use by the mining industry in Canada and US.

4.1 Determination of particle size distribution at Highvale mine

As cited by Palangio (1995), WipFrag is an IAS originally developed in the mid 1980's by the University of Waterloo; initially named the Waterloo Image Enhancement Program (WIEP). The system was created with the goal of determining the size distribution of blasted rock using increasingly powerful computational technology. Although the mathematical algorithms used by WipFrag are proprietary, in general, the software uses 3 general stages: image capture, image processing and reporting. According to Maerz et al., (1996), the system creates a 3D distribution from a 2D matrix of pixels via applying geometric probabilistic theory.

4.1.1 Rock pile sampling and Photograph

As photographs represent the input data for the WipFrag system, it is essential not only to carefully select the location and viewpoint from which images are taken, but also to assure that such images do in fact reflect the actual rock fragmentation. At the Highvale mine, the blast muck pile and the dragline bucket were selected as suitable locations to acquire images. However, the muck pile, as the immediate post-blast view was chosen for two reasons:

a) Only a simple camera was necessary to take the photographs, and by employing sampling strategies, the introduction of errors or bias could be reduced to a minimum. According to Palangio and Maerz (2005), and Shahram and Nima (2009), using the dragline bucket option would have required a robust camera mounted within an operational hazardous location and a more sophisticated system to maintain integrity should have been necessary.

b) The fragmentation of the muck pile resulted from the explosive energy only; whereas further fragmentation, could be produced by the action of loading by a dragline bucket.

The next step was to discern which one of the WipWare (host company) licenses offered was the most convenient. Given the two options: WipFrag for iOs App and Windows; the difference was how the images are acquired and speed of output. According to WipWare Inc, (2019b), WipFrag for iOs App is characterized mainly on the ability to analyze images with or without scaling objects, making it more convenient for steep muck piles, where placing scaling objects introduces a safety concern. WipFrag for iOs App produces essentially instant output. However, use of the application is limited by the view point options for image acquisition, and represents a new and largely undocumented unproven option. Conversely, WipFrag for Windows processes images incorporating scaling objects or images taken by drones with onboard GPS negating the need for scaling objects. With WipFrag, output is generated post image acquisition.

However, after careful consideration of the site access safety challenges, the iOS App license was chosen on the grounds of flexibility to analyze images with and without scaling objects. It is worth mentioning that blast bench heights at the Highvale mine range from 22 to 35 m, which pose significant safety risk for access to place scaling objects. The drone option was discarded after trialing, as the Highvale mine steep slopes would likely produce biased results (WipWare, personal communication, February 2019).

Images were taken immediately after a blast, once it was safe to do so. An initial observation of the muck pile was undertaken to identify a representative sampling area. Figure 4.1 shows the scale of the muck pile in the manual observation phase immediately post blast.

Figure 4.1Initial inspection of the muck pile

Fifteen images were acquired for varying location over the surface of the muck pile, using a random sampling methodology. The choice of image location was primarily based on (a) access safety, (b) minimizing delay in dragline operations and (c) avoiding image overlap within the same acquisition sector. The auto-scaling software feature was not applied given the (i) mine operational constraints and (ii) the inability to achieve mandatory technical specifications in the field. To scale images, wooden survey laths of length 51cm (20") were used. As recommended by Maerz (1996a), and Santamaria, Morley, Franklin, and Wang (1996), to achieve more reliable results and due to the heterogeneity of the muck pile, the Zoom-Merge technique was applied. Thus, in some images two scaling objects were placed (Figure 4.2 a), while for images where fragments were evidently smaller, the camera was zoomed in with only one scaling object (Figure 4.2 b).

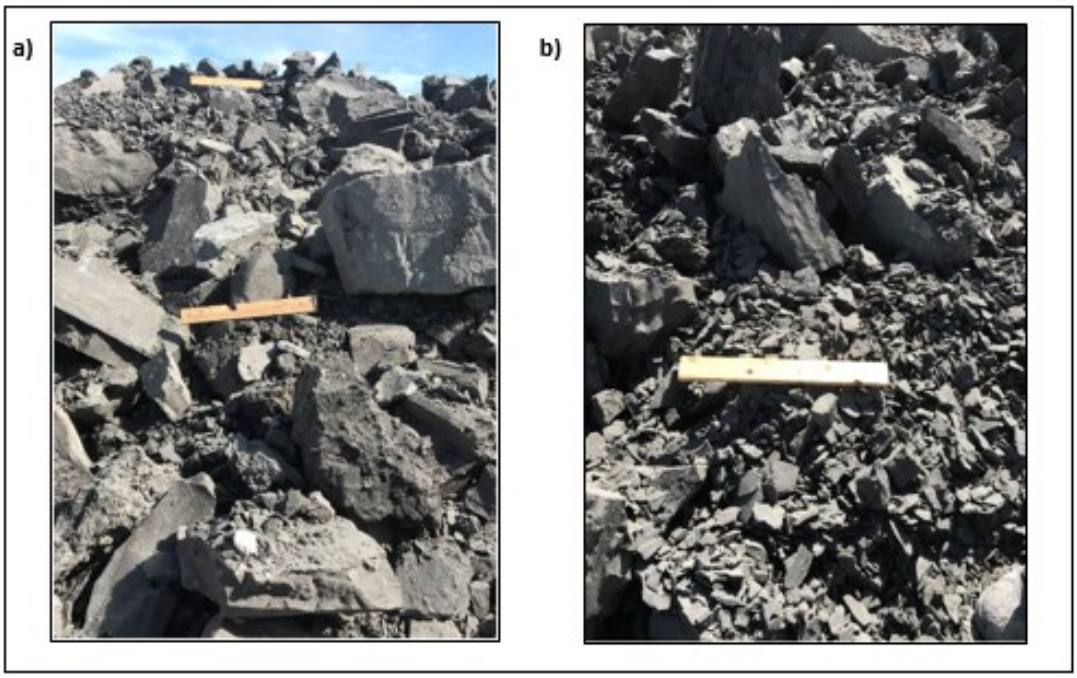

Figure 4.2 Images with one and two scaling objects: The Zoom-Merge technique

4.1.2 Image Processing and Reporting

Given natural lighting conditions (for a given sun azimuth), a few images presented shadows between fragments, as evident in Figure 4.2, making auto delineation of particles unreliable, in which major errors generated in “fusion” of particles into a larger fragment. As such, boundary delineation was initially performed automatically by the software, followed by manual editing to improve the accuracy of the net. Figure 4.3 shows the image from figure 4.2(b) with final net delineation. Some zones at the image border were excluded from the analysis as (a) the particle images were insufficiently sharp, (b) some fragments were truncated at the image edge, or (c) the image displayed regions outside the muck pile such as landscape or sky. Additionally, on analysis the scaling object was removed from the image, figure 4.3.

To maintain a consistent analytical methodology, the same analysis procedure was performed for all images even though shadows were observed in only few images. Finally, the fifteen images were merged to attain the PSD presented in Figure 4.4.

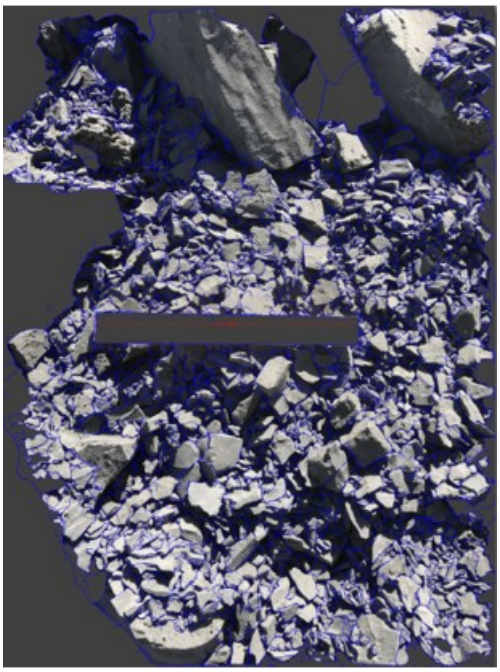

Figure 4.3 Fragments edges delineated

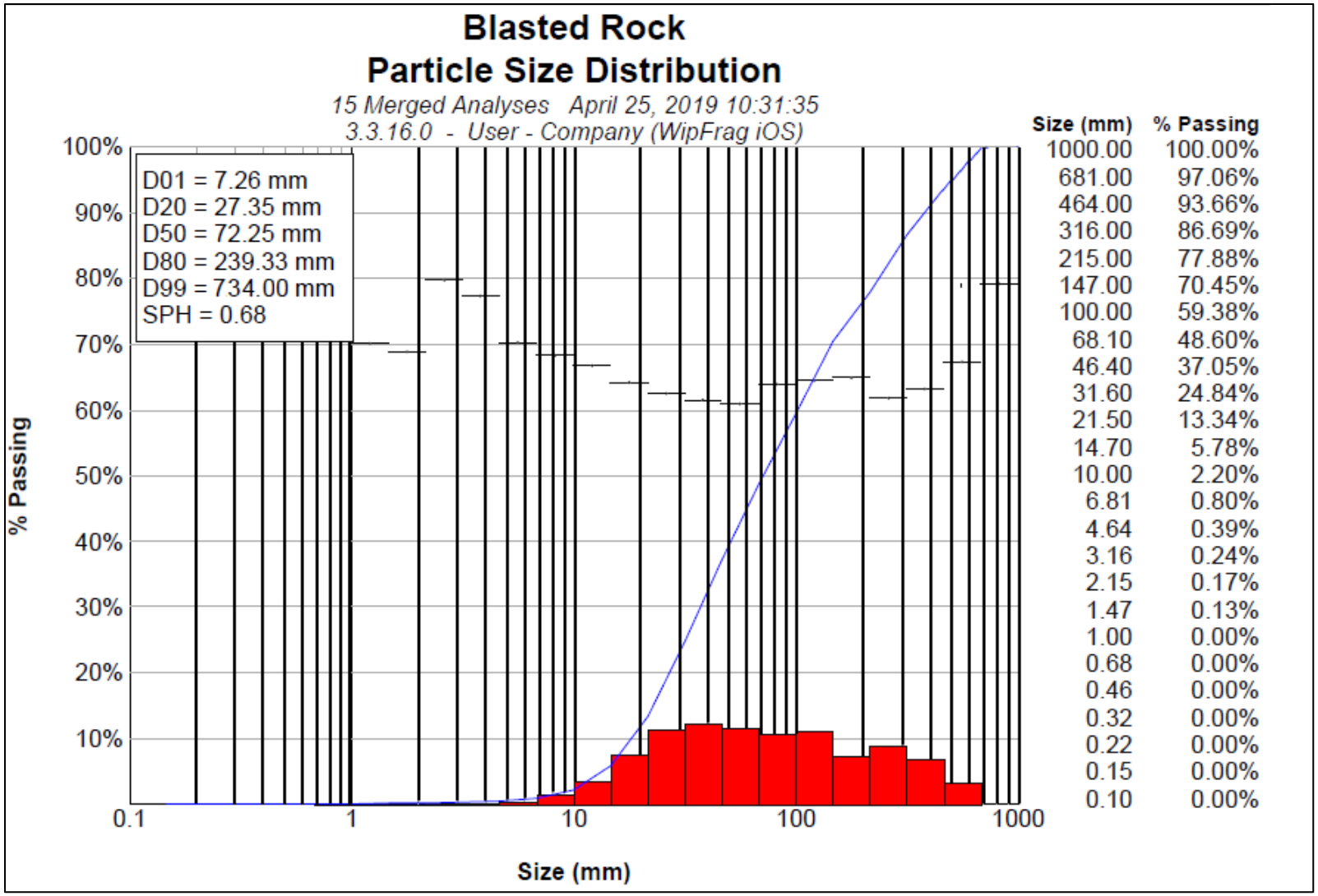

Figure 4.4 Particle Size distribution of Highvale mine-pit 5

4.1.3 Results analysis

In Figure 4.4, the cumulative percent passing is represented by the blue trace, generated from the data shown to the right of the plot. The percent passing (vertical axis) indicates the amount of material smaller than a specific size that would pass a screen size (horizontal axis). The co-plotted histogram indicates the amount of material that would be effectively retained for each bin passing size. By default, the software divides the range of data values into 25 size classes or bins.

The horizontal bars evident in the plot indicate the average sphericity (SPH) measured per size class. According to (WipWare, personal communication, February 2019), SPH values are calculated in a 2D plane as the ratio between the longest dimension of the particle, also called "length", over the longest perpendicular dimension (width), having values from 0 to 1. The average SPH for all the distribution was 0.68, indicating that the particles are far form being spheres or cubes and are more likely to be elongated.

For the blasted rock analyzed, the mean particle size (D50) was 72.25mm. Of interest to downstream crushing operations in processing (had it been applicable to the mine) D80 was 239.33mm which would be a prospective feed size (F_{80}) in crushing consideration. The smallest and largest particle size delineated was 1.47 mm and 734 mm respectively.

The effectiveness of cast or bench blasts for dragline operations through PSD for blasted rock is sparely reported in the literature. Price Waterhouse Coopers (PwC) Mining Intelligence and Benchmarking (2014) study, states that for maximum dragline performance, the biggest particle size should be smaller than one third the bucket width. Frimpong, Somua-gyimah, Nyaaba, and Gbadam (2019) proposed a size distribution ranging between 0.1% and 26 % of the dragline bucket width.

Table 4.1 illustrates actual values from field measurements at the Highvale mine and suggested values for improved dragline performance. Given the literature indications above and knowing the dragline bucket size and width of 76m^3 and 5m respectively, the Highvale mine has an opportunity for improved dragline performance through blasting practices. Effectively the explosive energy (shock and gas energy) could be better distributed to assure a blasted rock muck pile with fewer "fines" and greater larger fragments.

Table 4.1 Actual values from field measurements at the Highvale mine and suggested values for improved dragline performance

Actual dragline bucket size and width: 76 m^3 and 5m respectively.			
	Actual Size Distribution indices at Highvale mine	**Indices proposed for maximum dragline performance**	
		(PwC Mining Intelligence and Benchmarking, 2014)	(Frimpong et al., 2019)
Minimum fragment size (mm)	1.47		5
Mean fragment size (D50) (mm)	72.25		
Maximum fragment size (mm)	734	1667	1300

5. TENSILE STRENGTH DETERMINATION

The tensile strength (σ_T), was first introduced by Griffith (1920), an important rock parameter for fracture initiation and propagation. Several direct and indirect approaches to its determination exist, based on repeatability, practicality and economy. In this chapter, the widely recognized Brazilian Test (BT), is used not only for rock tensile strength estimation but also as a tool, specifically here, to compare the mechanism of rock failure for fracture propagation during blasting.

In addition, a new approach to estimate σ_T is introduced, and the results are compared with those obtained from the BT and the pull (direct tension) testing techniques. The results are analyzed and compared, and their benefits and drawbacks detailed. The methodology is summarized in Figure 5.1 below:

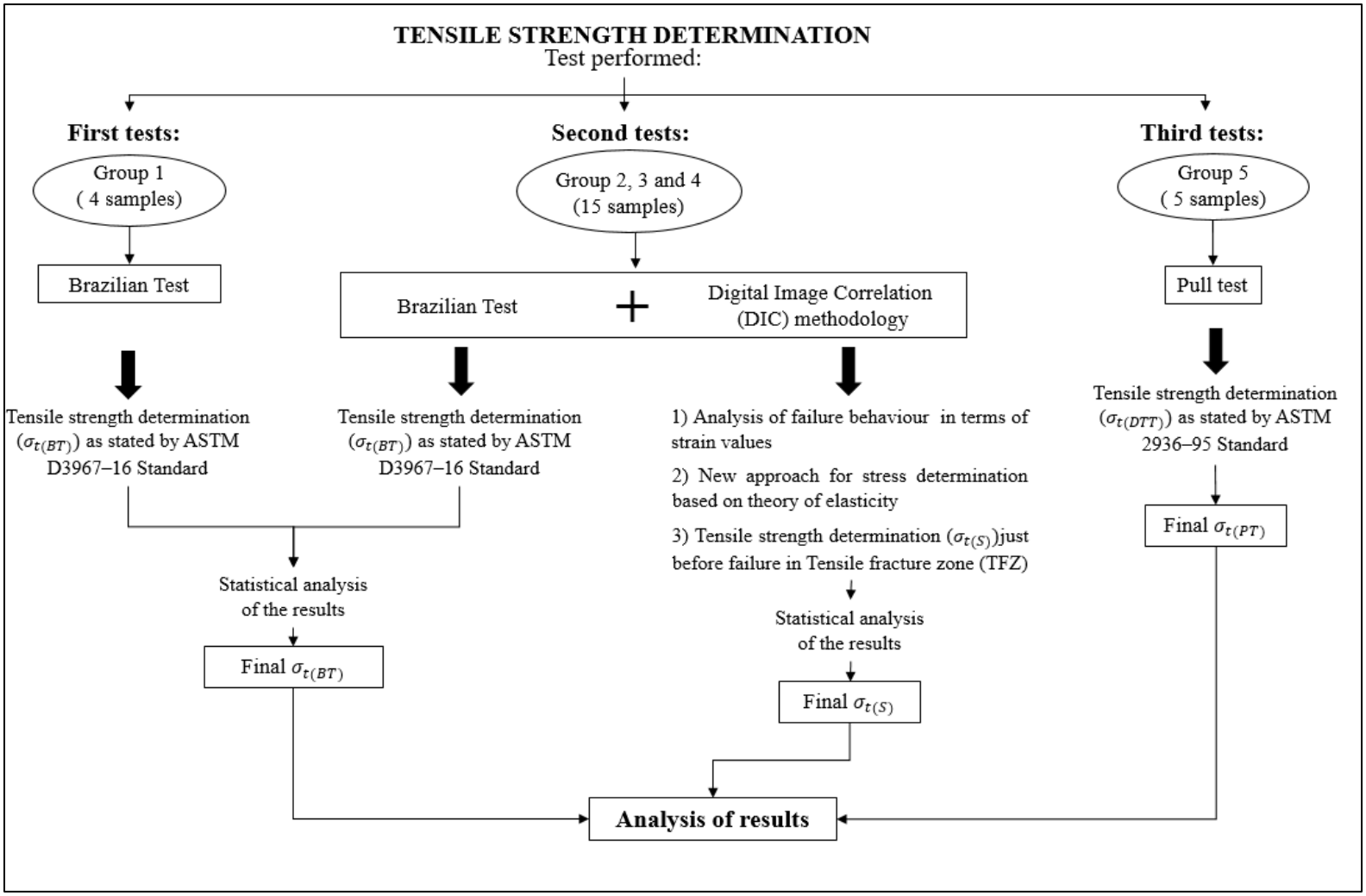

Figure 5.1 Graphical representation of the methodology followed for tensile strength determination

Brazilian tests were performed in the Surface Mining Research Laboratory facilities at the University of Alberta, using the same MTS machine and data acquisition system previously introduced in Chapter 3.4.

5.1 Initial Brazilian test procedure

The initial tests were performed following the ASTM D3967–16 (2016b) standard test method for Splitting Tensile Strength of Intact Rock Core Specimen.

5.1.1 Experimental set up and results

Core samples were taken from blocks of rock gathered at the mine and cut into small discs with an average thickness to diameter ratio of 0.5. In total, 4 samples were tested (Group 1) using flat platens and a constant test rate of 0.15 mm/min. On average every test lasted 6.12 min and the applied force and axial displacement were recorded. Figure 5.2 shows the broken samples.

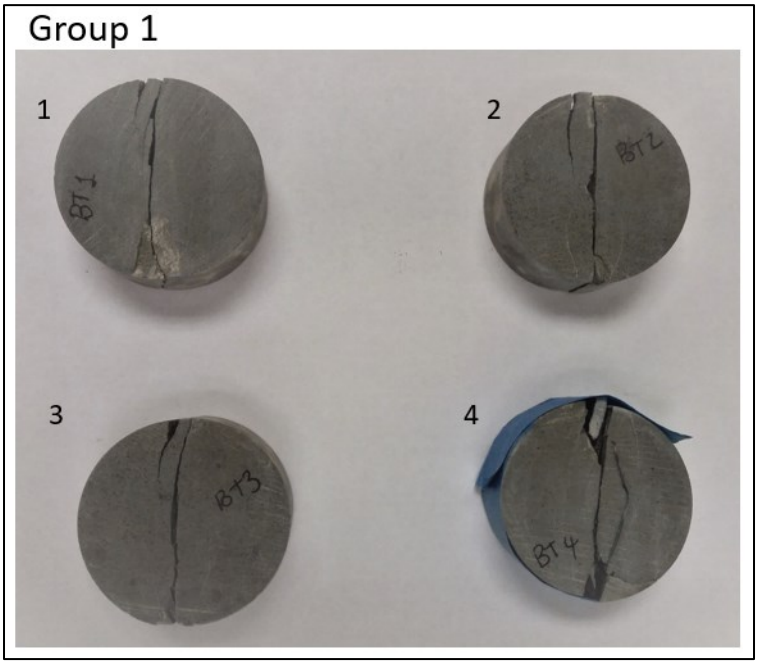

Figure 5.2 Broken samples in Group 1 after the Brazilian test

For tensile strength determination, equation 5.1 as suggested by ASTM D3967–16 (2016b) was utilized assuming crack initiation occurred at the center of the sample where, theoretically, the maximum tensile stress is reached.

$$\sigma_{t(BT)} = \frac{2P}{\pi Dt} \quad 5.1$$

Where $\sigma_{t(BT)}$is the tensile strength of the rock in MPa, P is the applied load at failure (N), D and t are the diameter (mm) and thickness (mm) of the samples respectively. Table 5.1 indicates the sample dimensions and the calculated $\sigma_{T(BT)}$.

Table 5.1 Tensile strength ($\sigma_{T(BT)}$) of rocks in Group 1

Sample #	**Thickness t (mm)**	**Diameter D (mm)**	$\boldsymbol{\sigma_{t(BT)}}$**(MPa)**
1	25.43	49.66	6.80
2	31.71	49.34	7.84
3	24.90	50.04	10.25
4	25.27	49.92	6.55
Average	26.83	49.74	7.86

The average $\sigma_{T(BT)}$ obtained was 7.86 MPa with a standard deviation (SD) of 1.69. It is noted that sample 3 presented the highest $\sigma_{T(BT)}$value recorded. However, by observation, there was no obvious visual difference between this and the rest of the samples. The discrepancy might occur due to the intrinsic small heterogeneities of the rock, so it was not discarded.

Equation 5.1 assumes that the crack initiates at the center of the sample where the maximum tensile stress is reached. However, during the test, the fracture starting point was impossible to observe but two clear failure zones were identified: A Crushing Zone (CZ) at the loading contact points, and a vertical tensile crack along the sample diameter as illustrated in the Figure below.

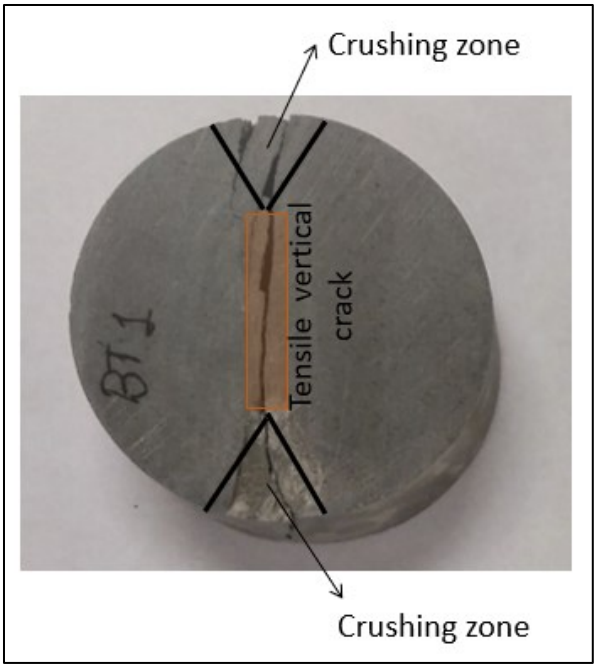

Figure 5.3 Crushing Zone and a vertical tensile crack observed in Brazilian Test

5.2 Application of Digital Image Correlation Technique (DIC) to tensile strength determination

From BT, the failure displayed a CZ and a tensile vertical crack. However, it was not possible to confirm that the center of the samples experienced the highest tensile stress value at crack initiation. In order to confirm and explore this in a more scientific manner, a Digital Image Correlation Technique (DIC) was utilized.

DIC was first introduced in the 1980's by Sutton, Wolters, Peters, Ranson, and McNeill, (1983); and Sutton, Mingqi, Peters, Chao, and McNeill, (1986). Since then, it has been utilized in many science and engineering applications. Authors like Tariq, Siddiqui, Naz, Ahmed, and Hussain, (2012); Lorenzino, Beretta, and Navarro, (2014); and L. Wang et al. (2018) used the technique to characterize crack initiation and propagation; Yi-Qiu, Lei, Meng, and Li-Yan, (2012); and Bilotta, Ceroni, Lignola, and Prota, (2017) assessed the mechanical behaviour of different materials and Sztefek et al., (2010); Tiossi et al., (2012); and Karimi, Shojaei, and Razaghi, (2017) made great contributions to understanding the mechanical behaviour of bones and arteries in the human body.

According to Correlated Solutions (2018); image analysis methods, via DIC techniques are able to track movement of groups of pixels called subsets (a user defined parameter), along a continuous

surface on a sample marked with a speckled pattern. For the subset tracking process, the system identifies the same subset in each photograph by comparing grey levels at each pixel inside the subset, that then relates their relative positions between the reference image (usually before load application) and each subsequent image taken while the object is loaded. Once the subset recognition is done, the displacement and deformation vectors are calculated (Correlated Solutions, 2018) and assigned to a unique point within the subset.

The continuous surface is analyzed as a mesh of subsets separated, as a function of distance called "step size" which is a user defined parameter that should be ¼ of the subset size (Simonsen, 2016). As stated by Correlated Solutions (2016), each point is considered independently and generates a local mesh of triangles, each one with a defined strain tensor which is then interpolated and smoothed to get the strain value for every existing data point on the sample.

The DIC system is composed of one (2D system) or two cameras (3D system), data acquisition hardware, grids or calibration targets and the analysis software. Since the main application of the DIC technique is to calculate displacement and strain, it has been extensively compared with strain gauges or extensometers measurements. According to Wei, Karuppanan, and Latif, (2013); Patel and Martin, (2018); and Kavdir and Aydin, (2019), there is no doubt that DIC measurements are in a good agreement with all more established strain measurement approaches, and in addition, it has the additional benefit of giving full-field strain data for every point in the area of analysis.

5.2.1 Experimental set up

The MTS machine and flat platens were the same as previously introduced. In addition, two cameras, one LED flood light and a data acquisition system connected with DIC software were installed. The final configuration is presented in Figure 5.4.

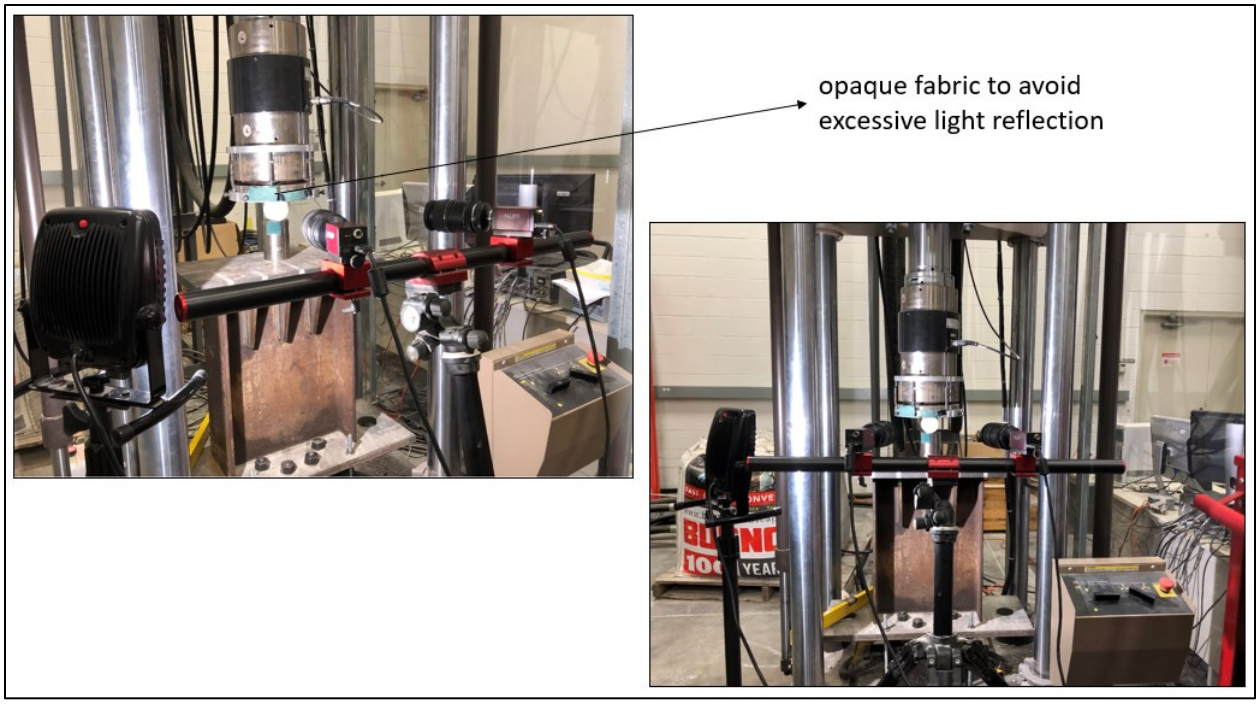

Figure 5.4 Experimental set up for Brazilian Test and DIC methodology

The cameras used were 4 MP resolution (2048 x 2048 pixels) Nikon units with a fixed focal length (f) of 90mm. The distance between the cameras and the cameras and the specimen was designed to optimize the overlap between the images, so that the field of view of both cameras completely covered the area of interest. To accomplish this, the cameras were installed symmetrically in front of the sample, as shown in Figure 5.5. Once the cameras were positioned, they were focused carefully on the surface 'painted' speckles. Best practice was followed to zoom in to a particular area on the specimen and focus the cameras at this point.

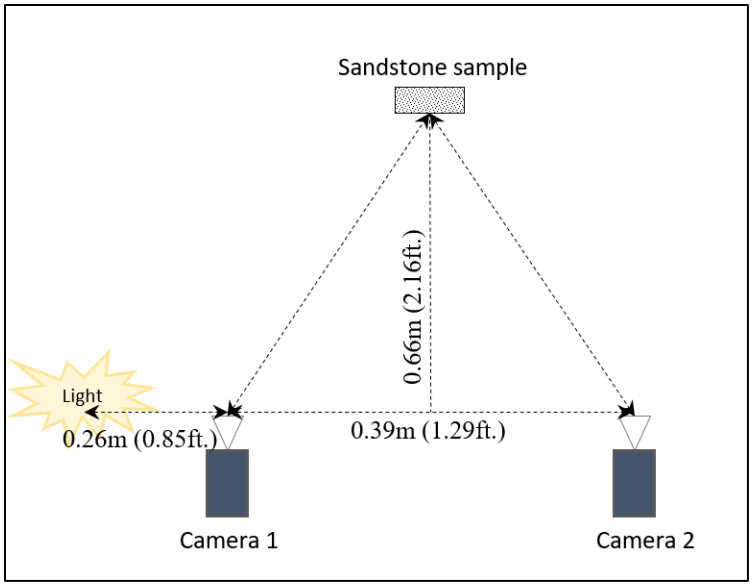

Figure 5.5 Distances set for Brazilian Test and DIC approach

In order to allow enough light into the camera, a large aperture (low f number) was necessary. However, this resulted in a very small depth of field (DOF), which in turn, made the speckles on the images unfocused in some areas. Therefore, improvement was introduced using a LED flood light, so it was possible to obtain suitably bright images with small values of aperture and workable DOF. It should be noted that an LED light was selected to avoid any wave interference that could cause noise in the measurements. Initially the light was located behind and in the middle of the cameras, but this caused excessive light reflection which in turn interfered with the strain measurements. To avoid this, the light was located next to one camera (one corner of the set up configuration) and some opaque fabric was attached to the metallic platens in the MTS machine as shown in figure 5.4.

After positioning the LED light, the aperture and exposure time were adjusted. Aperture is defined as the opening in the lens that governs the amount of light that enters the camera. It is usually designated with a f-number. The larger the number the less light passes through the lenses, and vice versa. An aperture value of f11 was used and an LED light was positioned so as to allow the correct combination of focus, aperture and exposure time. The exposure time or shutter speed, which controls the time that the cameras shutters remain open between shots, was adjusted at the beginning and during the test as suggested by Correlated Solutions (2007). For all the samples, values of 22 to 19 ms were used to get suitable images.

5.2.2 Specimen preparation

Initially all the core samples were cut by using a cut-off diamond blade saw and following the specifications suggested by the ASTM D3967–16 (2016b) standard. In total 15 samples with an average thickness to diameter ratio of 0.33 were tested and divided into 3 groups as shown in the table 5.2.

9 samples were obtained from one block of rock. Of these 4 were smaller (Group 2 in Table 5.2) and 5 were larger (Group 3 in Table 5.2). In addition, 6 samples from another block of rock, were analyzed, all of similar size (Group 4 in Table 5.2).

Table 5.2 Samples dimensions for DIC application on Brazilian Test

	Sample #	Thickness t (mm)	Diameter D (mm)
Group 2	1	15.65	50.69
	2	16.79	50.50
	3	16.34	50.55
	4	13.87	50.63
	Average	**15.66**	**50.59**
Group 3	1	26.30	82.02
	2	26.97	82.46
	3	25.91	81.92
	4	26.49	82.49
	5	27.11	82.49
	Average	**26.56**	**82.27**
Group 4	1	17.69	50.47
	2	16.95	50.82
	3	16.29	50.58
	4	18.17	50.58
	5	16.81	50.52
	6	16.52	50.98
	Average	**17.08**	**50.66**

An appropriate subset recognition is only possible if the pattern is random and highly contrasted. To avoid unwanted reflection or over brightness, the “speckling” paint must be flat (ie not glossy). In addition, The speckle or contrasting pattern as stated by Correlated Solutions (2018) can be drawn using spray paints, ink, stencils, printing, etc. During the development of this thesis, a fine

felt tipped pen and a brush were used to draw the speckles. Initially, one face of the sample was sanded with extra fine 220 and 320 grit sandpapers to ensure their smoothness. The sanded surfaces were cleaned using a brush and solvent wipes. After 12 hours at room temperature (to ensure the samples were completely dried), the cleaned surfaces were covered with a flat white paint shown in Figure 5.6. Even though the paint was “fast dry”, 12 hours was allowed before the speckles were drawn.

Figure 5.6 Flat white paint used for sample preparation

The pen used was a retractable black ultra fine point marker (a “sharpie”) as shown in Figure 5.7. Even though this technique worked well, it was time consuming, which was not convenient when preparing many samples.

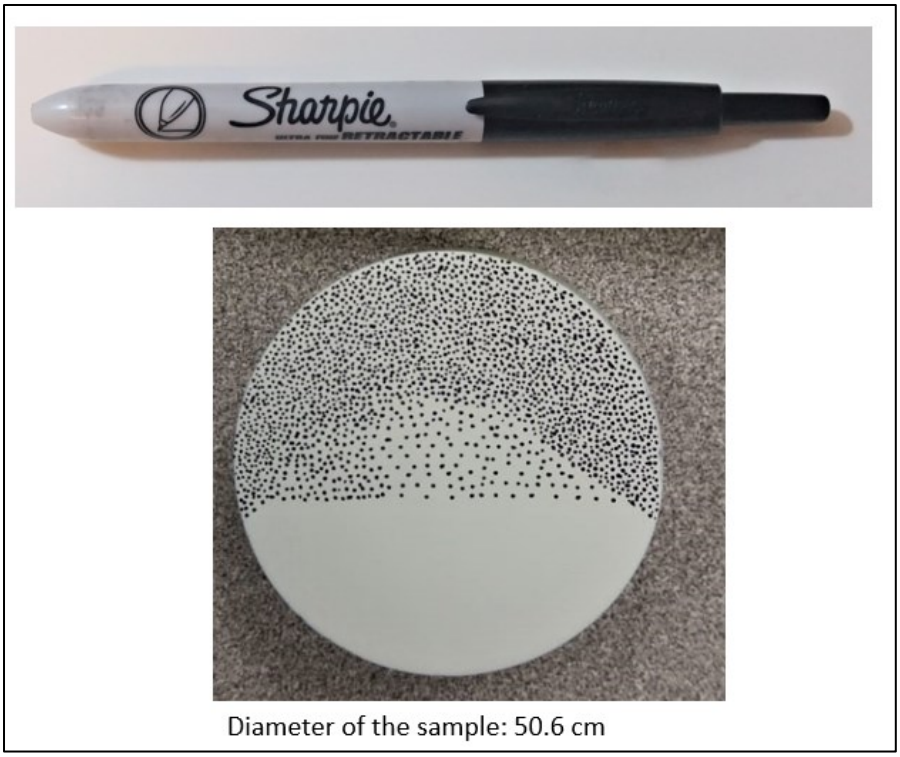

Figure 5.7 Retractable black ultra fine point marker used for sample preparation

Creating speckles using the brush technique involves charging the brush with black paint and strumming the bristles to produce a spray of paint, Figure 5.8. This technique produced much faster results but required practice to achieve consistency. The main issue was that without care overlarge speckles were generated which fell outside the required subset size range.

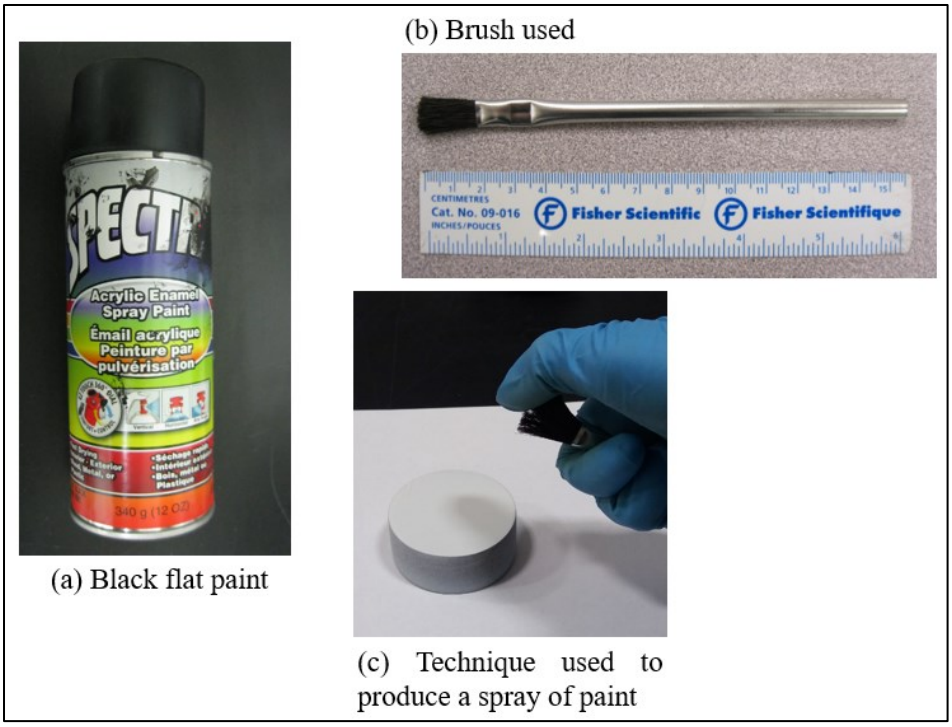

Figure 5.8 Tools used with the brush technique

Preparing one 50mm average diameter sample using the felt tip pen took about 40 min but only about 5 min with the brush. In total 5 samples were prepared using the pen method and 10 with the brush. Figure 5.9 shows an example of each method.

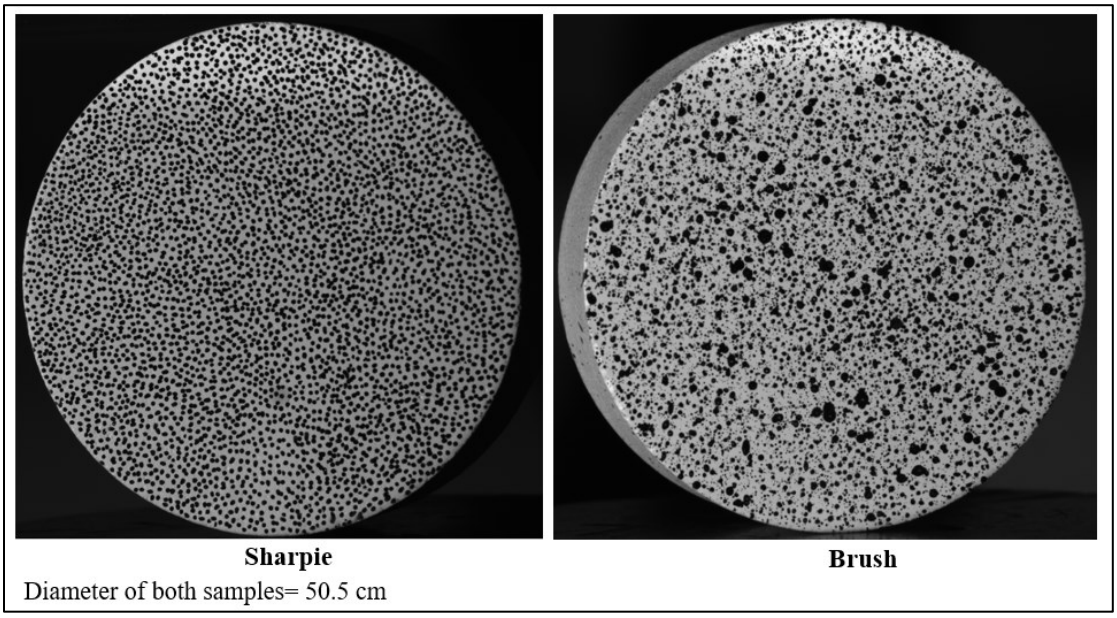

Figure 5.9 Speckle pattern drawn using an ultra fine point marker (left) and a brush (right)

5.2.3 Running the test and analysis of results

The test rate for the BT was set as 0.15 mm/min and the mean time to failure for all the samples tested lay between 3 and 5 min. Figure 5.10 shows the broken samples in each group and Table 5.3, the $\sigma_{T(BT)}$ of the samples.

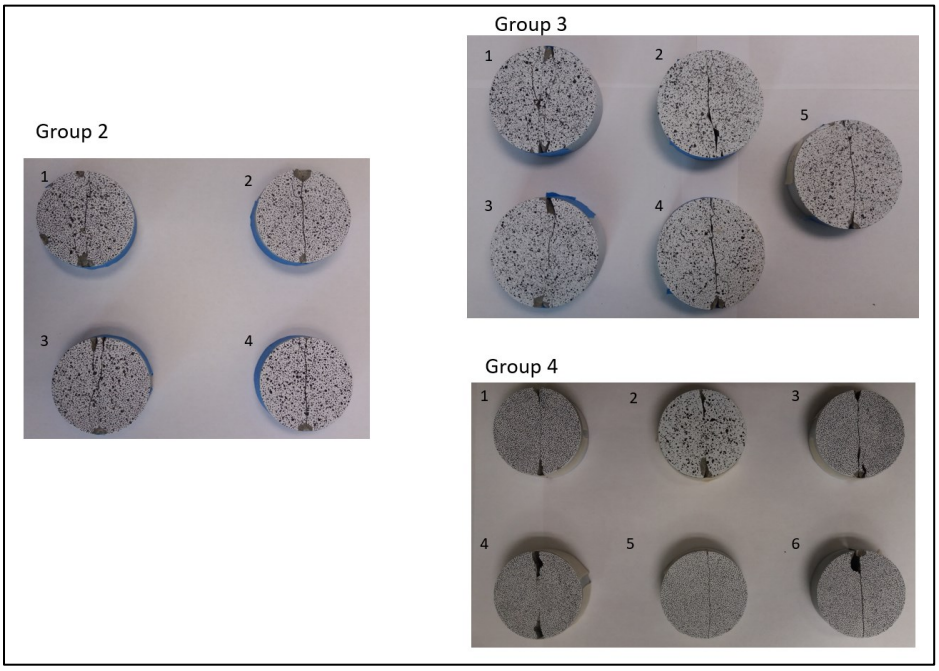

Figure 5.10 Broken samples using Brazilian Test and DIC methodology

Table 5.3 $\sigma_{T(BT)}$ values for Group 2, 3 and 4

	$\sigma_{T(BT)}$ (MPa)		
	Group 2	**Group 3**	**Group 4**
Sample 1	8.56	10.20	11.01
Sample 2	6.01	7.71	7.23
Sample 3	10.38	10.12	11.25
Sample 4	7.68	10.68	5.65
Sample 5		11.13	7.74
Sample 6			7.95
Average	**8.16**	**9.97**	**8.47**

Comparing the results above (Table 5.3) with those obtained during the first BT attempt (Table 5.1), the results appeared similar. However, to verify this initial observation, the data was statistically analyzed.

A statistical technique called Analysis of Variance (ANOVA), was used to compare the mean values of $\sigma_{T(BT)}$ for groups 1, 2, 3 and 4. However, since ANOVA requires a normally distributed sample population, a normality test (Shapiro-Wilk test) with an alpha level of 0.05 was first performed. The results shown in Table 5.4 evidence that the data in each group were normally distributed, and therefore the ANOVA analysis was used.

Table 5.4 Normality test results of $\sigma_{T(BT)}$ for Group 1, 2, 3, and 4

	Number of Sample	**P-value**	**Decision**
Group 1	4	0.273	Can't reject normality
Group 2	4	0.993	Can't reject normality
Group 3	5	0.125	Can't reject normality
Group 4	6	0.345	Can't reject normality

To perform the ANOVA, a significance level of 0.05 was selected, the null hypothesis (H_0) stated that there was no significant difference among the means of the groups whereas the alternative hypothesis (H_A) stated that at least one of the means was significant different. The results are shown in Table 5.5:

Table 5.5 ANOVA test to compare the means of $\sigma_{T(BT)}$ for Group 1, 2, 3, and 4

	DF	**Sum of Squares**	**Mean Square**	**F value**	**P value**
Between Groups	3	12.313	4.104	1.233	0.332
Within Groups	15	49.919	3.328		
Total	18	62.232			

Since the P-value was greater than 0.05, H_0 was accepted. In other words, even though the samples tested were taken from different block of rocks, the results can be treated as significantly similar since they are part of the same population or type of rock. Also, it should be noted that the variations in sample dimensions between the groups did not affect the resulting $\sigma_{T(BT)}$. Taking all the samples for group 1,2,3 and 4, the average $\sigma_{T(BT)}$ was estimated as follow:

$$\sigma_{t(BT)} = (8.67 \pm 1.86)\text{MPa} \quad 5.2$$

The above tests were also monitored using the DIC system. However, it should be noted that sample 5 of group 4 was not recorded due to an experimental error, and was hence not included in the following results. For DIC analysis, the system was programmed to capture 2 images per second (its maximum rate frame). The equipment was calibrated before each group was tested, as recommended by Correlated Solutions (2007) using a 12 x 9 mm grid and taking 20 reference images.

The correlation process was performed using VIC-3D with a subset size of 40 and step size of 10. The program gave full-field strain values on the surface in every image taken throughout the test. In all the tests, at the early stage (usually for loads less than 12% of the peak load), the values calculated showed only random behaviour, possibly caused by small displacements between the sample and the loading platens (also stated by Belrhiti et al. (2017)). After this erratic stage, the values clearly started to show one of two "typical" behaviours as explained below (Type a or Type b):

a) ***Type a***: 57% of the samples displayed this type of behaviour. Here, from the start of the test, a distinctive area of high strain in all directions, (horizontal (ε_x), vertical (ε_y) and shear (ε_{xy})), was evident in the area where the load was applied, the "Crushing Zone". Also, the level of strain increased with increasing load.

   Another feature was that the highest values of ε_x and the smallest values of ε_y were found to occur along the vertical plane connecting the loading points. The positive ε_x values found here, created a characteristic tensile zone, as predicted by the theory behind the BT. However contrary to the theory, the highest values were not at the center of the sample but at the top and bottom edges in the crushing zone. The same plane also experienced vertical compressive strains ($-\varepsilon_y$) and once again these peaked in the crushing zone. The values of shear, ε_{xy}, in the same plane were close to zero. Figure 5.11 (a) shows the force vs axial displacement curve recorded during the BT for sample 3 in group 3. It can be observed that the sandstone presents a typical brittle fracture. Figure 5.11 (b) shows the sequence of strain values observed at different times during the test.

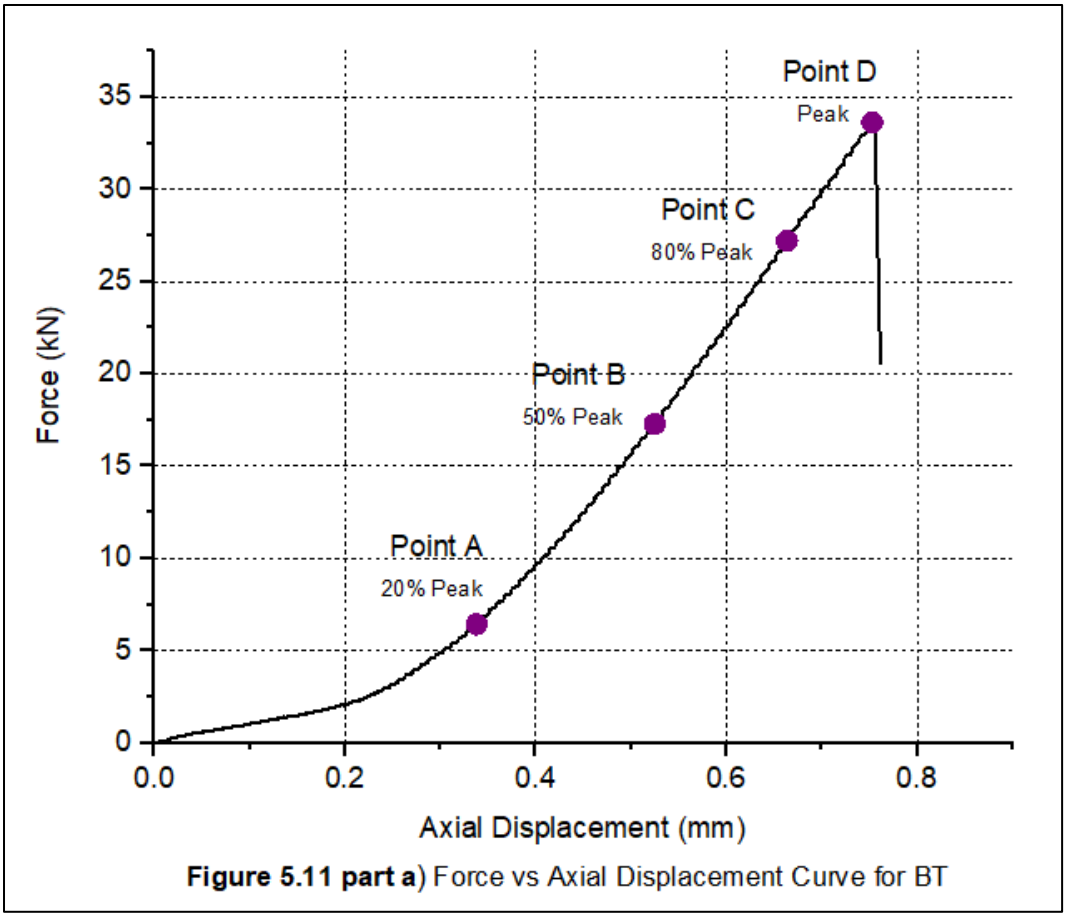

Figure 5.11 part a) Force vs Axial Displacement Curve for BT

Figure 5.11 Sequence of strain values during BT for Type a fracture behavior. (a) Force vs Axial displacement curve. (b) Strain values calculated from DIC

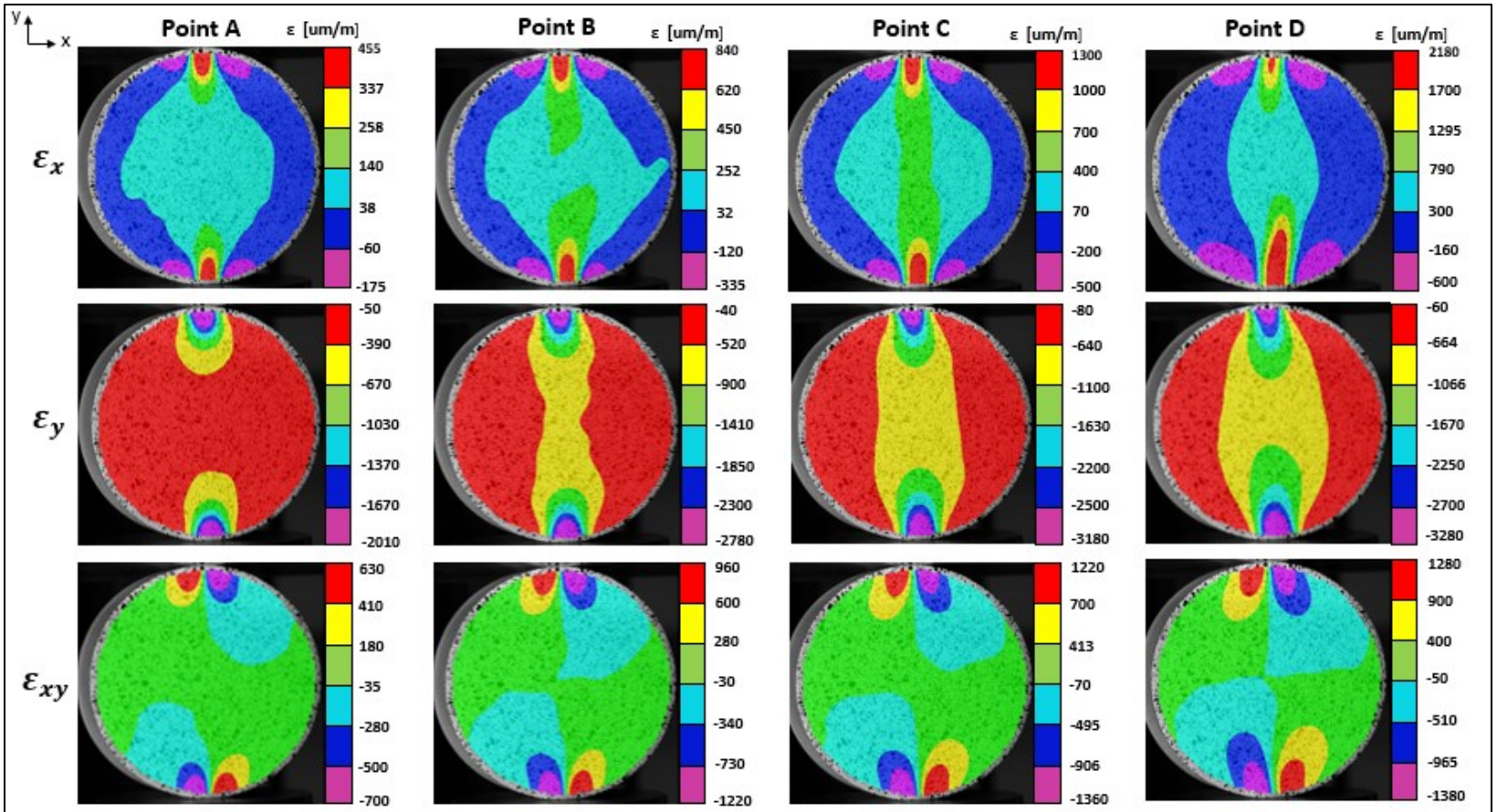

Figure 5.11 part b) Full-field strain values obtained at different moments during the BT. Point A is at 20% of the peak load, Point B at 50%, Point C at 80% and Point D just before the peak value. Each point is characterized with 3 graphs. The first one shows the strain values reached in horizontal direction (ε_x). The second picture shows the strain values reached in vertical direction (ε_y) and the last one shows the shear strain values (ε_{xy}). Positive strain values are interpreted as Tension. Note that every image has a different scale where red is always the highest value and magenta the less.

a) ***Type b:*** In this type of behaviour no Crushing Zone is evident at the start. Just after the erratic stage, the center of the sample was subjected to high values of tensile strain(ε_x), which then propagated in the vertical plane as predicted by the BT theory. However, at certain point, this propagation stopped, and the behaviour became very similar to that in Type a, the highest ε_x appearing at the top and bottom edges where a CZ appeared. Figure 5.12 (a) shows the force vs axial displacement curve recorded during the BT for sample 1 in group 4. Figure 5.12 (b) show the sequence of strain values observed at different time during the test.

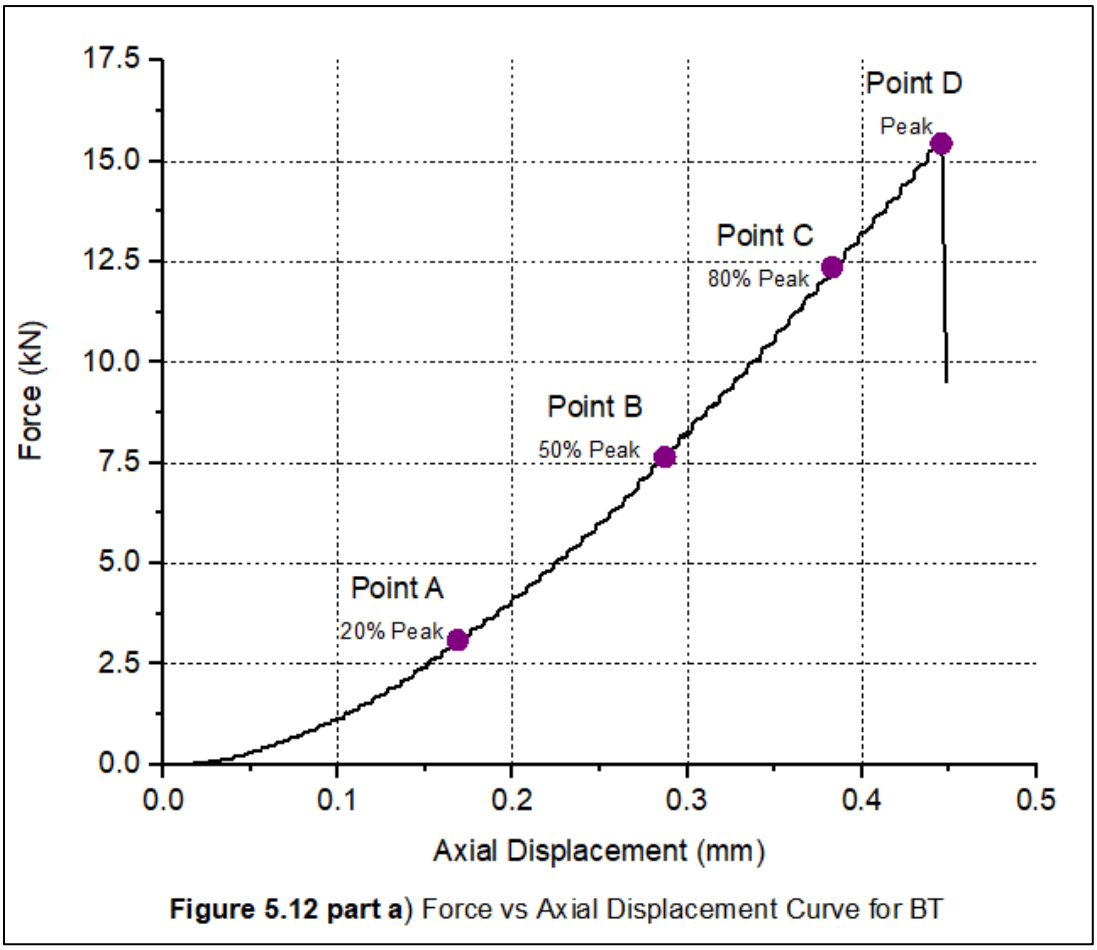

Figure 5.12 part a) Force vs Axial Displacement Curve for BT

Figure 5.12 Sequence of strain values during BT for Type b of fracture behavior. (a) Force vs Axial displacement curve. (b) Strain values calculated from DIC

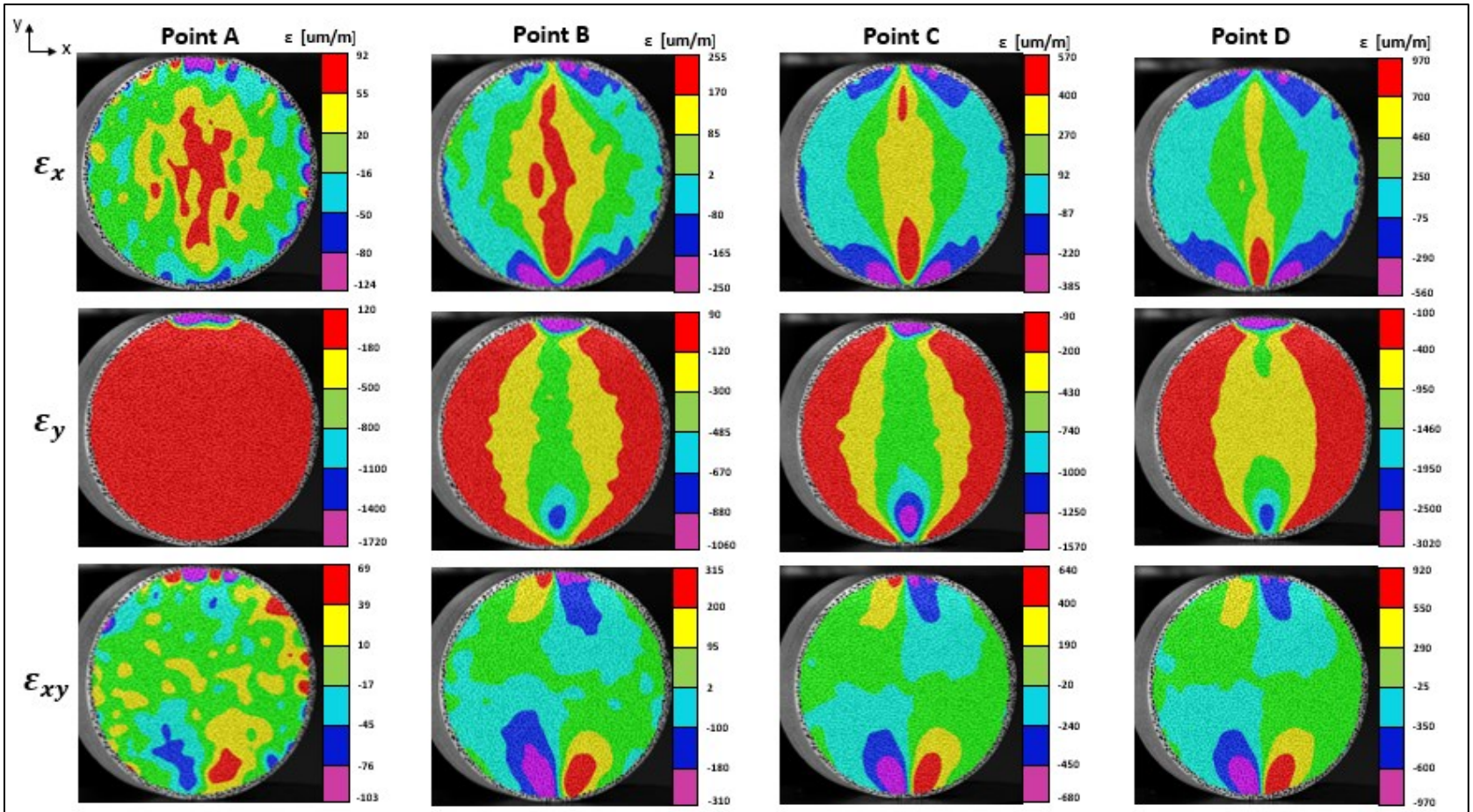

Figure 5.12 part b) Full-field strain values obtained at different moments during the BT. Point A is at 20% of the peak load, Point B at 50%, Point C at 80% and Point D just before the peak value. Each point is characterized with 3 graphs. The first one shows the strain values reached in horizontal direction (ε_x). The second picture shows the strain values reached in vertical direction (ε_y) and the last one shows the shear strain values (ε_{xy}). Positive strain values are interpreted as Tension. Note that every image has a

In Summary, it was clear in all the tests that two distinct areas of interest developed before failure: The Crushing Zone (CZ) and Tensile Fracture Zone (TFZ). The strain behaviour in the CZ was characterized by high values in all directions. It should be noted that in both Type a and Type b failure modes, the area of maximum horizontal strain (ε_x) did not necessarily appear at both crushing zones, sometimes just at one. On the other hand, along the TFZ, the values of ε_{xy} for all the samples were almost zero (-4.08x10^{-5}), ε_y equal to $-1.52\varepsilon_x$ for group 2, $-1.55\varepsilon_x$ for group 3 and $-1.79\varepsilon_x$ for group 4.

5.2.3.1 Stress determination from DIC methodology

Up to this point the conclusions have been drawn from strain values, but it would be more significant to know the full-field stress condition to which the rock was subjected along the vertical loading plane just before failure. This information could be used to analyze the TFZ created during rock breakage by blasting.

Assuming a homogeneous, isotropic and linear elastic rock, both the theory of elasticity and Hooke's law were used for stress determination in a plane stress condition from strain values measured by DIC approach. The following equations were used (Timoshenko and Goodier, 1951):

$$\sigma_x = \frac{E(\varepsilon_x + v\varepsilon_y)}{1 - v^2} \quad 5.3$$

$$\sigma_y = \frac{E(\varepsilon_y + v\varepsilon_x)}{1 - v^2} \quad 5.4$$

$$\tau_{xy} = \varepsilon_{xy} G \quad 5.5$$

Where σ_x is the horizontal stress (MPa), σ_y is the vertical stress (MPa), τ_{xy} is the shear stress (MPa), E is the Young's Modulus (MPa) and v the Poisson's ratio, G shear modulus (MPa).

The values of E, v and G where previously calculated in Chapter 3, Table 3.4.

The stress condition calculated just before failure along the vertical plane connecting the loading points is illustrated in Figure 5.13 for type a and 5.14 for type b failure modes.

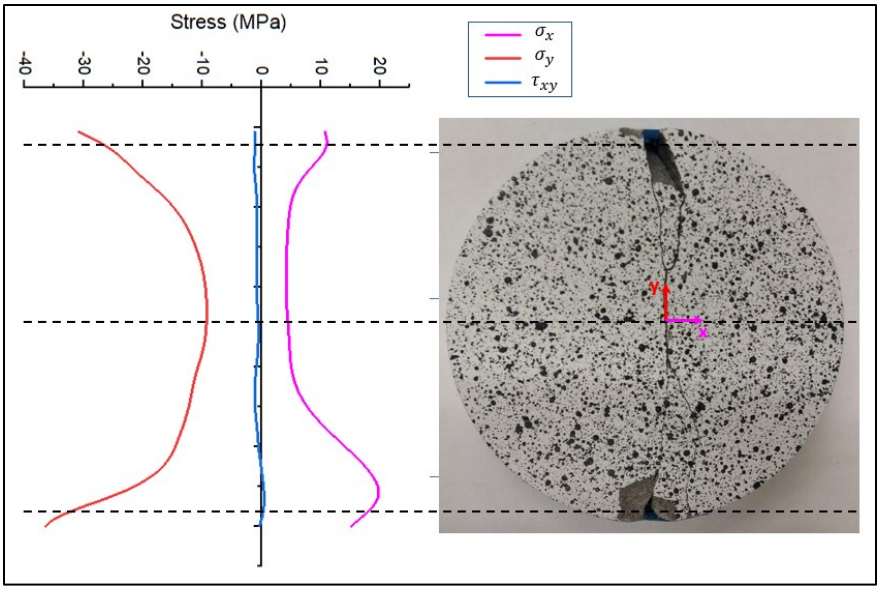

Figure 5.13 Stress distribution calculated along the vertical plane for Type a failure

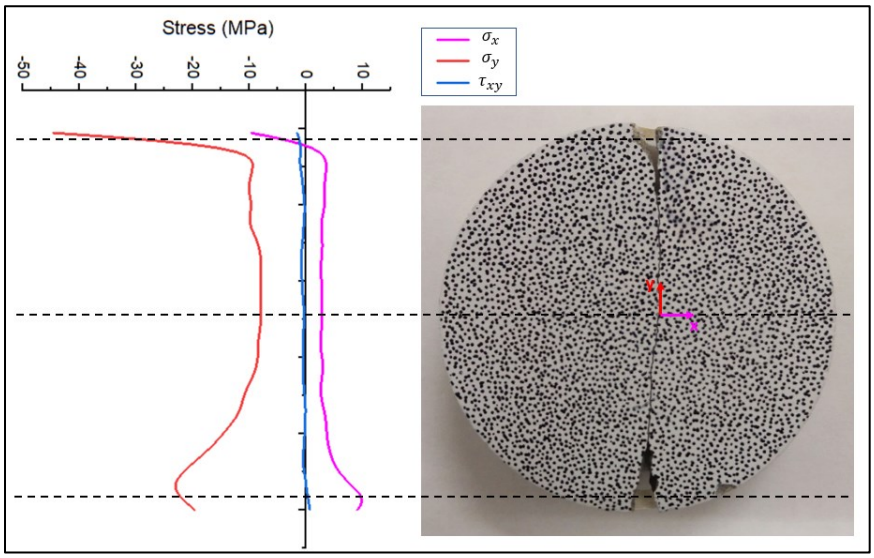

Figure 5.14 Stress distribution along vertical plane for Type b failure

For both failure modes, along the vertical plane, τ_{xy} with and average value of 0.35 MPa for all the samples, did not present significant difference between the contact under the platen and at the center of the samples. However, considering σ_x and σ_y; peak values were reached near the loading contact areas and decreased towards the center to a defined point of stress reaction change where they experienced a steady state at which tensile failure cracks propagated (TFZ).

The CZ experienced multiple stresses but not a predominant or distinct stress pattern. On the contrary, in the TFZ, σ_y and σ_x displayed a clear relationship, numerically correlated by equations 5.6, 5.7, 5.8, and graphically shown in Figure 5.15.

$$\text{For Group 2: } \sigma_y = -2.20\sigma_x \pm 0.31 \quad 5.6$$

$$\text{For Group 3: } \sigma_y = -2.26\sigma_x \pm 0.21 \quad 5.7$$

$$\text{For Group 4: } \sigma_y = -2.57\sigma_x \pm 0.39 \quad 5.8$$

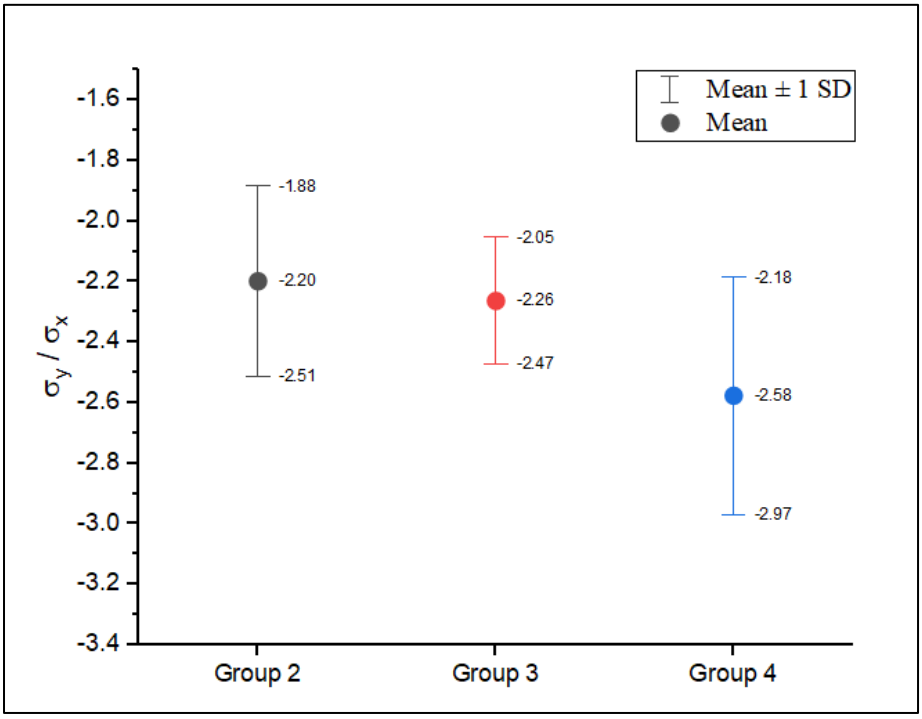

Figure 5.15 Ratio between σ_y and σ_x for each group

For σ_x the following Figure shows the mean values and SD obtained in each group (see Figure 5.16).

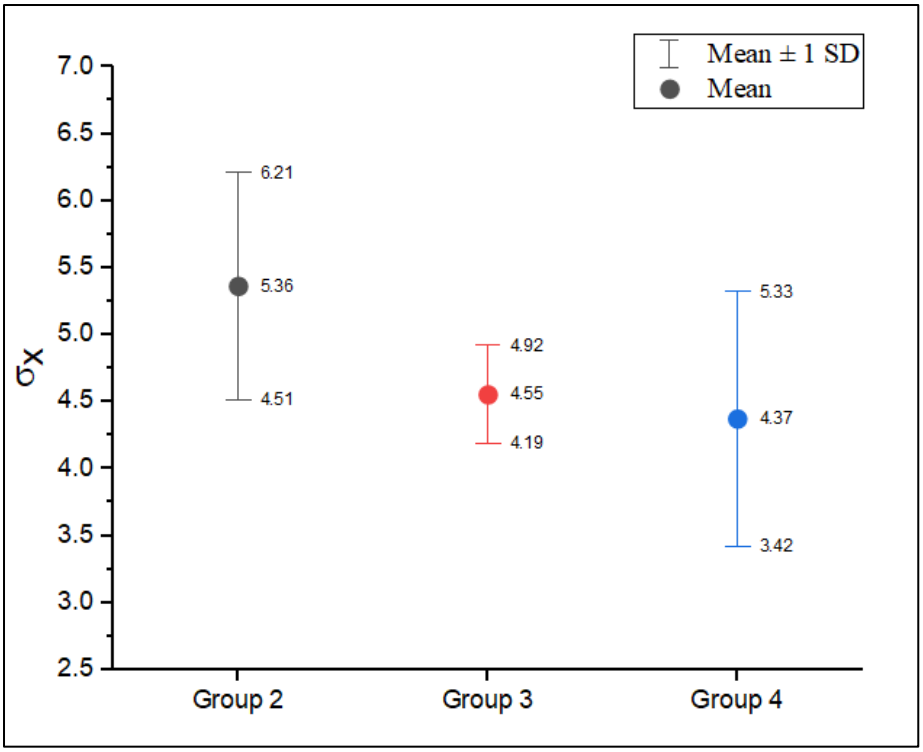

Figure 5.16 Average tensile strength in the Tensile Failure Zone per group

In order to confirm that Group 2 was not anomalous, normality and ANOVA test were conducted to verify the statistical similarity between the means. The results are summarized in Table 5.6 and 5.7 respectively.

Table 5.6 Normality test results of σ_x for Group 2, 3, and 4

	Number of Sample	**P-value**	**Decision**
Group 2	4	0.58028	Can't reject normality
Group 3	5	0.10917	Can't reject normality
Group 4	5	0.78647	Can't reject normality

Table 5.7 ANOVA test to compare the means of σ_x for Group 2, 3, and 4

	DF	**Sum of Squares**	**Mean Square**	**F value**	**P value**
Between Groups	2	2.394	1.197	2.079	0.171
Within Groups	11	6.335	0.579		
Total	13	8.729			

Again, all groups are random samples from the same population. In other words, the data seems to be part of the same type of rock. Also, an important feature concluded was that the dimension differences between the group samples were not statistically significant to change the stress concentration around the TFZ. Consequently, the groups were analyzed as a one single group.

As expected, the results followed a normal distribution as seen in Figure 5.17. The results indicated that the average value of σ_x just before failure in the TFZ was 4.72 MPa with a SD of ± 0.82.

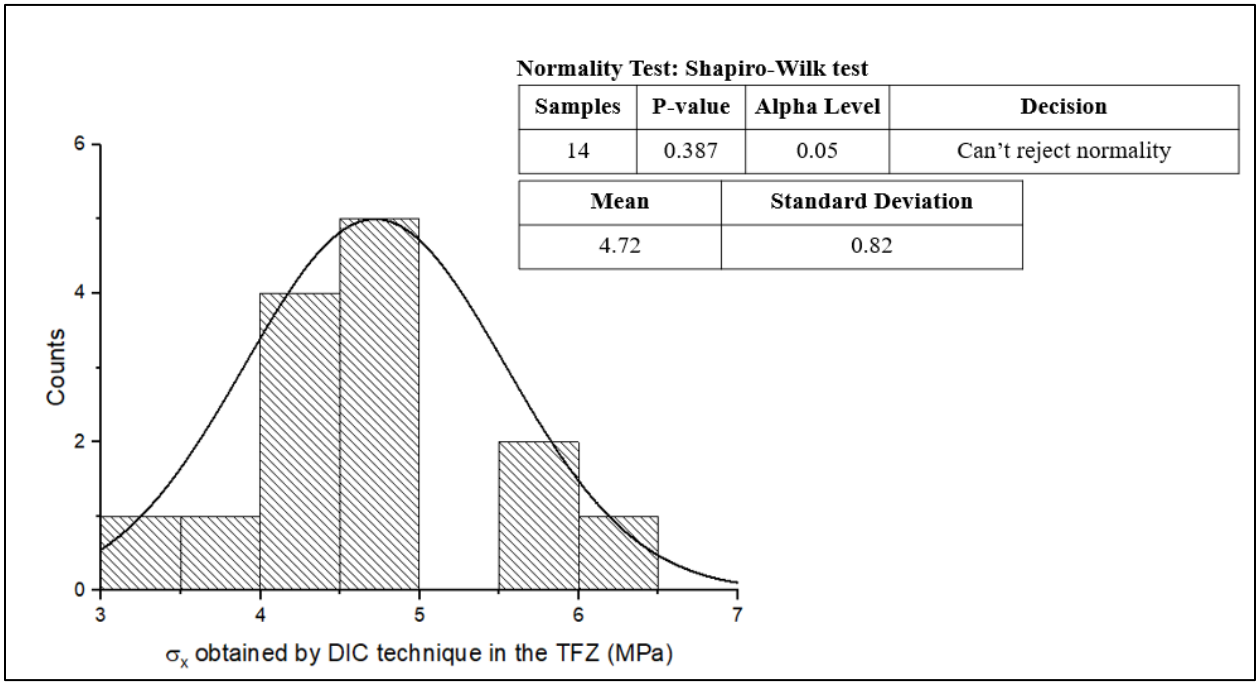

Figure 5.17 Histogram of σ_x for all the samples in Group 2,3 and 4

Sample 1 in group 4 presented the least value (3.11 MPa) and sample 1 in group 2 the highest, (6.3MPa). Neither sample showed any notable variations in their grain size or macro-structure, and the SD found in the distribution observed in Figure 5.17, was deemed acceptable.

From the fracture process perspective, the mean value of σ_x calculated in the TFZ just before failure, can be interpreted as the maximum tensile stress that needs to be exceeded in order for the rock to approach fracture by tension along the vertical loading plane. Therefore:

$$\sigma_x = \sigma_{t(S)} = (4.72 \pm 0.82)\text{MPa} \qquad 5.9$$

Where $\sigma_{t(S)}$ is the tensile strength of the material calculated from strain values in MPa.

Just prior to failure, the findings showed a completely different stress distribution to that predicted by BT theory as follows:

a) The maximum tensile stress did not appear at the center of the sample as predicted. On the contrary, the maximum stress concentration was found to be at the CZ, and therefore, it is assumed that the fracture starts inside this area and propagates towards the center of the sample. In order to determine the exact initial fracture point and propagation velocity, a much higher frame rate camera would be required.
b) The ratio between σ_y and σ_x is not -3 as implied by equation 2.17 and 2.18 (BT theory). Instead, the ratio, estimated by analyzing all the sample groups together can be expressed as:

$$\frac{\sigma_y}{\sigma_x} = (-2.36 \pm 0.34) \qquad 5.10$$

c) It is clear from the results in these tests, using flat platens, that ASTM D3967–16 (2016b) does not consistently apply.

5.3 Pull test approach

The Direct Tensile Test (DTT) or Direct Pull Test (DPT) is a standardized procedure where the rock specimen is subjected to direct tensile force until failure. The rationale behind conducting this test was to provide a comparator for the other two methodologies.

In total 5 samples were tested following the ASTM D2936-08 (2008) standard for Direct Tensile Strength of Intact Rock Core Specimens using a "Digital Tritest 50" testing machine with a maximum capacity of 50kN. The constant test rate in tension was set up at 0.4 mm/min and the mean time to failure was 10 min. The average length to diameter ratio for all the samples was 2.18.

The set-up configuration included two cylindrical caps of aluminium with a length of 33 mm and a diameter of 50.8 mm. The linkage system was designed to prevent any bending or flexural stresses along the specimen connected via four steel threaded eye bolts, 62 mm long and 12.7 mm in diameter; four grade 3 chains, each one with 3 links having a diameter of 6.3mm; four grade 5 bolts with a diameter of 6.3mm, eight washers and four nuts. The testing set up was designed as shown in Figure 5.18.

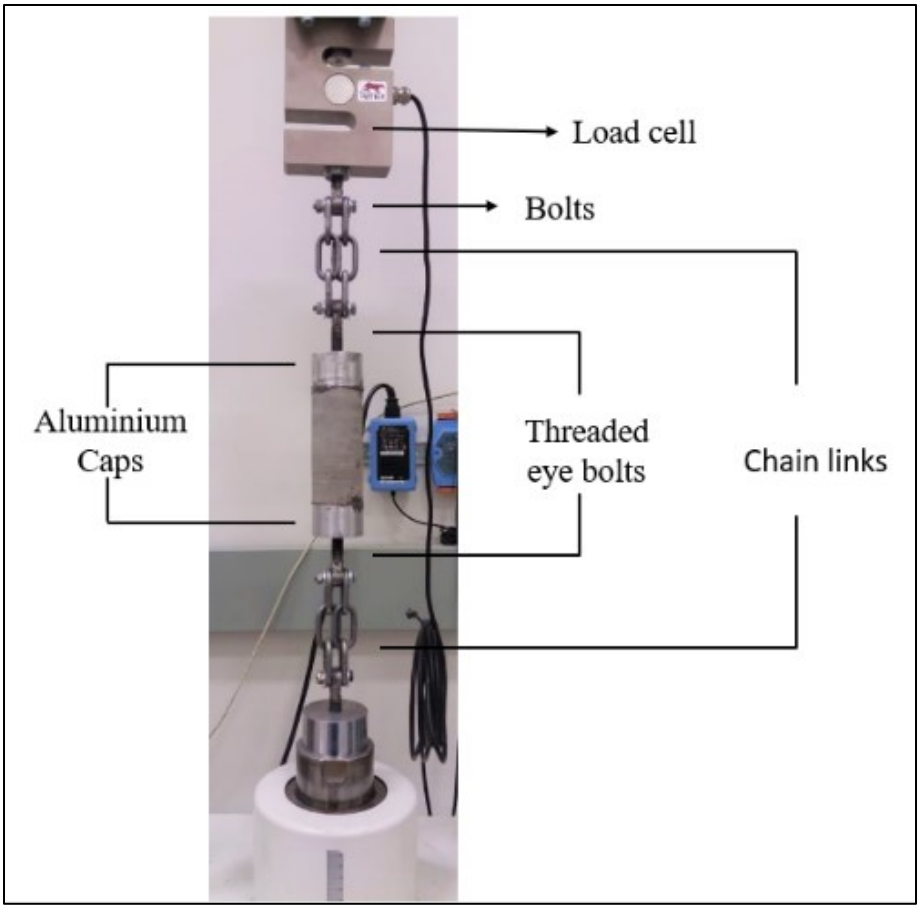

Figure 5.18 Testing set up for Pull test

The cylindrical end caps were glued to each end of the sample (which were cut, trimmed and ground flat and parallel to each other) using a crystalline, high tensile strength epoxy, brand name "Araldite" (Araldite, 2019). The samples remained at room temperature for at least 24 hours to set.

5.3.1 Results and discussion

The tensile strength was calculated using equation 5.11 as suggested by ASTM D2936-08 (2008).

$$\sigma_{t(PT)} = \frac{P}{A} \qquad 5.11$$

Where $\sigma_{t(PT)}$ is the tensile strength of the rock calculated in MPa, P is the maximum applied load in tension (N) and A is the cross-sectional area diameter (m^2).

Figure 5.19 presents the two failure mode observed, and Table 5.8 shows the sample dimensions, $\sigma_{t(PT)}$ and the fracture location. These samples are "Group 5".

Figure 5.19 The two characteristic crack locations in rock samples after Pull test

Table 5.8 Sample dimensions for Direct Pull Test

	Sample #	**Length (mm)**	**Diameter D (mm)**	**Tensile strength $\sigma_{t(PT)}$ (MPa)**	**Facture location**
Group 5	1	116.84	50.80	5.08	At the middle
	2	107.95	50.55	5.63	Top in rock
	3	114.30	50.55	5.45	Top in rock
	4	101.60	51.05	6.37	Top in rock
	5	111.00	50.00	5.37	Top in rock

In addition the Force vs Time curves recorded during the tests are presented in Figue 5.20.

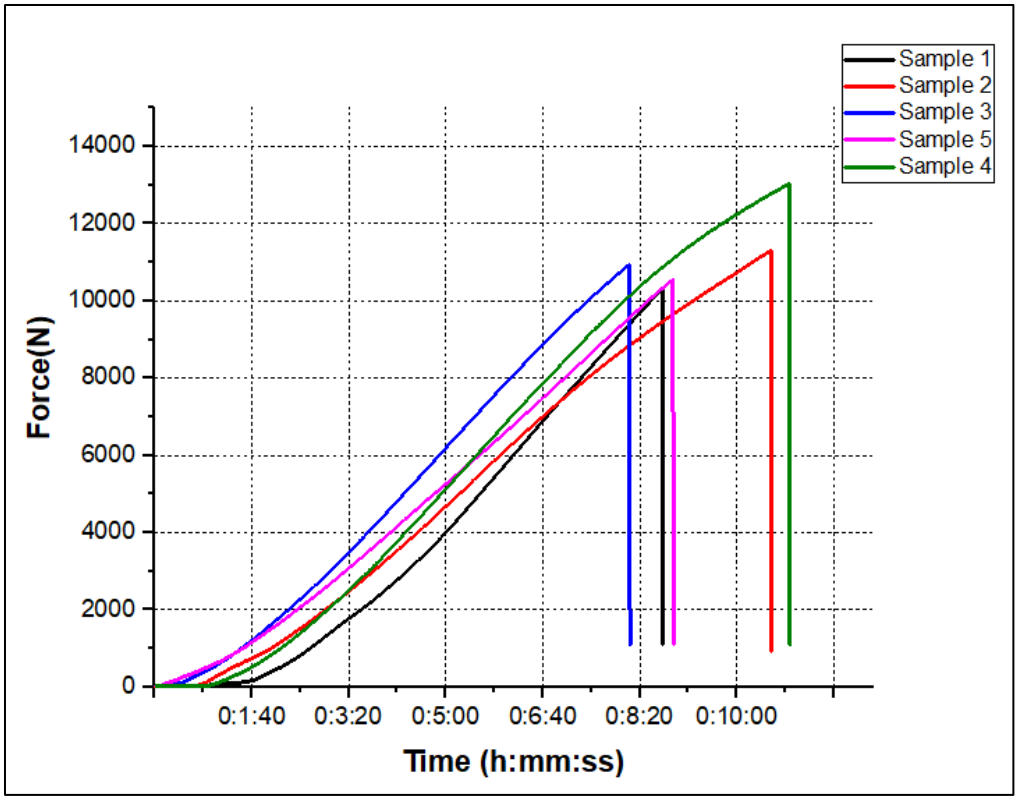

Figure 5.20 Resulting Force vs Time curves in pull tests

From Figure 5.20, it is observed that the tests fall into two groups which similar tensile values and testing time: Samples 1, 3 and 5 with smaller $\sigma_{t(PT)}$, and samples 2 & 4 with greater elapsed test time values. However, all the samples exhibited similar brittle failure behavior. An initial "settling zone" was encountered at the beginning due to the slack in the linkages being taken up. This was followed by a distinctive linear-elastic zone ending in a slightly curved area just before failure. In addition, all the samples presented the same slope of the linear elastic zone.

Equation 5.12 indicates the final $\sigma_{t(PT)}$ estimated using this approach.

$$\sigma_{t(PT)} = (5.58 \pm 0.48)\text{MPa} \qquad 5.12$$

The pull test is recognized in rocks mechanics as a methodology in which the actual tensile strength of the rock is obtained, but as found during these tests, there are many variables that make the test, in some cases, impractical. These include the specimen preparation, the linkage system and rock geological characteristics.

5.4 Comparing Tensile strength obtained by Brazilian test, DIC methodology and Pull test

Three methodologies have been used for tensile strength determination and the results are summarized in the following Table 5.9.

Table 5.9 Tensile strength values obtained by BT, DIC and PT

Experimental Technique	$\boldsymbol{\sigma_t}$ **(MPa)**
Brazilian test (BT)	$\sigma_{t(BT)} = (8.67 \pm 1.86)\text{MPa}$
Digital Image Correlation (DIC) and stress determination	$\sigma_{t(S)} = (4.72 \pm 0.82)\text{MPa}$
Pull test (DPT)	$\sigma_{t(PT)} = (5.58 \pm 0.48)\ \text{MPa}$

The pull test resulted in a lower value than the BT with a mean $\sigma_{t(BT)}$ to $\sigma_{t(PT)}$ ratio of 1.55. This ratio was very close to that obtained by (Patel, 2018) in a granite rock (1.35) and (Sarfarazi, Ghazvinian, Schubert, Nejati, and Hadei, 2016) in concrete (1.5). It is hence widely accepted that the BT overestimates the tensile strength value.

Comparing the mean values of $\sigma_{t(PT)}$ with $\sigma_{t(S)}$ and $\sigma_{t(BT)}$, differences of 0.86 and -3.09 MPa respectively were found. If the tensile strength given by the DPT were accepted as representative of the actual tensile strength of the sandstone as the ASTM standards stipulates, $\sigma_{t(S)}$ gave an accepted value of tensile strength.

It is interesting to note that the values obtained by the DPT suggested that the rock can support stresses in tension of up to 5.58MPa before failure, but according to DIC methodology, the tensile fracture zone reached values of only 4.72 (+/- 0.81) MPa before failure. The differences might be explained because insufficient information was gathered by DIC approach before failure. A higher speed camera might have recorded different strain values just before failure. According to the results observed, the stresses in x direction at the TFZ were uniform but were also incrementing as the load was increased, so there is a possibility that the final strain value just before failure were greater. Figure 5.21, shown the variation of the horizontal stresses of one point inside the TFZ at the middle of the one sample (sample 1 group 4) for all the pictures.

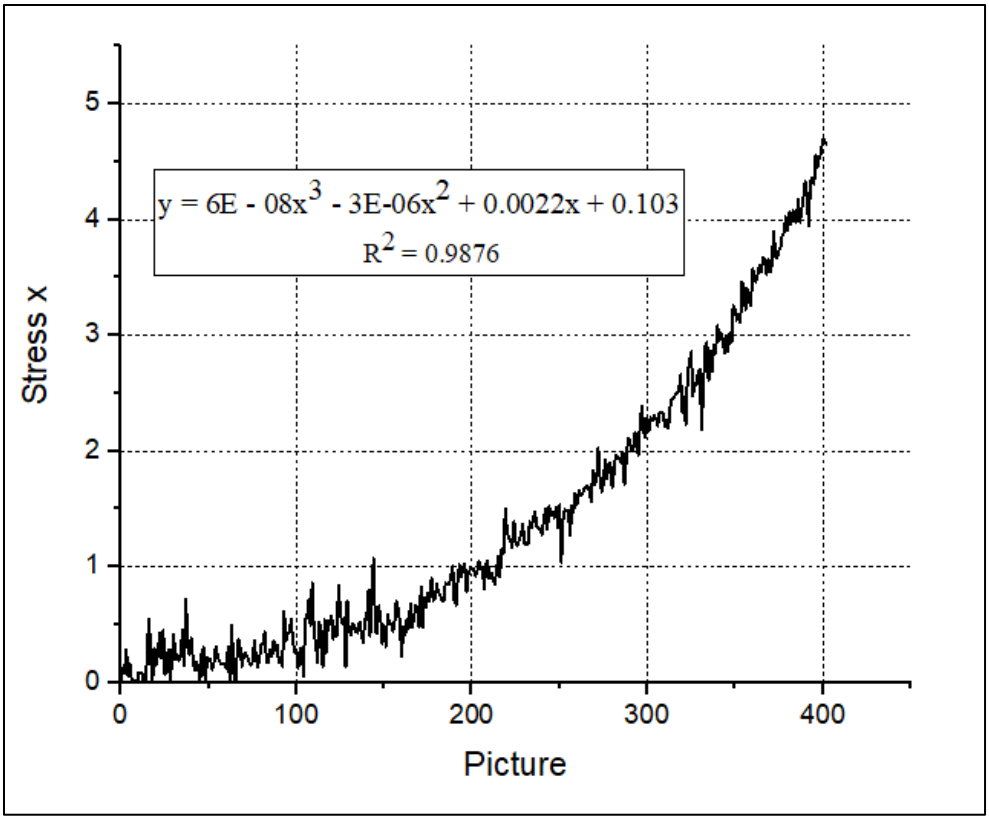

Figure 5.21 Typical variation of the horizontal stresses of one point inside the TFZ.

It should be noted that the variation of the horizontal stress per pictures taken follow a cubic equation, so extrapolating the values reached in the last picture on to a "next" picture basis, the tensile stress would never reach the results obtained by DPT. This is an interesting point that could be analyzed in future work.

6. FRAGMENTATION ENERGY IN ROCK BREAKAGE BY BLASTING

The energy required for rock fragmentation through blasting is derived from the explosive thermodynamics at detonation, then transmitted to the intact rock via shock waves and gas pressure to effect breakage. Ideally, all the energy would be conserved and focused to fragment the rock, or as may be deemed necessary for more efficient loading operations to move (or "heave") it to a piled format. However, the process is never 100% efficient; with noise, flyrock, loss through existing fractures and voids, vibration and heat as undesirable points of energy loss.

The concept of "energy partitioning", examining input and output energy distribution, is complex and comprises many variables that need to be understood in order to refine blast design strategy. A starting point is the determination of input energy derived from the explosive chemistry and an estimation of the efficiency of the blasting process. Once this has been established, one can consider more specific controllable factors in blast design, which can be altered and modified to effect an improved end result.

This chapter examines blast fragmentation and size distribution as a function of the pressure generated on detonation of an explosive; producing an instantaneous shock wave followed by gas products' expansion; to estimate the efficiency of the blasting process. For clarity, it is pertinent to mention that pressure, P is expressed in SI base units as Pascal (Pa), but it is also proportional to specific energy having units of Joules per cubic meter, also Pascal(J/m^3 or Pa). So, P may be expressed as energy per available unit volume of explosive, or energy per unit volume of rock blasted, to fragment a given volume of rock.

The final outcome of the interpretation and analysis, indicated through the work described below, is a practical measuring tool developed not only for efficiency determination but also as an easy-to–use means of evaluating and monitoring the effectiveness of the blasting process. All the calculations here are based on a single borehole, from which it is assumed that applicability could be extended and be representative for a larger field application to a blast pattern.

6.1 Explosive energy determination in terms of detonation and gas pressure

Energy determination of RIOFRAG^{TM} explosive, using the values reported by the manufacturer was previously introduced in chapter 3. The final energy value, expressed as the total energy released by the explosive through the detonation (Q), via thermodynamics' principles, was

calculated as 3.80 MJ/kg, or 4.74 GJ/hole, based on an average 1,247 kg of explosive used in one blast production hole. However, the objective of this research was to establish how much of that total energy was effectively converted into detonation and gas pressures.

According to ISEE (2011), the detonation pressure (P_{Det}) is defined as the high pressure reached at the commencement of the Reaction Zone resulting from the detonation process. It is widely accepted, used and calculated with the blasting industry as equation 6.1:

$$P_{Det} = \frac{\rho_e VOD^2}{4} \qquad 6.1$$

Where in this case, $\rho_e = 1{,}050\ kg/m^3$, the explosive density and VOD is the velocity of detonation (m/s) (see Chapter 3). Elliott and Wedgewood (2019) recorded VOD values with an average of 5,169.2 m/s at the Highvale mine. Substituting these values into equation 6.1, P_{Det} was estimated as 7,014.7 MPa.

P_{Det} is the initial high pressure shock front impacting the borehole wall. This effect expands the borehole by pushing the walls out, compressing and crushing the material and creating the majority of the "fines" in the resulting muckpile.

Gas pressure (P_{Gas}) is defined as the pressure exerted by the gases expanding into the rock fractures. It is also known as the Borehole pressure, and according to ISEE (2011), it is about 45 to 50 % the magnitude of P_{Det}. This estimation is however dependent wholly on the geologic nature of the rock mass being blasted, where huge variation would be generated through higher degrees of rock mass natural geologic fracture, through which such gas pressure could be lost.

Knowledge of the explosive chemical reaction is required to determine the P_{Gas}. Given the variability of fuel oil content in ANFO explosive preparation and the proprietary composition of RIOFRAG^{TM}, a widely accepted equation for ANFO was used as representative of the chemical reaction, equation 6.2. Note that the base diesel fuel molecule (CH_2) was utilized in this formulation.

$$\mathbf{3}NH_4NO_3 + \mathbf{1}CH_2 \rightarrow CO_2 + \mathbf{7}H_2O + \mathbf{3}N_2 \qquad 6.2$$

Since the molar mass (M_m) of Ammonium Nitrate (NH_4NO_3) and CH_2 are equal to 80.04 g and 14.03 g respectively, it was evident that 254.16 g of explosive were used in equation 6.2. In balancing the chemical equation, Table 6.1 and equation 6.3 were derived for 1,247 kg of explosive

Table 6.1 Moles of reactants and products in explosive chemical reaction for ANFO

		Moles	Explosive mass (g)	Relative weight (%)
Reactants	**NH_4NO_3**	14,719	1,178,179	94.5%
	CH_2	4,906	68,821	5.5%
Products	**CO_2**	4,906		
	H_2O	34,345		
	N_2	14,719		

$$\mathbf{14,719}NH_4NO_3 + \mathbf{4,906}CH_2 \rightarrow \mathbf{4,906}\,CO_2 + \mathbf{34,345}H_2O + \mathbf{14,719}N_2 \qquad 6.3$$

Once the equation was established, P_{Gas} was defined via the ideal gas equation, 6.4:

$$Pgas = \frac{nRT_e}{V} \qquad 6.4$$

Where:

- n is the number of moles of products and equal to 53,971 moles (see equation 6.3).
- R is a universal gas constant equal to $0.0821\ \frac{L\ atm}{mol\ K}$.
- V, equal to 1,187.6 L is the borehole volume filled with explosive. This was calculated as the area of a circle with a diameter equal to a borehole diameter (D_B) times the actual charge length(L). D_B and L were estimated in Chapter 3 and shown in Table 3.1 and equation 3.1 respectively.
- T_e is the temperature of the explosion in (K), expressed as the maximum temperature that the gaseous products reach in an adiabatic process (Akhavan, 2004). As the reaction proceeds, assuming no expansion or change in volume in the borehole, all of the energy liberated (Q) is used to heat the gasses resulting from the reaction, incrementing their temperature to T_e. The ultimate value of T_e depends on the specific heat capacity of the gaseous products.

According to Smith, Van Ness, and Abbott (2005), in a closed system of n moles of product, the energy balance can be express in terms of the mean molar heat capacity at constant volume (C_V) and the change in temperature (ΔT) as follows:

$$Q = n\Delta U = n\int_{T_1}^{T_2} C_v dT \qquad 6.5$$

However, since C_v is temperature dependant, an evaluation of equation 6.5 is compleed as empirical equations (Smith et al., 2005) in which some characterteristic constant of the products is needed. For the sake of practicality the methodology used in this research to determine T_e followed from Akhavan (2004), and applied by Britton, Skidmore, and Otuonye (1984). Knowing that T_2 is equal to T_e and the number of i^{th} product in the gas mixture, equation 6.5 may be written as equation 6.6 where T_e can be isolated as equation 6.7.

$$Q = \left(\sum n_i x C_{vi}\right) x(T_e - T_1) \qquad 6.6$$

$$T_e = \frac{Q}{\sum n_i x C_{vi}} - T_1 \qquad 6.7$$

Where C_{vi} is the mean molar heat capacity at constanct volume for each gaseous product in the product mixture at T_e.

To solve equation 6.7, the mean molar heat capacities of the gaseous products at different temperatures were required (see Table 6.2). The Q value, calculated as 4.74GJ/hole, T_1 was assumed as 293.15K (Standard Temperature), and n moles was as indicated in equation 6.3.

Using final temperatures estimates of 2,700 K and 2,800 K and applying equation 6.7, two different Q values were calculated as shown in Table 6.3.

Table 6.2 Average molar heat capacities at constant volume C_v (J $mol^{-1}K^{-1}$) for gaseous products at different temperatures after Akhavan, (2004).

Temperature (K)	CO_2	H_2O	N_2
2,700	47.51	37.48	25.70
2,800	47.74	37.85	25.82
2,900	47.97	38.20	25.93
3,000	48.17	38.53	26.03

Table 6.3 Q values calculated at different explosion temperatures

***Te* (K)**	**Q calculated (GJ/hole)**
2,700	4.57
2,800	4.80

From the Table above, the following graph was constructed as a linear relation to find the final T_e .

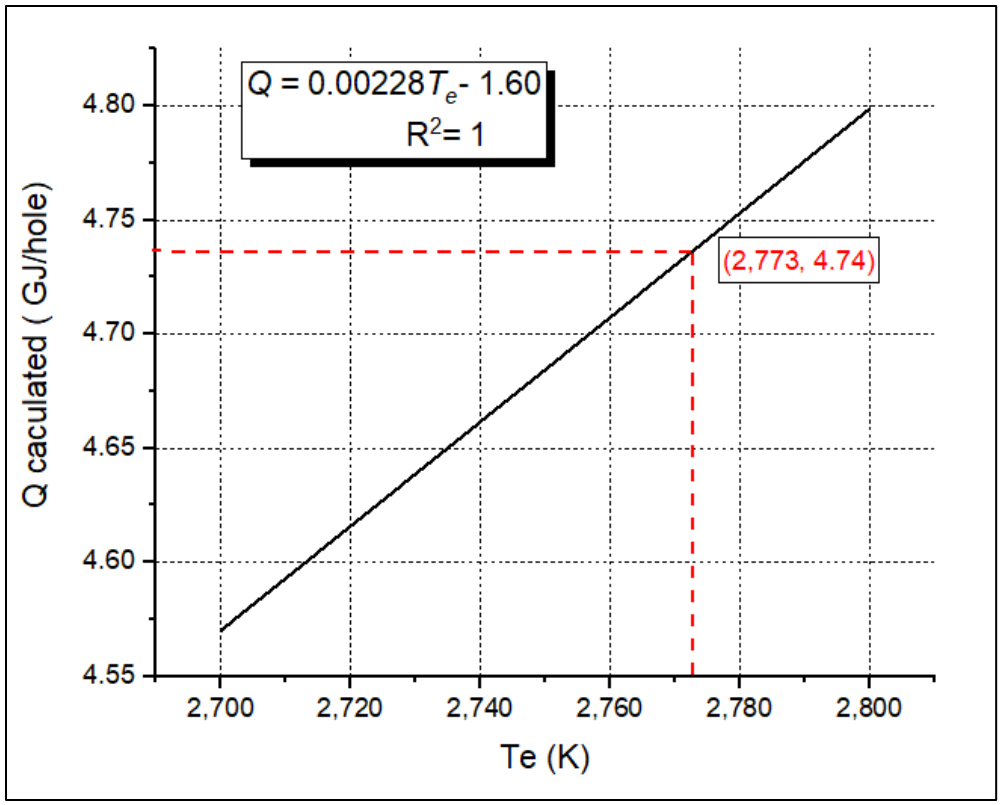

Figure 6.1 Q vs Te curve to find final Temperature of explosion for RIOFRAG

As such, Te was calculated as 2,773 K.

Having defined each value for equation 6.4, It was concluded that P_{Gas} was equal to 1,048 MPa or 15% of P_{DET}.

One reason for the difference determined here, versus values reported by ISEE (2011) and Cunningham (2006) could be that at high temperature, the gaseous products do not behave as an ideal gas. If this were so, it would be necessary to apply a compressibility factor (Z) to equation 6.4. Unfortunately, the advanced chemistry and modelling required for this does not fall within the scope of this research. However, future work in this area could consider such a variation.

6.2 Measuring the efficiency of rock fragmentation in bench blasting

In rock breakage, two dominant fracture zones are created: a Crushing Zone (CZ) and a Tensile Fracture Zone (TFZ), as illustrated in Figure 6.2. According to ISEE (2011), upon detonation, the shock front pushes the borehole walls out and the shock or compressive wave induces high stresses that far exceed the strength of the rock. The combination of these two effects crushes the rock near the borehole wall by subjecting them to high stresses, creating the CZ. As the compressive wave propagates outward, its radial extension creates hoop stresses that exceed the tensile strength of the rock, and so create radial cracks (ISEE, 2011) (TFZ).

Comparing blasting theory and the results observed during the BT procedure described in Chapter 5, both processes present similar CZ and TFZ. The new adaptation of the BT allowed the recognition of the stress pattern through the TFZ, indicating that the crack initiation occurred at the CZ, but with tensile radial fracture propagation into the TFZ. Taking into account these two failure modes and understanding that in rock blasting, generally and particularly for brittle rock like the bench blasts at Highvale mine, the majority of the fragmentation was produced in the TFZ. The stresses observed through the modified BT were thus used for estimating the blasting process efficiency.

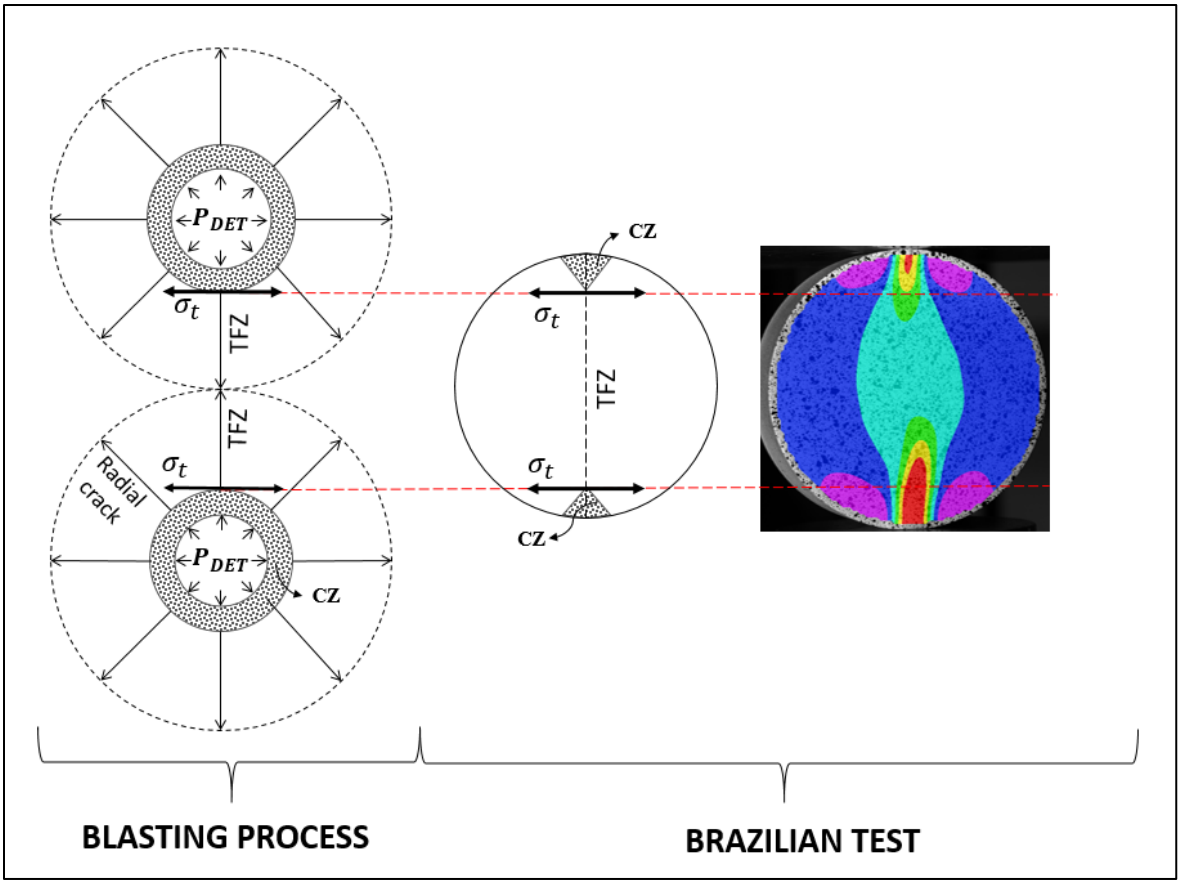

Figure 6.2 Schematic representation of the Crushing and Fracture Tensile Zone in Rock breakage by blasting and Brazilian test

To understand and estimate the influence of each type of pressure on the final size distribution, the TFZ in one hole was considered at three different radii from the center of the hole, representing the maximum zone affected by the blast (at the hole spacing limit), the limit of the crushing zone in closest proximity to the borehole and including fragments representative of a minimum fragment size evaluation, and the area midway between the borehole wall and the maximum zone affected, by 50% of progressive circumferential area, as illustrated in Figure 6.3. At each of the three evaluation zones, the diameter (D_{Max}, D_{CZ} and D_{50}), the circumferential perimeter (C_{Max}, C_{CZ}, C_{50}), and average particle size (X_{MAX}, X_{CZ} , X_{50}) were initially determined to then, estimate and compare the number fractures created in the field at those zones, per fragmentation analysis outcomes, to the expected ideal values at 100% energy usage. To focus the analysis, all calculations honoured blasting theory and the PSD actual results obtained in the field.

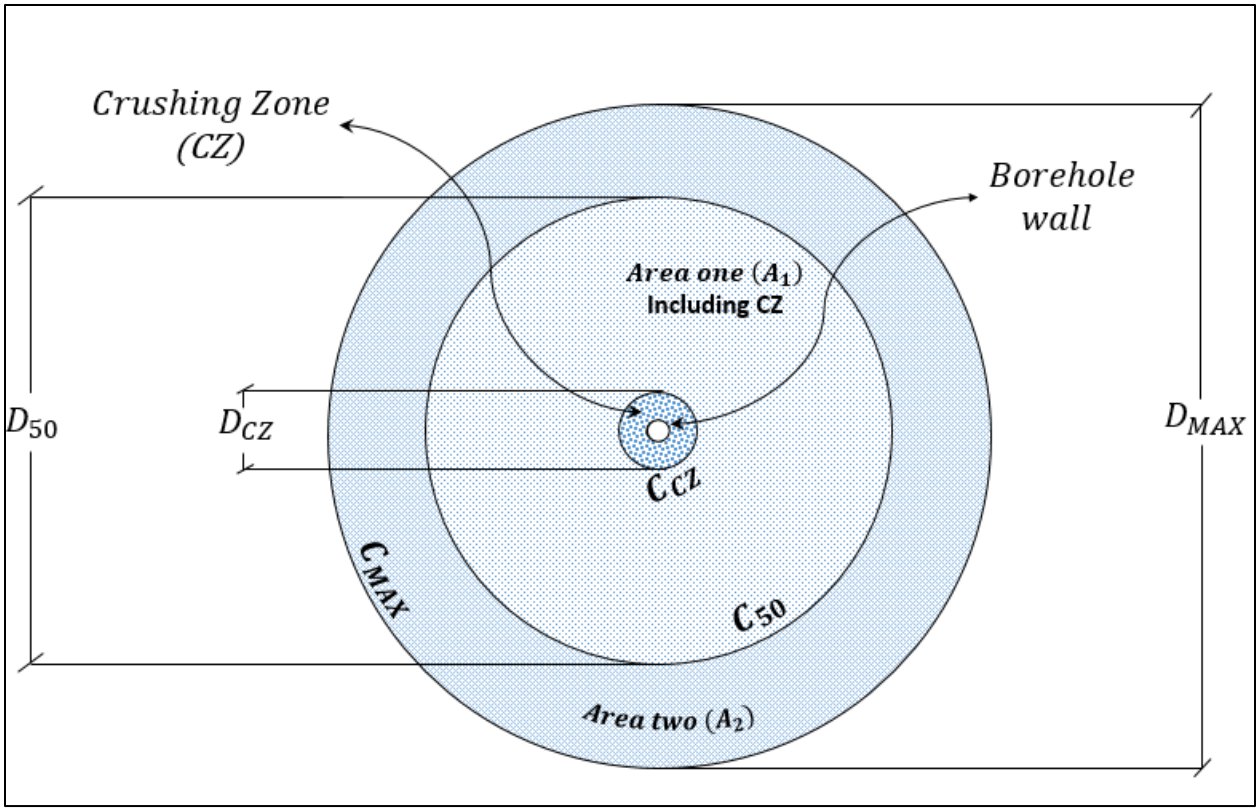

Figure 6.3 Diagrammatic representation of the areas defined for energy efficiency estimation in rock fragmentation in a bench blast

6.2.1 Methodology for characterizing the tensile failure zone around a blast hole

6.2.2 Maximum zone

Under ideal conditions, in a staggered drilling pattern forming an equilateral triangle grid in which the spacing is equal to 1.15 times the burden (the blasthole pattern adopted at the Highvale mine), the impact of the explosive energy must reach at least a distance equal to one spacing (10.3m) in order to maximize the energy distribution that the pattern offers. Under this assumption, a diameter of 10.3 m (D_{Max}) will be used to determine the circumference C_{Max} using equation 6.8.

$$C_{Max} = \pi D_{Max} = \pi \text{ x} 10.3\text{m} = 32.36 \text{ m} \qquad 6.8$$

Since C_{Max} is at the maximum distance from the borehole, the average particle size associated with this area (X_{Max}) will be the maximum particle size measured using Wipfrag (0.734 m), and previously calculated in section 4.1.2.

6.2.3 Middle zone

C_{50} was calculated midway by equal area between C_{Max} and the borehole wall as illustrated in Figure 6.3. Initially the total area affected in one blast hole (A_T) was estimated as 83.25 m^2 using equation 6.9, given D_{Max}= 10.36 m and the borehole plan-section area (A_B) = 0.076 m^2.

$$A_T = \frac{\pi D_{MAX}^2}{4} - A_B \qquad 6.9$$

Since C_{50} was located in the middle of the total area, the latter can be written as follows:

$$A_T = A_1 + A_2 \qquad 6.10$$

$$\text{and } \ldots . A_1 = A_2 \quad \therefore \quad \frac{A_T}{2} = A_1 \qquad 6.11$$

Using equation 6.11, A_1 was equal to 41.6 m^2. To calculate the circumferential perimeter, C_{50}, the diameter of this area D_{50} was used. For this, equations 6.12 and 6.13 were employed.

$$A_1 = \frac{\pi D_{50}^2}{4} - A_B \quad \therefore \quad D_{50} = \sqrt{\frac{4(A_1 + A_B)}{\pi}} = 7.29 \text{ m} \qquad 6.12$$

$$C_{50} = \pi D_{50} = 22.89 \text{ m} \qquad 6.13$$

The average particle size associated with this area (X_{50}) was then, the mean (D50) particle size measured using Wipfrag (0.072 m).

6.2.4 The limit of the Crushing Zone

Estimation of the extension of the CZ in the field is a complex topic and few authors have attempted to determine it. Some have recommended an approach which could be applied to any type of rock and explosive, while others have developed semi-empirical equations which require some rock and explosive parameters to be considered. The following graph summarizes the range of values, as r_c/r_b ratios, that have been suggested by prior researchers. Where r_c and $r_b$are the CZ and borehole radius respectively.

Figure 6.4 Values for r_c/r_b suggested by prior researchers

The values suggested by Djordjevic (1999) and Esen et al., (2003) were calculated using equations 2.1 and 2.2 respectively (see Chapter 2), the dynamic Young's modulus equation suggested by Esen et al., (2003) and assuming the same value for dynamic and static Poisson's ratio. Atlas Powder Company (1987) recommended an interval for any field conditions presented; where Bastante et al.,(2014) calculated the interval for a granite rock and using ANFO as a blasting agent. Lu et al., (2016) developed a model which was based on data reported in the literature; where, the investigation involved quartzite, granite, limestone and Siltstone rock types, with ANFO and Emulsion as explosives.

From Figure 6.4, the most common interval for r_c/r_b ratio lies between 1 and 5. For CZ assessment here, at middle value of 3, was taken as representative. This was in good agreement with the ratio calculated using the equation recommended by Esen et al., (2003). According to Lu et al., (2016), the equation proposed by Djordjevic (1999), overestimated the crushing zone while the one suggested by Esen et al., (2003) is closer to reality. Finally, here for the Highvale mine, r_c was determined at 3 times the borehole radius, and C_{CZ} as follows:

$$C_{CZ} = \pi D_{CZ} = \pi \text{ x } 0.933 \text{ m} = 2.93 \text{ m} \quad 6.14$$

Where D_{CZ} is the diameter of the CZ measured from the center of the borehole in m.

To calculate the average particle size associated with C_{CZ} (X_{CZ}), a relationship based on areas was established. The area of the crushing zone *(*A_{CZ}) was initially determined by equation 6.15 and expressed as a percentage of the total area (A_T). This percentage was applied to the PSD and the size fraction with the same percentage passing was used as the average size in the CZ.

$$A_{CZ} = \frac{\pi D_{CZ}^2}{4} - A_B \quad 6.15$$

Using equation 6.15, A_{CZ} was calculated as 0.73% of A_T. So, the size value of $D_{0.73}$ from the field measured PSD was used as X_{CZ}, equal to 0.007 m.

The following Table summarizes the values above, calculated by circumference.

Table 6.4 Perimeter and average particle size determined at $C_{MAX,}$ C_{50} & C_{CZ}.

	Circumference - C (m)	**Average particle Size - X (m)**
Maximum Zone	32.36	0.734
Middle Zone	22.89	0.072
Outer limit of the Crushing Zone	2.93	0.007

6.2.5 A practical tool for pressure expenditure estimation

The borehole has been divided into 3 circumferential zones that account for the TFZ and where the pressure expenditure will be estimated. The first step was the determination of the actual number of radial fractures (ARF_i) crossing each i^{th} circumference using equation 6.16, and the values indicated in Table 6.4.

$$ARF_i = \frac{C_i}{X_i} \quad 6.16$$

The values obtained via equation 6.16 were then compared with the ideal or maximum number of radial cracks crossing each i circumference (MRF_i). Key to this however is an understanding of the distribution of pressure energy at the outer edge of the CZ and in the TFZ. Clearly, P_{Det} is the

pressure available to create the CZ, so by means of a relationship between the detonation pressure and tensile strength of the rock, the maximum number of radial cracks crossing the CZ may be determined. However, for the TFZ, the relationship is not that simple because there is no unified theory to quantify the amount of gas or detonation pressure used to create radial fractures during rock fragmentation. In order to determine the distribution of pressures, a pragmatic approach was taken, and pressures were estimated empirically and sequentially from the pressure in the previous zone.

Without any knowledge of the rock mass and the pre-blasting rock mass fracture density it is difficult to know how much pressure (particularly gas pressure) at sequential stages of the fracture process is lost through existing fracture network venting to the atmosphere. In the case of the Highvale Mine test site, the rock mass exhibited bedding layers at the shale/sandstone/coal contacts; but there were no fractures evident at those contacts, nor at any orientation in any form within the mass prior to blasting. As such, the target blast zone was deemed to be essentially intact. During blasting, observation of the blasting event identified minimal ejection of stemming material suggesting that good blast energy containment within the pattern was achieved on detonation. With this in mind, the analysis that follows assumes conversation of energy in the progressive sequential evaluation of available energy to effect fragmentation.

Outside the scope of the work described here would be a future work evaluation of the impact of energy containment as a function of rock mass fracture density, as may be evaluated through a rock mass rating system. This would potentially set the next logical evaluation step in moving this research area forward.

The energy conservation assumed sequential steps are thus:

The first consequence of detonation is at the CZ. Here, the maximum number of radial cracks crossing (C_{CZ}) were computed using equation 6.17. Comparing the results obtained from equation 6.16 and 6.17, the percentage of pressure used at the limit of the CZ ($\%P_{u,cz}$) and remaining available shock pressure to produce further fracturing beyond CZ ($P_{a,cz}$) were calculated with the following equations 6.17, 6.18 and 6.19.

$$MRF_{CZ} = \frac{P_{Det}}{\sigma_{\tau}} \qquad 6.17$$

$$\frac{\mathrm{ARF_{CZ}}}{\mathrm{MRF_{CZ}}}\ \mathrm{x}\ 100 = \%\mathrm{P_{u,cz}} \tag{6.18}$$

$$\mathrm{P_{Det}}\left(1 - \mathrm{P_{u,cz}}\right) = \mathrm{P_{a,cz}} \tag{6.19}$$

Should be noted that $\mathrm{MRF_{CZ}}$ indicates the number of tensile radial cracks that emanate from the CZ due to the detonation pressure and represent the starting point for radial tensile crack propagation. This explains why the tensile strength σ_τ was used into equation 6.17.

The next sequential area of interest occurs at $\mathrm{C_{50}}$. Here $\mathrm{P_{Gas}}$ and $\mathrm{P_{a,cz}}$ are both involved in the fracturing process, so equation 6.17, 6.18 and 6.19 were re-written as follows:

$$\mathrm{MRF_{50}} = \frac{\mathrm{P_{gas}} + \mathrm{P_{a,cz}}}{\sigma_\tau} \tag{6.20}$$

$$\frac{\mathrm{ARF_{50}}}{\mathrm{MRF_{50}}}\ \mathrm{x}\ 100 = \%\mathrm{P_{u,50}} \tag{6.21}$$

$$\left(\mathrm{P_{gas}} + \mathrm{P_{a,cz}}\right)\left(1 - \mathrm{P_{u,50}}\right) = \mathrm{P_{a,50}} \tag{6.22}$$

Finally, for the case of $\mathrm{C_{Max}}$ the pressure involved was the remaining pressure at $\mathrm{C_{50}}$ ($\mathrm{P_{a,50}}$). Here, equation 6.20, 6.21 and 6.22 were expressed as:

$$\mathrm{MRF_{Max}} = \frac{\mathrm{P_{a,50}}}{\sigma_\tau} \tag{6.23}$$

$$\frac{\mathrm{ARF_{Max}}}{\mathrm{MRF_{Max}}}\ \mathrm{x}\ 100 = \%\mathrm{P_{u,Max}} \tag{6.24}$$

$$\mathrm{P_{a,50}}\left(1 - \mathrm{P_{u,Max}}\right) = \mathrm{P_{a\ ,Max}} \tag{6.25}$$

The following table summarizes the energy expenditure values estimated at each circumference.

Table 6.5 Values calculated to measure the blasting process efficiency

C_i	Pressure involved (MPa)	ARF_i	MRF_i	$\%P_{u,i}$	$P_{a,i}$ (MPa)
C_{CZ}	P_{Det} = 7,015	448	1,486	30.2	4,899
C_{50}	$P_{gas} + PA_{CZ}$ = 5,946	317	1,260	25.2	4,451
C_{Max}	PA_{50} = 4,451	44	943	4.67	4,242

Knowing the input pressure (P_{Det} +P_{gas}) and the available pressure at the end of C_{Max} ($P_{a,Max}$), it was concluded that 52.6% of the energy was lost and therefore, 47.4% used to fragment the rock (the overall efficiency of the process).

6.2.6 The simplified 'cookbook' approach for operations

In this section, a "cookbook" flow chart is presented to illustrate the steps that could easily be performed in the field to estimate the efficiency of the blasting process. This methodology analyzes the pressure expenditure at three different locations from the borehole, which in turn allows an opportunity for blast design improvement to meet operational rock fragmentation requirements. The process is simple and practical, and only a few steps are needed for blast assessment.

For a given mine location and geology, the BT evaluation of σ_τ used in part 5 (rock tensile strength determination) is unique, such that calibration by mine site and geology is required to make the "cookbook" approach viable.

If, as is suggested for future work, a rock mass is blasted, then rock mass rating (RMR) would impact the outcome of the "cookbook approach", requiring a relationship between RMR and percentage energy or pressure to be investigated.

1 Explosive characterization

Measure → a) Density (ρ)
b) Velocity of detonation (VOD)

Output → $P_{Det} = \frac{\rho\, VOD^2}{4}$

$P_{Gas} \sim 0.2 P_{Det}$

2 Muck pile description

Identify → a) Spacing (S)
b) Borehole diameter (D_B)
c) Photograph the muckpile (use WipFrag or alt.)
d) Image processing

Output → Actual fragment size distribution (PSD)

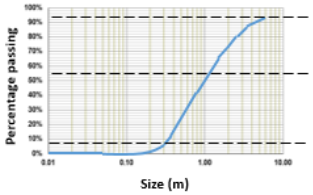

X_{Max}= maximum particle size

X_{50}= mean particle size

X_{CZ}= particle size at the edge of the Crushing Zone (CZ) . Assuming a Diameter (D_{CZ}) of 3 times D_B

$$X_{CZ} = X_{\left[\frac{8}{\left(\frac{S}{D_B}\right)^2 - 1} * 100\right]}$$

↓ % *passing*

3 Rock tensile strength determination

Perform → a) Sample discs with thickness (t) to diameter (D) ratio of 0.5
b) Use on-site " Shop press" to record P_{Max}
c) Apply Brazilian Test equation $\sigma_{BT} = {}^{2P_{Max}}/_{\pi Dt}$

Output → $\sigma_T \sim 0.5\sigma_{BT}$

4 Use the results in 1, 2 and 3 to evaluate the blast

a) Create a simple spread sheet for every day use. → **Output**

	% Pressure expenditure (%P)	**Available pressure (P_a)**
End Crushing Zone	$\%P_{u,CZ} = \left({}^{(3\pi D_B \sigma_T)}/_{(P_{Det} X_{CZ})}\right) x100$	$P_{a,CZ} = (1 - P_{u,CZ}) P_{Det}$
Middle Zone (50% zone)	$\%P_{u,50} = \left({}^{\sigma_T \pi \sqrt{0.5(S^2 + D_B{}^2)}}/_{[X_{50}(0.2P_{Det} + P_{CZ})]}\right) x100$	$P_{a,50} = (1 - P_{u,50})(P_{Gas} + P_{a,CZ})$
Maximum Zone	$\%P_{u,Max} = \left({}^{(\pi S \sigma_T)}/_{(P_{50} X_{Max})}\right) x100$	$P_{a,Max} = (1 - P_{u,Max}) P_{a,50}$

5 $P_{a,Max}$ = Pressure lost or unused in breaking the rock

Figure 6.5 Flow chart

6.3 Outcome and discussion

Form table 6.5, 4,242 MPa is then either the pressure lost or wasted as vibration (peak particle velocity), noise (airblast), heat, rock movement and flyrock (projectiles) or simply insufficient to generate further rock fracture extension, during the blasting process. This corresponds to 52.6% of the input pressure into the system ($P_{Det} + P_{gas}$). This means that 47.4 % of the energy was used to actually fracture the rock.

The values obtained are greater than those found by (Ouchterlony et al., 2003; José A. Sanchidrián et al., 2007; Hamdi et al., 2008; Calnan, 2015). However, the methodology that these four researchers specifically and in comparison followed used the same mathematical relationships between rock fracture toughness and final surface area of broken rock, so it is not surprising that their findings are similar; and different from the findings here. One aspect that might introduce significant error into this prior research is the high impact associated with particle shape into their estimations. Cubic shapes of broken rock were assumed by all the authors, which indeed, it is one of the most uncommon geometries for blasted rock.

There is a possibility that the value of energy used for rock fragmentation, might be due to the small gas pressure value calculated using the ideal gas equation. As mentioned, P_{Gas} was found to be 15% of the detonation pressure while authors like ISEE (2011) and Cunningham (2006) suggested about 45 to 50% of P_{Det}. Future work in this area could consider such a variation.

Table 6.5 not only indicates the final efficiency of the blasting process as a number, as has been done before, it also presents three important areas for analysis (at the hole spacing distance, limit of the CZ and the midway between them). For example, at the Highvale mine, where the blasted rock is excavated by dragline, the efforts can be focused on incrementing the $\%P_u$ at the C_{50} and C_{Max} areas. One technique to accomplish this, would be the use of air decking to decrease the initial detonation pressure transmitted to the surrounding rock in the CZ, but as such effectively increase the amount of gas pressure reaching the further C_{50} and C_{Max} zones, as less initial fractures are required for propagation. This would reduce the proportion of oversize fragments as greater gas pressure would extend small size fraction fractures further. Also, this could be used as a strategy to reduce the amount of explosive required per hole to effect the same size distribution but with only less small size fraction closer to the borehole, and in turn costs.

The operational performance of the blasting process can also be measured based on the results indicated in Table 6.5, and new target KPI's may be established per operational requirements.

7. CONCLUSIONS AND FUTURE WORK

In an ideal rock blasting process, 100% of the energy released at detonation would be used to achieve the desired fragmentation outcome, but in reality, much of this energy is consumed generating noise, heave, flyrock, vibration and heat. To attempting reduction of such unwanted by products, we need to know how much of the input energy is actually used in rock fragmentation and understand how such energy can be better utilized to obtain a fragmentation size distribution meeting mining and milling input requirements.

Initially, field data and representative rock samples were collected at the Highvale Mine test site, along with photographic images of blasted rock piles. The method of capturing the images was vital to the success of the subsequent process, and previous analyses of muckpile characteristics at the mine site were important to determine the appropriate tools for capturing and processing such images to generate blasted rock particle size distributions. Consistent sampling techniques were employed to reduce possible error associated with the image assessment process itself. It is suggested that the mine itself could utilize such techniques for routine blast performance evaluation, employing a more standardized approach to capturing and processing images.

The amount of explosive energy released by the detonation process was determined in terms of gas pressure (P_{Gas}) and detonation pressure (P_{DET}). P_{DET} was estimated using a widely accepted equation defined as one-fourth of the explosive density times the square of the velocity of detonation; whereas, for P_{Gas} estimation, a new approach was proposed via for simplicity, in illustrating the principle of application, the ideal gas equation. The P_{Gas} was estimated as 15% of the P_{DET}, a lower value than the 50-45% currently adopted in the mining industry. The discrepancy may be explained via assuming the blast gases to behave as ideal gases. It would be interesting to analyze P_{Gas} by applying a non-ideal approach, but outside the scope of this study.

Laboratory work was carried out to determine the mechanical properties of the sandstone from the mine. Point Load tests (PLT) and the unconfined compressive strength (UCS) tests were undertaken with values of 113.4 MPa and 107.1 MPa obtained respectively. The results were similar, where the value obtained by the UCS test was within the range calculated by the PLT. It is noted that the PLT values were obtained using a correction factor (K) of 23 as suggested by D5731-16 ASTM (2016). However, if more data had been obtained from UCS tests, a regression

analysis could have produced a more accurate K value for the sandstone under test. The PLT was confirmed as an appropriate tool for UCS estimation

The tensile strength of the rock was tested in 3 ways, a Brazilian Test (BT), an experimental technique using a Digital Image Correlation Technique (DIC) and a direct Pull Test (DPT). The results from these were recorded as $\sigma_{t(BT)}$, $\sigma_{t(S)}$ and $\sigma_{t(PT)}$ respectively.

- The BT revealed two mainly failure zones: A Crushing Zone (CZ) at the loading contact points, and a vertical tensile crack along the sample diameter (the TFZ). The average $\sigma_{t(BT)}$ calculated was 8.67 ± 1.86 MPa.
- DIC technology proved a useful tool for full-field strain measurements while conducting a BT test. This approach coupled with the BT revealed two different types of failure when the diametral compressive load was applied into the specimen (type a and type b). In both test, CZ and TFZ were identified just before failure. The main differences between types a and b were observed just after failure initiation. Immediately on taking yield load, 57% of the samples (type a) displayed high values of strain in all directions, in the area where the load was applied (CZ). These increased with load. On the contrary, in 43% of the samples (type b), no CZ was evident at the start, but the center of the sample was subjected to high values of tensile strain(ε_x), which then propagated in the vertical plane as predicted by the BT theory. However, this propagation eventually ceased and the behaviour became very similar to that in type a. The difference could be related to the nature of the contact between the sample and the loading platens. Small variations in the flatness of both likely created discrepancies at the onset of loading. However, it is noted that this had no influence on the CZ and TFZ created at the end of the test or just before rock failure.
- Stress values were obtained from strain measurements applying theory of elasticity. An average value of 0.35 MP was calculated for τ_{xy} along the vertical loading diameter, while σ_x and σ_y reached peak values near the loading contact areas and decreased towards the center eventually reaching a steady state when solely tensile failure cracks propagated in the TFZ. The mean value was interpreted as the maximum tensile stress required for the rock to fail in tension along the vertical loading plane. Accordingly, $\sigma_{t(S)}$ calculated was 4.72 ± 0.82 MPa.

- However, as the BT theory predicts, the DIC approach revealed a maximum stress at the CZ. So, it was assumed that fracture initiated within this area and propagated towards the center of the sample. The σ_y/σ_x ratio was estimated to be -2.36 ± 0.34 while the theory predicted -3. It was concluded that the BT overestimates the result, and since the crack initiation was not apparent at the center of the sample, the use of this approach for tensile strength determination when flat platens are used is suspect. However, for simplicity and ease of field application, the tensile strength was initially calculated using the BT, and then adjusted per the indications of the DIC approach to show that the tensile strength was in fact about 50% of the BT evaluation.
- Comparing the mean values of $\sigma_{t(S)}$ and $\sigma_{t(BT)}$, the result obtained by the DPT suggests a higher tensile strength. There are two potential explanations for this. The first is associated with the amount of "energy" or in this case, "tensile stress" needed to initiate or propagate a tensile fracture. As noted by the DIC approach, the tensile crack initiates at the CZ where high pressure is needed but, the pressure associated with its propagation at the TFZ is less. The difference might also be explained where insufficient information was achieved from the DIC approach before failure due to the slow image capture rate. Further work using BT with cameras at a higher frame rate capture would undoubtedly enable a more substantiated conclusion to be drawn.

A practical methodology for blasting performance assessment was introduced in which the minimum, mean and maximum actual fragment size was analyzed proportionate to the P_{Gas} and P_{DET} 'spent' to actually fragment the in-situ rock. The results showed, as expected, a high value (52.6%) of input pressure lost or unused in breaking the rock. The results suggest that tensile fractures in rock breakage by blasting are produced by the combination of the effect produced by the detonation and gas pressure. However, the evaluation is unable to predict which mechanisms has more effect on crack development. P_{DET} was dominant in the crushing zone, and in initiating the radial cracks, but it also likely that it continues to propagate some of the tensile fractures that reached the C_{50} zone and quite possibly the C_{Max} area.

The blast performance approach illustrated by this research work allows measurement of the efficiency not only of the entire blasting process, but also, if it is desired, how much energy was required to produce a minimum, mean and maximum fragment size. This latter

contribution allows mining operations to focus their efforts on improving the results proportionate to operational mining and milling needs.

BIBLIOGRAPHY

Akhavan, J. J. (2004). *The Chemistry of Explosives* (2nd, Ed.). Retrieved from https://search.ebscohost.com/login.aspx?direct=true&db=e000xna&AN=496199&site=eds-live&scope=site

Alitalesh, M., Mollaali, M., and Yazdani, M. (2015). Correlation between uniaxial strength and point load index of rocks. *15th Asian Regional Conference on Soil Mechanics and Geotechnical Engineering, ARC 2015: New Innovations and Sustainability*, 504–507. https://doi.org/10.3208/jgssp.IRN-08

Araldite. (2019). Araldite® profesional adhesives. Retrieved from http://go-araldite.com/products/epoxy-adhesives/araldite-crystal-2-x15ml-tube

Asgari, A. (2016). Blast-Induced Rock Fracturing and Minimizing Downstream Comminution Energy Consumption. *41st Annual Conference on Explosives and Blasting Technique*, (February 2015). At New Orleans, La.

ASTM. (2002). Standard Test Method for Unconfined Compressive Strength of Intact Rock Core D2938-95 (Reapproved 2002). *ASTM International*. https://doi.org/10.1520/D2938-95R02

ASTM. (2008). Standard Test Method for Direct Tensile Strength of Intact Rock Core Specimens D2936-08. *ASTM International*. https://doi.org/10.1520/D2936-08.2

ASTM. (2014). Standard test method for compressive strength and elastic moduli of intact rock core specimens under varying states of stress and temperatures. *ASTM International*. Retrieved from https://doi-org.login.ezproxy.library.ualberta.ca/10.1520/D7012-14E01

ASTM. (2016a). Standard Test Method for Determination of the Point Load Strength Index of Rock and Application to Rock Strength Classifications D5731-16. *ASTM International*. https://doi.org/10.1520/D5731-08.2

ASTM. (2016b). Standard Test Method for Splitting Tensile Strength of Intact Rock Core Specimens D3967-16. *ASTM International*. Retrieved from https://doi.org/10.1520/D3967-16

Atlas Powder Company. (1987). *Explosives and Rock Blasting*. Dallax, Tex: Atlas Powder Company.

Bamford, T., Esmaeili, K., and Schoellig, A. P. (2017). A real-time analysis of post-blast rock fragmentation using UAV technology. *International Journal of Mining, Reclamation and Environment*, *31*(6), 439–456. https://doi.org/10.1080/17480930.2017.1339170

Bastante, F., Alonso, E., and González, M. A. (2014). An approximation to the prediction of the extent of the area crushed around a blasting drill. *Rock Engineering and Rock Mechanics: Structures in and on Rock Masses - Proceedings of EUROCK 2014, ISRM European Regional Symposium*, (i), 689–693. https://doi.org/10.1201/b16955-118

Belrhiti, Y., Dupre, J. C., Pop, O., Germaneau, A., Doumalin, P., Huger, M., and Chotard, T. (2017). Combination of Brazilian test and digital image correlation for mechanical characterization of refractory materials. *Journal of the European Ceramic Society*, *37*(5), 2285–2293. https://doi.org/10.1016/j.jeurceramsoc.2016.12.032

Bieniawski, Z. T. (1974). THE POINT-LOAD TEST IN GEOTECHNICAL PRACTICE. *Engineering Geology*, *9*, 1–11.

Bilotta, A., Ceroni, F., Lignola, G. P., and Prota, A. (2017). Use of DIC technique for investigating the behaviour of FRCM materials for strengthening masonry elements. *Composites Part B: Engineering*, *129*, 251–270. https://doi.org/10.1016/j.compositesb.2017.05.075

Borana, S. ., Yadav, S. ., and Parihar, S. . (2018). Image Processing Analysis of Blast Fragmentation : A Case Study of Sandstone Mining Area of Jodhpur. *International Journal of Research in Advent Technology*, *6*(October). https://doi.org/10.13140/RG.2.2.24151.73120

Britton, R. R., Skidmore, D. R., and Otuonye, F. O. (1984). Simplified calculation of explosives-generated temperature and pressure. *Mining Science and Technology*, *1*(4), 299–303. https://doi.org/10.1016/S0167-9031(84)90339-6

Brunton, I., Thornton, D., Hodson, R., and Sprott, D. (2003). *Impact of Blast Fragmentation on Hydraulic Excavator Dig Time*. (November), 3–5.

Calnan, J. (2015). *Determination of Explosive Energy Partition Values in Rock Blasting Through Small-Scale Testing* (University of Kentucky. Mining Engineering. 24. Thesis and Dissertation). Retrieved from http://uknowledge.uky.edu/mng_etds/24

Carlsson, O., and Nyberg, L. (1983). A method for estimation of fragment size distribution with automatic image processing. In *Firts International Symposium on Rock Fragmentation by blasting* (pp. 333–337). Lulea, Sweden: Daniel Johansson.

Cebrian, B., and Flores, J. (2015). Drilling and Blasting Optimization. *International Society of Explosives Engineers*, 1–11.

Choudhary, B. S., and Mishra, A. K. (2016). *Effect of Stemming to Burden Ratio and Powder Factor on Blast Induced Rock Fragmentation – A Case Study*. (December). https://doi.org/10.1088/1757-899X/225/1/012191

Chow, E., Zeng, H., Baumann, M., and Tafazoli, S. (2012). Automation of Rock Fragmentation Analysis. In *International Society of Explosive Engineers*. NASHVILLE, TN USA.

Chow, E., Zeng, H., and Tafazoli, S. (2011). Measuring Blast Fragmentation by Analyzing Shovel Bucket Contents. *Proceeding of 37th Annual Conference on Explosives and Blasting Technique*, 11.

Correlated Solutions. (2007). *Vic-3D 2007 Testing Guide*.

Correlated Solutions. (2016). *Strain Calculation in Vic-3D*. Retrieved from http://www.correlatedsolutions.com/supportcontent/strain.pdf

Correlated Solutions. (2018). *Application Note AN-1701 Speckle Pattern Fundamentals*. Retrieved from http://correlatedsolutions.com/support/index.php?/Knowledgebase/Article/View/80/0/speckle-pattern-fundamentals

Cowperthwaite, M., and Zwisler, W. . (1974). *TIGER Computer Program Documentation*. Retrieved from National Technical Information Service website: https://apps.dtic.mil/dtic/tr/fulltext/u2/a002791.pdf

Cunningham, C. (1996). Lessons from the Compaphoto technique of fragmentation measurement. In J. A. Franklin and T. Katsabanis (Eds.), *Measurement of Blast Fragmentation : Proceedings of the Fragblast-5 Workshop On Measurement of Blast Fragmentation* (pp. 53–57). Montreal, Canada: A.A. Balkema.

Cunningham, C. (2006). Blasthole Pressure : What it really means and how we should use it. *8th Annual Conference on Explosives and Blasting Technique*, *2*(2), 1–10.

Dahlhielm, S. (1996). Industrial applications of image analysis -The IPACS system. In J. A. Franklin and T. Katsabanis (Eds.), *Measurement of Blast Fragmentation : Proceedings of the Fragblast-5 Workshop On Measurement of Blast Fragmentation* (pp. 59–65). Montreal, Canada: A.A. Balkema.

Debnath, A., and Jha, A. (2013). Blast Instrumentation - A Key to Mine Productivity. *Canadian Institute of Mining, Metallurgy and Petroleum*, 11.

Djordjevic, N. (1999). Two-component of blast fragmentation. *Proceedings of the Sixth International Symposium on Rock Fragmentation by Blasting-Fragblast*, 213–219. Retrieved from https://www.onemine.org/document/abstract.cfm?docid=188182&title=A-TwoComponent-Model-of-Blast-Fragmentation

Djordjevic, N. (2001). Practical application of detonation code for explosive selection. *The AusIMM Proceedings*, *306*(1), 23–26. International Society of Explosives Engineers.

Downs, D. C., and Kettunen, B. E. (1996). On-line fragmentation measurement utilizing the CIAS(R) system. In J. A. Franklin and T. Katsabanis (Eds.), *Measurement of Blast Fragmentation : Proceedings of the Fragblast-5 Workshop On Measurement of Blast Fragmentation* (pp. 79–82). Montreal, Canada: A.A. Balkema.

Edgen, D. J., and Franklin, J. A. (1996). Desintegration, fusion and edge net fidelity. In J. A. Franklin and T. Katsabanis (Eds.), *Measurement of Blast Fragmentation : Proceedings of the Fragblast-5 Workshop On Measurement of Blast Fragmentation* (pp. 127–132). Montreal, Canada: A.A. Balkema.

Elghazel, A., Taktak, R., and Bouaziz, J. (2015). Determination of elastic modulus, tensile strength and fracture toughness of bioceramics using the flattened Brazilian disc specimen: analytical and numerical results. *Ceramics International*, *41*(9), 12340–12348. https://doi.org/10.1016/j.ceramint.2015.06.063

Elhakim, A. F. (2015). The use of point load test for Dubai weak calcareous sandstones. *Journal of Rock Mechanics and Geotechnical Engineering*. https://doi.org/10.1016/j.jrmge.2015.06.003

Elliott, R. J., and Wedgewood, D. (2019). Use of Signature Hole Analysis for Blast Vibration Control at the Highvale Mine. *The Journal of Explosives Engineering*, *36*, 6–14.

Esen, S., Onederra, I., and Bilgin, H. A. (2003). Modelling the size of the crushed zone around a blasthole. *International Journal of Rock Mechanics and Mining Sciences*, *40*(4), 485–495. https://doi.org/10.1016/S1365-1609(03)00018-2

Fairhurst, C. (1964). On the validity of the “Brazilian” test for brittle materials. *International Journal of Rock Mechanics and Mining Sciences And*. https://doi.org/10.1016/0148-

9062(64)90060-9

Fenton, M., Langenberg, C., Jones, C., Trydell, M., Paulowicz, J., Tapics, J., and Nikols, D. (1985). *Tour of the Highvale open pit coal mine*. Edmonton, Alberta.

Fifer, R. A., and Morris, J. B. (1993). *Approximate Techniques for the Estimation of Heats of Explosion (HEX) Using Thermochemical Codes*. *i*, 375–389.

Franklin, J. A. (1996). Fragment size measurements and statistics. In J. A. Franklin and T. Katsabanis (Eds.), *Measurement of Blast Fragmentation : Proceedings of the Fragblast-5 Workshop On Measurement of Blast Fragmentation* (pp. 23–31). Montreal, Canada: A.A. Balkema.

Freiman, S. W. (2012). *The fracture of brittle materials*. Hoboken, N.J.: John Wiley & Sons.

Fried, L. E. (1994). *CHEETA 1.0 User's Manual*. 137. Retrieved from https://www.osti.gov/servlets/purl/10165726

Frimpong, S., Somua-gyimah, G., Nyaaba, W., and Gbadam, E. (2019). Formation Fragmentation Modeling and Impact on Dragline Excavation Performance in Surface Mining Operations. *International Journal of Mining Science*, *5*(1), 11–21. https://doi.org/10.20431/2454-9460.0501002

Girdner, K. ., Kemeny, J. ., Srikant, A., and McGill, R. (1996). The split system for analyzing the size distribution of fragmented rock. In J. A. Franklin and T. Katsabanis (Eds.), *Measurement of Blast Fragmentation : Proceedings of the Fragblast-5 Workshop On Measurement of Blast Fragmentation* (pp. 101–108). Montreal, Canada: A.A. Balkema.

Gkikizas, N. (2016). *EXAMINATION OF THE EFFECT OF TIME DELAY ON FRAGMENTATION*. Queen's University.

Gokhale, B. (2011). Rotary Drilling and Blasting in Large Surface Mines. In *Rotary Drilling and Blasting in Large Surface Mines*. https://doi.org/10.1201/b10972

Hamdi, E., Bouden Romdhane, N., du Mouza, J., and Le Cleac'h, J. M. (2008). Fragmentation energy in rock blasting. *Geotechnical and Geological Engineering*, *26*(2), 133–146. https://doi.org/10.1007/s10706-007-9153-4

Hassani, F. P., Scoble, M. J., and Whittaker, B. N. (1980). Application of the point load index test to strength determination of rock and proposals for a new size-correction chart. *21st U.S. Symposium on Rock Mechanics, USRMS 1980*.

Hondros, G. (1959). The Evaluation of Poisson's Ratio and the Modulus of Materials of Low Tensile Resistance by the Brazilian (Indirect Tensile) Test with Particular Reference to Concrete. *Australian Journal of Applied Science*, *10*, 243–268.

Hosseini, Z., Amirrahmat, M., and Khoshroo, S. H. (2004). Determination of Ore Fragmentation by Image Analysis in Sarcheshmeh Mine. *Proceedings of the Thirtieth Annual Conference on Explosives and Blasting Technique*, *1*, 99–108.

ISEE. (2011). *ISEE Blasters' Handbook* (18th ed.; J. Stiehr, Ed.). Cleveland, Ohio: International Society of Explosives Engineers.

ISRM. (1978). International society for rock mechanics commission on standardization of

laboratory and field tests: Suggested methods for determining tensile strength of rock materials. *International Journal of Rock Mechanics and Mining Sciences & Geomechanics Abstracts*, *15*(3), 99–103. https://doi.org/10.1016/0148-9062(78)90003-7

ISRM. (2007). Suggested Method for Determining the Uniaxial Compressive Strength and Deformability of Rock Materials. In R. Ulusay and J. . Hudson (Eds.), *The complete ISRM suggested methods for rock characterization, testing and monitoring : 1974-2006* (pp. 137–140). Ankara: Commission on Testing Methods, International Society of Rock Mechanics.

Kabwe, E. (2017). Improving Collar Zone Fragmentation by Top Air-Deck Blasting Technique. *Geotechnical and Geological Engineering*, *35*(1), 157–167. https://doi.org/10.1007/s10706-016-0094-7

Kahriman, A., Tuncer, G., Karadogan, A., and Ozdemir, K. (2005). Kuz-Ram and Digital Image Processing System Combination to Determine Specific Blasting Parameters. *Proceedings of the 30st Annual Conference on Explosives and Blasting Technique*, *1*, 1–9. New Orleans,Louisiana: International Society of Explosives Engineers.

Karimi, A., Shojaei, A., and Razaghi, R. (2017). Viscoelastic mechanical measurement of the healthy and atherosclerotic human coronary arteries using DIC technique. *Artery Research*. https://doi.org/10.1016/j.artres.2017.02.004

Kavdir, E. Ç., and Aydin, M. D. (2019). The investigation of mechanical properties of a structural adhesive via digital image correlation (DIC) technic. *Composites Part B: Engineering*, *173*, 14. https://doi.org/10.1016/j.compositesb.2019.106995

Klapötke, T. M. (2012). *Chemistry of High-Energy Materials* (Vol. Secon). Retrieved from http://search.ebscohost.com/login.aspx?direct=true&db=e000xna&AN=471075&site=ehost-live&scope=site

Kojovic, T., Michaux, S., and McKenzie, C. (1995). Impact of blast fragmentation on crushing and screening operations in quarrying. *Proceedings of the EXPLO '95 Conference*, 427–436.

Kumara, J., Hayano, K., and Ogiwara, K. (2012). Image Analysis Techniques on Evaluation of Particle Size Distribution of Gravel. *International Journal of Geomate*, *3*(1999), 290–297. https://doi.org/10.21660/2012.5.1261

Langenberg, W., Berhane, H., Sweet, A. R., Marchionu, D., and Heaman, L. (2007). Regional Correlations of the Ardley Coal Zone, Alberta. In *EUB/AGS Earth Sciences Report* (p. 31). Retrieved from https://ags.aer.ca/publications/ESR_2007_05.html

Ledoux, L. (2015). *THE ROLE OF STRESS WAVES AND GASES IN THE DEVELOPMENT OF FRAGMENTATION*. Queen's University.

Li, D., and Wong, L. N. Y. (2013). Point load test on meta-sedimentary rocks and correlation to UCS and BTS. *Rock Mechanics and Rock Engineering*, *46*(4), 889–896. https://doi.org/10.1007/s00603-012-0299-x

Liu, Y., Dai, F., Xu, N., Zhao, T., and Feng, P. (2018). Experimental and numerical investigation on the tensile fatigue properties of rocks using the cyclic flattened Brazilian disc method. *Soil Dynamics and Earthquake Engineering*, *105*(October 2017), 68–82. https://doi.org/10.1016/j.soildyn.2017.11.025

Lopez Jimeno, C., Lopez Jimeno, E., and Ayala Carcedo, F. J. (1995). *Drilling and blasting of rocks*. Rotterdam: A.A. Balkema.

Lorenzino, P., Beretta, G., and Navarro, A. (2014). Application of digital image correlation (DIC) in resonance machines for measuring fatigue crack growth. *Frattura Ed Integrita Strutturale*, *30*, 369–374. https://doi.org/10.3221/IGF-ESIS.30.44

Lu, J. (2001). Evaluation of the Thermochemical Code - CHEETAH 2.0 for Modelling Explosives Performance. In *Dsto-Tr-1199*. Victoria, Australia: DSTO Aeronautical and Maritime Research Laboratory.

Lu, W., Leng, Z., Chen, M., Yan, P., and Hu, Y. (2016). A modified model to calculate the size of the crushed zone around a blast-hole. *Journal of the Southern African Institute of Mining and Metallurgy*, *116*(5), 413–422. https://doi.org/10.17159/2411-9717/2016/v116n5a7

Maerz, N. H. (1996a). Image Sampling Techniques and Requirements for automated image analysis of rock fragmentation. *Measurement of Blast Fragmentation : Proceedings of the Fragblast-5 Workshop On Measurement of Blast Fragmentation*, 115–120.

Maerz, N. H. (1996b). Reconstructing 3-D block size distributions from 2-D measurements on sections. *Measurement of Blast Fragmentation : Proceedings of the Fragblast-5 Workshop On Measurement of Blast Fragmentation*, 39–43.

Maerz, N. H., Palangio, T. C., and Franklin, J. A. (1996). WipFrag image based granulometry system. In J. A. Franklin and T. Katsabanis (Eds.), *Measurement of Blast Fragmentation : Proceedings of the Fragblast-5 Workshop On Measurement of Blast Fragmentation* (pp. 91–99). Montreal, Canada: A.A. Balkema.

Maxam. (2015). *RIOFRAG™ Series Mini Prill Ammonium Nitrate Technology*. 2. Retrieved from https://www.maxamcorp.com/

McHugh, S. (1983). Crack extension caused by internal gas pressure compared with extension caused by tensile stress. *International Journal of Fracture*, *21*(3), 163–176. https://doi.org/10.1007/BF00963386

Mellor, M., and Hawkes, I. (1971). Measurement of tensile strength by diametral compression of discs and annuli. *Engineering Geology*, *5*(3), 173–225. https://doi.org/10.1016/0013-7952(71)90001-9

Moser, P., Grasedieck, A., Olsson, M., and Ouchterlony, F. (2003). Comparison of the blast fragmentation from lab-scale and full-scale tests at Bårarp. In R. Holmberg (Ed.), *Explosives and Blasting Technique* (pp. 449–458). A.A. Balkema.

Nie, S., and Olsson, M. (2001). Study of facture mechanism by measuring pressure history in blast holes and crack lengths in rock. *Proceedings of the Annual Conference on Explosives and Blasting Technique*, *I*, 291–300. International Society of Explosives Engineers.

Olsson, M., Nie, S., Bergqvist, I., and Ouchterlony, F. (2002). What causes cracks in rock blasting. *6th International Symposium on Rock Fragmentation by Blasting*, 221–233. https://doi.org/10.1076/frag.6.2.221.8668

Ouchterlony, F. (2003). Influence of blasting on the size distribution and properties of muckpile

fragments, a state-of-the-art review. *MinFo Proj. P2000–10*, 29–32, 97–102.

Ouchterlony, F., Nyberg, U., Olsson, M., Bergqvist, I., Granlund, L., and Grind, H. (2003). The energy balance of production blasts at Nordkalk's Klinthagen quarry. In R. Holmberg (Ed.), *PROCEEDINGS OF EFEE SECOND WORLD CONFERENCE ON EXPLOSIVES AND BLASTING TECHNIQUE* (pp. 193–203). https://doi.org/10.1201/9781439833476.ch24

Palangio, T. C. (1995). Wipfrag - A New Tool for Blast Evaluation. *Proc. 11th Ann. Symp. On BLasting Research*, *1*, 269–280.

Palangio, T. C., and Franklin, J. A. (1996). Practical guidelines for lighting and photography. In J. A. Franklin and T. Katsabanis (Eds.), *Measurement of Blast Fragmentation : Proceedings of the Fragblast-5 Workshop On Measurement of Blast Fragmentation* (pp. 111–125). Montreal, Canada: A.A. Balkema.

Palangio, T. C., and Maerz, N. H. (1999). Case Studies using the WipFrag Image Analysis System. In *Proceedings of the Sixth International Symposium For Rock Fragmentation by Blasting* (pp. 117–120). Retrieved from https://www.researchgate.net/publication/228739792_Case_studies_using_the_WipFrag_image_analysis_system

Palangio, T. C., and Maerz, N. H. (2005). Advanced automatic optical blast fragmentation sizing and tracking. *EFEE Conference Proceedings. Brighton*. Retrieved from https://mospace.umsystem.edu/xmlui/handle/10355/31807

Patel, S. (2018). *Impact of Confined Extension on the Failure Envelope of Intact Low-Porosity Rock*. University of Alberta.

Patel, S., and Martin, C. D. (2018). Application of digital image correlation technique for measurement of tensile elastic constants in Brazilian tests on a bi-modular crystalline rock. *Geotechnical Testing Journal*, *41*(4), 664–674. https://doi.org/10.1520/GTJ20170208

Persson, P. A., Holmberg, R., and Lee, J. (1994). *Rock Blasting and Explosives Engineering*. Boca Raton, FL: CRC Press LLC.

PwC Mining Intelligence and Benchmarking. (2014). *Dragline Dictionary* (p. 557). p. 557. Retrieved from http://pwc.com.au/industry/energy-utilitiesmining/publications/dragline-dictionary.htm

Qian, L., and Tran, H. (1996). Comparing Systems - Validation of FragScan, Wipfrag and Spit. In J. A. Franklin and T. Katsabanis (Eds.), *Measurement of Blast Fragmentation : Proceedings of the Fragblast-5 Workshop On Measurement of Blast Fragmentation* (pp. 151–166). Montreal, Canada: A.A. Balkema.

Rusnak, J., and Mark, C. (2000). Using the point load test to determine the uniaxial compressive strength of coal measure rock. *Proceeding of the 19th International Conference on Ground Control in Mining*, 362–371. Morgantown, WV.

Saharan, M. R., Mitri, H. S., and Jethwa, J. L. (2006). Rock fracturing by explosive energy: Review of state-of-the-art. *Fragblast*, *10*(1–2), 61–81. https://doi.org/10.1080/13855140600858792

Sameti, B., Ziraknejad, N., Azmin, A., Chow, E., Bell, I., and Tafazoli, S. (2014). Portable Rock Fragmentation Sensing Using 3D Imaging. *Proceedings of the Fortieth Annual Conference on Explosives and Blasting Technique*, 537–546.

Sanchidrián, J. A., Segarra, P., and López, L. M. (2006). A practical procedure for the measurement of fragmentation by blasting by image analysis. *Rock Mechanics and Rock Engineering*, *39*(4), 359–382. https://doi.org/10.1007/s00603-005-0073-4

Sanchidrián, J. A., Segarra, P., Ouchterlony, F., and López, L. M. (2009). On the accuracy of fragment size measurement by image analysis in combination with some distribution functions. *Rock Mechanics and Rock Engineering*, *42*(1), 95–116. https://doi.org/10.1007/s00603-007-0161-8

Sanchidrián, José A., Segarra, P., and López, L. M. (2007). Energy components in rock blasting. *International Journal of Rock Mechanics and Mining Sciences*, *44*(1), 130–147. https://doi.org/10.1016/j.ijrmms.2006.05.002

Santamaria, J. ., and Fratta, D. (1996). Image processing in blast fragmentation: Transfer function invertibility. In J. A. Franklin and T. Katsabanis (Eds.), *Measurement of Blast Fragmentation : Proceedings of the Fragblast-5 Workshop On Measurement of Blast Fragmentation* (pp. 121–125). Montreal, Canada: A.A. Balkema.

Santamaria, J. ., Morley, M., Franklin, J. A., and Wang, D. . (1996). Development and testing of a zooming technique for fragmentation. In J. A. Franklin and T. Katsabanis (Eds.), *Measurement of Blast Fragmentation : Proceedings of the Fragblast-5 Workshop On Measurement of Blast Fragmentation* (pp. 133–139). Montreal, Canada, Canada: A.A. Balkema.

Sarfarazi, V., Faridi, H. R., Haeri, H., and Schubert, W. (2015). A new approach for measurement of anisotropic tensile strength of concrete. *Advances in Concrete Construction*, *3*(4), 269–282. https://doi.org/10.12989/acc.2015.3.4.269

Sarfarazi, V., Ghazvinian, A., Schubert, W., Nejati, H. R., and Hadei, R. (2016). A new approach for measurement of tensile strength of concrete. *Periodica Polytechnica Civil Engineering*, *60*(2), 199–203. https://doi.org/10.3311/PPci.8328

Shahram, T., and Nima, Z. (2009). An in-Shovel Camerabased Technology for Automatic Rock Size Analysis in Open Pit Mining. *Proceedings of the 3rd CANUS Rock Mechanics Symposium,* (May), 1–8. Toronto.

Shanthi, C., Kingsley Porpatham, R., and Pappa, N. (2014). Image analysis for particle size distribution. *International Journal of Engineering and Technology*, *6*(3), 1340–1345.

Simonsen, M. (2016). Subset, Step Size and Strain Filter Selection. Retrieved from 13 October website: http://correlatedsolutions.com/support/index.php?/Knowledgebase/Article/View/10/0/subset-step-size-and-strain-filter-selection

Singh, S. P. (1999). The Effect of Shock and Gas Energies on Rock Fracturing Process. *Proceedings of the 25th Annual Conference on Explosives and Blasting Technique*, *1*, 397–406. Nashville, USA: International Society of Explosives Engineers.

Smith, H. J. (1997). The point load test for weak rock in dredging applications. *International Journal of Rock Mechanics and Mining Sciences & Geomechanics Abstracts*. https://doi.org/10.1016/S1365-1609(97)00063-4

Smith, J. M., Van Ness, H. C., and Abbott, M. M. (2005). *Introduction to Chemical Engineering Thermodynamics* (7th ed.). Boston: McGraw-Hill.

Split Engineering LLC. (2016). *What is new with Version 4.0?* Retrieved from http://www.soft-blast.com/Software/SplitDesktop.html

Split Engineering LLC. (2019a). *Split-Net Instruction Manual*. 1–14. Retrieved from https://www.spliteng.com/dloads/

Split Engineering LLC. (2019b). Split Engineering. Retrieved from https://www.spliteng.com/

Sudhakar, J., Adhikari, G. R., and Gupta, R. N. (2006). Technical Note. Comparison of Fragmentation Measurements by Photographic and Image Analysis Techniques. *Rock Mechanics and Rock Engineering*, *39*(2), 159–168. https://doi.org/10.1007/s00603-005-0044-9

SunHills Mining LP. (2018). Highvale Mine. Retrieved from https://sunhills.ca/files/Highvale-Mine-Map.pdf

Sutton, M., Mingqi, C., Peters, W., Chao, Y., and McNeill, S. (1986). Application of an optimized digital correlation method to planar deformation analysis. *Image and Vision Computing*, *4*(3), 143–150. https://doi.org/10.1016/0262-8856(86)90057-0

Sutton, M., Wolters, W., Peters, W., Ranson, W., and McNeill, S. (1983). Determination of displacements using an improved digital correlation method. *Image and Vision Computing*, *1*(3), 133–139. https://doi.org/10.1016/0262-8856(83)90064-1

Sztefek, P., Vanleene, M., Olsson, R., Collinson, R., Pitsillides, A. A., and Shefelbine, S. (2010). Using digital image correlation to determine bone surface strains during loading and after adaptation of the mouse tibia. *Journal of Biomechanics*. https://doi.org/10.1016/j.jbiomech.2009.10.042

Tariq, F., Siddiqui, M. Z., Naz, N., Ahmed, M. F., and Hussain, W. (2012). Practical application of DIC in fatigue and fracture toughness testing. *Proceedings of the International Astronautical Congress, IAC*.

Tavakol Elahi, A., and Hosseini, M. (2017). Analysis of blasted rocks fragmentation using digital image processing (case study: limestone quarry of Abyek Cement Company). *International Journal of Geo-Engineering*, *8*(1), 16. https://doi.org/10.1186/s40703-017-0053-z

Timoshenko, S., and Goodier, N. (1951). *Theory of Elasticity*. New York: McGraw-Hill Book Company, Inc.

Tiossi, R., Lin, L., Conrad, H. J., Rodrigues, R. C. S., Heo, Y. C., de Mattos, M. da G. C., … Ribeiro, R. F. (2012). A digital image correlation analysis on the influence of crown material in implant-supported prostheses on bone strain distribution. *Journal of Prosthodontic Research*. https://doi.org/10.1016/j.jpor.2011.05.003

Tosun, A. (2018). A modified Wipfrag program for determining muckpile fragmentation. *Journal*

of the Southern African Institute of Mining and Metallurgy, *118*(10), 1113–1119. https://doi.org/10.17159/2411-9717/2018/v118n10a13

Toutanji, H., Matthewson, P. R., Effinger, M., and Noumowe, A. (2003). Zero-eccentricity direct-tension testing of thermally damaged cement-based materials. *Cement and Concrete Research*, *33*(10), 1507–1513. https://doi.org/10.1016/S0008-8846(03)00126-1

Van Mier, J. G. M., and Van Vliet, M. R. A. (2002). Uniaxial tension test for the determination of fracture parameters of concrete: State of the art. *Engineering Fracture Mechanics*, *69*(2), 235–247. https://doi.org/10.1016/S0013-7944(01)00087-X

Wagner, M. (2015). WipWare Inc. A Photographer's Advice on Fragmentation Photography. Retrieved from http://wipware.com/a-photographers-advice-on-fragmentation-photography/

Wang, L., Li, J., Qi, Y., Tan, X., Deng, S., and Li, Q. (2018). Application of 3D-DIC method on crack forming process of concrete under axial compression. *Key Engineering Materials*, 21–27. https://doi.org/10.4028/www.scientific.net/KEM.764.21

Wei, K. S., Karuppanan, S., and Latif, M. R. B. A. (2013). Development of an Optical Strain Measurement Method Using Digital Image Correlation. *Asian Journal of Scientific Research*, *6*, 411–422. https://doi.org/10.3923/ajsr.2013.411.422

WipWare. (2017). *Sampling and Analysis Guide* (pp. 1–40). pp. 1–40. Retrieved from http://wipware.com/wp-content/uploads/2018/01/Sampling-and-Analysis-Guide.pdf

WipWare. (2019a). *WipFrag 3: Operating Manual* (pp. 1–41). pp. 1–41. Retrieved from from software

WipWare. (2019b). WipWare. Retrieved from http://wipware.com

Wu, S., Ma, J., Cheng, Y., Xu, M., and Huang, X. (2018). Numerical analysis of the flattened Brazilian test: Failure process, recommended geometric parameters and loading conditions. *Engineering Fracture Mechanics*. https://doi.org/10.1016/j.engfracmech.2018.09.024

Yi-Qiu, T., Lei, Z., Meng, G., and Li-Yan, S. (2012). Investigation of the deformation properties of asphalt mixtures with DIC technique. *Construction and Building Materials*, 581–590. https://doi.org/10.1016/j.conbuildmat.2012.07.046

Yuan, R., and Shen, B. (2017). Numerical modelling of the contact condition of a Brazilian disk test and its influence on the tensile strength of rock. *International Journal of Rock Mechanics and Mining Sciences*, *93*(January), 54–65. https://doi.org/10.1016/j.ijrmms.2017.01.010

Zhang, G. J. (1996). A study of free toe-space explosive loading and its application in open pit blasts. In B. Mohanty (Ed.), *Proceedings of the Fifth International Symposium on Rock Fragmentation by Blasting* (pp. 313–318). Montreal, Quebec, Canada: Rotterdam: A.A. Balkema.

Zhang, Z. (2016). *Rock Fracture and Blasting: Theory and Applications* (Elsevier). https://doi.org/10.1016/B978-0-12-802688-5.00022-1

APPENDICES

Appendix A: Material Safety Data Sheet (MSDS) OF CFE-150

NEWALTA CORPORATION

MATERIAL SAFETY DATA SHEET

SECTION 1 – PRODUCT INFORMATION

MANUFACTURER: NEWALTA CORPORATION
6110 – 27th Street
Edmonton, AB T6P 1J9
www.newalta.com

For additional product information call: (780) 469-0392
Mon-Fri 8 a.m. – 4 p.m. (MT)

Emergency Contacts:
For transportation emergencies:
CANUTEC – 24 HOURS: **1-613-996-6666** (CALL COLLECT)
OR cellular: *666
For other emergencies call the Newalta Emergency Call Centre – 24 Hours: **1-800-567-7455**

PRODUCT: CFE 150

SYNONYMS:	Fuel Oil	CHEMICAL FAMILY:	Petroleum hydrocarbon
BRAND NAMES:	Newalta	CAS REGISTRY NO.:	not applicable to mixtures
PRODUCT I.D.:	10262	**WHMIS CONTROLLED:**	**YES**
PRODUCT USE:	Fuel Oil	Class B-3: Combustible liquid flash point between 37.8°C & 93.3°C; Class D: Toxicity uncertain due to variable composition	

SHIPPING INFORMATION	**TDG** – FUEL OIL 4 Class 3 • UN 1202 • Packing Group III

SECTION 2 – COMPOSITION

100%	Variable mixture of distillate fuel oil and obsolete base oils.

SECTION 3 – HAZARDOUS INGREDIENTS

COMPONENT	WEIGHT %	CAS NUMBER	LD_{50} (route/species)	LC_{50}
Fuel Oils, distillate	40-60	68476-31-3	5.1 mg/kg (oral/rat))	n.av.
Toluene	<1.0	108-88-3	636 mg/kg (oral/rat)	980 ppm (inhalation, mouse)
Xylenes	<0.01 – 1.0	1330-20-7	5,000 mg/kg (oral/rat)	4,550 ppm (inhalation, rat)
Benzene	<0.01 – 0.25	71-43-2	930 mg/kg (oral/rat)	9980 ppm (inhalation, mouse)
Ethylbenzene	<0.01 – 0.2	100-41-4	3500 mg/kg (oral/rat)	4,000 ppm (inhalation, rat)
Heptanes	0.5 – 1.0	142-82-5	n.av	103 g/m^3 air (4 hours; rat)
Octanes	1.0 – 2.5	111-65-9	n.av	118 g/m^3 air (4 hours rat)
Nonanes	1.5 – 3.0	11-84-2	n.av	3.2 g/m^3 air (4 hours; rat)
Cyclopentane	<0.01 – 0.1	287-92-3	>5000 mg/kg (oral/rat)	25.3 mg/L air (4 hours; rat)